

REPORT DOCUMENTATION PAGE

AFRL-SR-BL-TR-98-

0377

Public reporting burden for this collection of information is estimated to average 1 hour per response, including the time for reviewing the data needed, and completing and reviewing the collection of information. Send comments regarding this burden estimate or any other aspect of this collection of information, including suggestions for reducing this burden, to Washington Headquarters Services, Directorate for Information Operations and Reports, 1220 North 17th Street, Arlington, VA 22202-4302, and to the Office of Management and Budget, Paperwork Reduction Project (0377), Washington, DC 20503.

18

process, gathering
is collection of
Highway, Suite

1. AGENCY USE ONLY (Leave Blank)		2. REPORT DATE August 1996		3. REPORT TYPE AND DATES COVERED Final	
4. TITLE AND SUBTITLE Measurement of Proton Electromagnetic Form Factors via the Spin Transfer Reaction				5. FUNDING NUMBERS	
6. AUTHORS Brian Dennis Milbrath					
7. PERFORMING ORGANIZATION NAME(S) AND ADDRESS(ES) University of Virginia				8. PERFORMING ORGANIZATION REPORT NUMBER	
9. SPONSORING/MONITORING AGENCY NAME(S) AND ADDRESS(ES) AFOSR/NI 110 Duncan Avenue, Room B-115 Bolling Air Force Base, DC 20332-8080				10. SPONSORING/MONITORING AGENCY REPORT NUMBER	
11. SUPPLEMENTARY NOTES					
12a. DISTRIBUTION AVAILABILITY STATEMENT Approved for Public Release				12b. DISTRIBUTION CODE	
13. ABSTRACT (Maximum 200 words) See attached.					
14. SUBJECT TERMS				15. NUMBER OF PAGES	
				16. PRICE CODE	
17. SECURITY CLASSIFICATION OF REPORT Unclassified	18. SECURITY CLASSIFICATION OF THIS PAGE Unclassified	19. SECURITY CLASSIFICATION OF ABSTRACT Unclassified	20. LIMITATION OF ABSTRACT UL		

DTIC QUALITY INSPECTED 3

Standard Form 298 (Rev. 2-89)
Prescribed by ANSI Std. Z39.18
Designed using WordPerfect 6.1, AFOSR/XPP, Oct 96

**MEASUREMENT OF PROTON ELECTROMAGNETIC FORM
FACTORS VIA THE SPIN TRANSFER REACTION $^1\text{H}(\vec{e}, e' \vec{p})$**

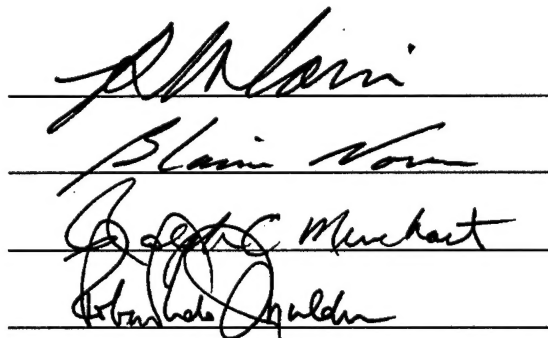
Brian Dennis Milbrath
Palmersville, Tennessee

B.S., Murray State University, 1988

A Dissertation Presented to the Graduate Faculty
of the University of Virginia in Candidacy for the Degree of
Doctor of Philosophy

Department of Physics

University of Virginia
August 1996
(defended June 6, 1996)



[DTIC QUALITY INSPECTED 5]

19980430 021

*To Mom,
who taught me how to live*

Abstract

A measurement of G_E^p/G_M^p at Q^2 values of 0.38 and 0.50 GeV^2 was performed at Bates Linear Accelerator Center using a focal plane polarimeter (FPP) to measure the recoil proton polarization following elastic scattering of polarized electrons on a hydrogen target. These are the first measurements of all three polarization components and determination of the proton's form factors via spin transfer rather than Rosenbluth separation. The ratio G_E^p/G_M^p is obtained in a nearly systematic free manner. The measured polarizations are consistent with the Plane Wave Impulse Approximation (PWIA). This is the first experiment to use the newly-built BATES-FPP and that device is described in detail.

Contents

Chapter 1	Introduction	14
1.1	Using Electron Scattering to Evaluate G_E^p and G_M^p . . .	15
1.2	The G_E and G_M Form Factors	18
1.3	Form Factor Models	19
1.3.1	Dipole Fit	20
1.3.2	Vector Dominance Model Fits	20
1.3.3	Quark Models	23
1.4	Method of Rosenbluth Separation	25
1.5	Previous G_E^p and G_M^p Data	26
1.5.1	Low Q^2 Data	28
1.5.2	High- Q^2 Data	31
1.6	Motivation for this Experiment	32
Chapter 2	The $(\vec{e}, e' \vec{p})$ Reaction	35
2.1	Electron-Proton Coincidence Scattering	35
2.2	Polarizations	36

Chapter 3	Experimental Equipment Setup	42
3.1	Accelerator Facility	42
3.2	Polarized Beam	45
3.2.1	Polarized Source	45
3.2.2	Spin Precession in Beam	47
3.2.3	Møller Polarimeter	49
3.3	Target	51
3.4	MEPS	52
3.4.1	MEPS Scintillators and Pilot	56
3.4.2	MEPS VDCX	58
3.5	OHIPS	60
3.5.1	OHIPS Focal Plane and Pilot	64
3.5.2	OHIPS VDCX	66
3.6	FPP	68
3.6.1	FPP MWPCs	70
3.6.2	FPP Electronics	72
3.6.2.1	MWPC Readout System	72
3.6.2.2	Small-Angle Rejection System	73
3.6.2.3	Multi-hit Rejection System	76

3.7	Coincidence Trigger Electronics	77
3.7.1	Level 2 Trigger Electronics	77
3.7.2	Level 3 Trigger Electronics	80
3.7.3	Experimental Control Electronics	81
3.8	Data Acquisition System	84
Chapter 4	Data Analysis	91
4.1	OHIPS VDCX Analysis	91
4.1.1	Determination of Drift Distances	91
4.1.2	Determination of Wire Plane Coordinates	94
4.1.3	Determination of Focal Plane Coordinates	95
4.1.4	Determination of Target Coordinates	96
4.2	MEPS VDCX Analysis	101
4.2.1	Determination of Analyzable Events	101
4.2.2	Determination of Focal Plane Coordinates	103
4.2.3	Determination of Target Coordinates	104
4.3	Scattering Angles	104
4.4	Coincidence Spectra	106
4.4.1	Time-of-Flight Spectra	106
4.4.2	Missing Energy Spectra	106

4.5	FPP MWPC Analysis	110
4.5.1	Determination of Carbon Scattering Angles	110
4.5.2	Determination of Spin Precession Angle	117
4.6	Extraction of Polarizations	118
4.7	Quadrupole Depolarization Effects	124
Chapter 5	Results	127
5.1	Systematic Errors	127
5.2	Results	129
5.3	Conclusion and Recommendations	133
Appendix A	Derivation of Cross Section Relationships	137
A.1	Cross Section Formalism	137
A.2	The Breit Reference Frame	144
A.3	Proton Transition Current in the Breit Frame	147
A.4	Rosenbluth Formula	150
A.5	Polarizations	151
Appendix B	FPP Calibration at IUCF	155
Appendix C	FPP Alignment	157

Tables

3.1	Target Parameters	54
3.2	MEPS Parameters	56
3.3	OHIPS Parameters	63
3.4	OHIPS Scintillator Dimensions	64
3.5	FPP MWPC Parameters	71
3.6	Event 8 Data Array Structure.	87
3.7	Event 4 Scaler Data Array Structure	88
4.1	OHIPS TRANSPORT Matrix Elements.	100
4.2	MEPS Reverse Matrix Elements.	105
4.3	Quadrupole Depolarization Effects.	126
5.1	Experiment Kinematics	128
5.2	Møller Systematic Errors	129
5.3	Magnet Depolarization Systematic Errors for $Q^2 = 0.38 \text{ GeV}^2$.	130
5.4	Magnet Depolarization Systematic Errors for $Q^2 = 0.50 \text{ GeV}^2$	131

5.5	$Q^2 = 0.38 \text{ GeV}^2$ Systematic Errors	131
5.6	$Q^2 = 0.50 \text{ GeV}^2$ Systematic Errors	132
5.7	$Q^2 = 0.38 \text{ GeV}^2$ Experiment Results	132
5.8	$Q^2 = 0.50 \text{ GeV}^2$ Experiment Results	133
C.1	FPP Chamber Offsets	158

Figures

1.1	Feynman diagram for one-photon exchange in (e,e')	17
1.2	Diagram of Vector Dominance Model (VDM)	22
1.3	Rosenbluth plot examples	26
1.4	G_E^p and G_M^p data	27
1.5	Normalized G_E^p and G_M^p data	29
1.6	Q^{-4} scaling of G_M^p at high- Q^2	32
1.7	Proton form factors at high- Q^2	33
2.1	The (e,e'p) reaction.	36
2.2	The \vec{p} - ^{12}C analyzing power as a function of proton energy.	37
2.3	Theta-dependence of the analyzing power.	38
2.4	Proton-carbon elastic cross section vs. scattering angle.	39
2.5	Target polarization to focal plane coordinates transformation.	40
3.1	Bates Linear Accelerator Center layout	43
3.2	Beam line B layout.	44

3.3	Polarized source layout	46
3.4	Møller polarimeter.	52
3.5	Basel Loop target.	53
3.6	MEPS spectrometer layout.	55
3.7	MEPS pilot logic.	57
3.8	VDCX layout.	59
3.9	DCOS system.	61
3.10	OHIPS layout.	62
3.11	OHIPS focal plane including FPP detail.	65
3.12	OHIPS pilot logic.	67
3.13	OHIPS delay line system.	69
3.14	PCOS III system.	74
3.15	FPP small-angle rejection system.	75
3.16	Measured FPP angular distribution.	76
3.17	Overview of experiment electronics.	78
3.18	Level 2 trigger electronics.	79
3.19	Level 3 trigger electronics.	80
3.20	Experimental control electronics.	82

3.21	Computer analysis flowchart.	90
4.1	Raw VDCX spectra.	92
4.2	VDCX drift distance spectra.	94
4.3	OHIPS VDCX coordinate systems.	97
4.4	Target and focal plane coordinates.	98
4.5	MEPS cluster spectra.	102
4.6	CTOF spectrum.	107
4.7	Missing energy and momentum spectra.	109
4.8	FPP MWPC trajectories.	112
4.9	FPP MWPC scattering vertex reconstruction spectra.	116
4.10	Cone-test diagram	117
5.1	Measured polarizations.	134
5.2	$\mu_p G_E^p / G_M^p$ ratio	135
A.1	Transitions currents in electron-nucleon scattering.	138
A.2	Breit reference frame.	144
B.1	FPP IUCF asymmetry measurement	156
C.1	Misalignment result of small-angle rejection system.	159
C.2	$x = \theta \cos(\phi)$ cut on $-2 < y = \theta \sin(\phi) < 2$ and vice versa.	160

C.3	Event distribution after software θ -cut.	161
-----	--	-----

Chapter 1

Introduction

This dissertation describes an experiment (88-21) performed at the Bates Linear Accelerator Center in Middleton, Massachusetts to measure proton electromagnetic form factors. While these have been measured many times before using Rosenbluth separation, limitations of that method inspired us to use an alternative one measuring polarization transfers in the $^1\text{H}(\vec{e}, e'\vec{p})$ reaction. This method allows the ratio G_E^p/G_M^p to be obtained in a nearly systematic-free manner. The polarization of the outgoing protons was measured using a focal plane polarimeter (FPP) built by our group for this and other experiments. To the extent that G_E^p and G_M^p are known, this experiment also provided on-site calibration of the FPP. The experiment was performed at two Q^2 values: 0.38 and 0.50 GeV^2 , and is the first such experiment to measure all three proton polarization components and determine the form factors.

The remainder of this chapter will discuss the previous Rosenbluth form factor measurements and the models used to describe the form factors. The next chapter of this dissertation will develop the formalism explaining how to measure form factors using polarization transfer. The experimental set-up used for this experiment will be described in chapter 3. Chapter 4 overviews the data analysis while chapter 5 discusses the results. Appendix A provides detailed derivations of cross section relationships used in this document. Appendix B describes the FPP calibration run performed at the Indiana University Cyclotron Facility (IUCF) while appendix C delves into alignment aspects of the FPP.

1.1 Using Electron Scattering to Evaluate G_E^p and G_M^p

Electron scattering has been a successful tool for many years in studying the structure of the nucleus. The main advantages of the electromagnetic probe are the following: ^[1]

- 1) The electromagnetic interaction is well understood and can be described quantitatively very well due to the precision of the underlying theory: quantum electrodynamics (QED). With electron scattering, the cross section can be directly related to the transition matrix elements of the charge and current density operators of the target, i.e. the nuclear electromagnetic structure.
- 2) The electromagnetic interaction is weak, on the order of the fine structure constant $\alpha = \frac{e^2}{4\pi} \approx \frac{1}{137}$. This is part of the reason that QED gives such precise predictions, since the interaction's weakness allows perturbation theory to be used. The weakness also allows the whole target to be probed, whereas the strong-force interactions of proton-scattering tend to just probe the nuclear surface. The target is also probed without greatly disturbing it, whereas with proton scattering it is difficult to separate the scattering mechanisms from target structure effects. Electron scattering can usually (for $1/Z \gg \alpha$, where Z is the nuclear charge) be treated in the first Born approximation, i.e. as the exchange of a single virtual photon.
- 3) Electron scattering allows one to vary the momentum transfer \vec{q} while keeping the energy transfer ω fixed (and vice versa). This is what separates electron scattering from photon scattering since real photon

^[1] T. de Forest Jr. and J.D. Walecka, *Adv. Phys.* **15**, 1 (1966).

scattering has the constraint that $q_\mu^2 \equiv \omega^2 - \vec{q}^2 = 0$. Virtual (or “off-mass shell”) photons, however, have $q_\mu^2 < 0$. Thus one is allowed to study the \vec{q} -dependence of the transition matrix elements and use Fourier transforms to determine the spatial distributions of the nucleus’s charge and current densities.

Figure 1.1 illustrates the one-photon exchange process in (e, e') scattering off a nucleon. The electron has initial energy E and initial momentum \vec{k} . After scattering through an angle θ_e its final energy is E' and its final momentum is \vec{k}' . The electron interacts with a nucleon by the exchange of a virtual photon. The electron’s energy transfer is

$$\omega = E - E' \quad (1.1)$$

and its 3-momentum transfer is

$$\vec{q} = \vec{k} - \vec{k}' \quad (1.2)$$

The four-momentum transfer is expressed as $q_\mu = (\omega, \vec{q})$; its squared magnitude as

$$q_\mu^2 = \omega^2 - \vec{q}^2 \equiv m^2 \equiv -Q^2 \quad , \quad (1.3)$$

which can be approximated in the extreme relativistic limit ($m_e \approx 0$) as:

$$q_\mu^2 \approx -2k \cdot k' \approx -4E_e E'_e \sin^2(\theta_e/2) \quad . \quad (1.4)$$

Using only Lorentz covariance, gauge invariance, and parity conservation; the doubly-differential cross section for unpolarized (e, e') (inclusive) scattering can be shown to depend on only two response functions, R_L and R_T , which contain all the target structure information: [2]

$$\frac{d^2\sigma}{d\Omega d\omega} = \sigma_M \left\{ \left(\frac{q_\mu}{\vec{q}} \right)^4 R_L(\vec{q}, \omega) + \left[\frac{1}{2} \left(\frac{q_\mu}{\vec{q}} \right)^2 + \tan^2\left(\frac{\theta_e}{2}\right) \right] R_T(\vec{q}, \omega) \right\} \quad . \quad (1.5)$$

[2] M. Gourdin, *Nuovo Cim.* **21**, 1094 (1961).

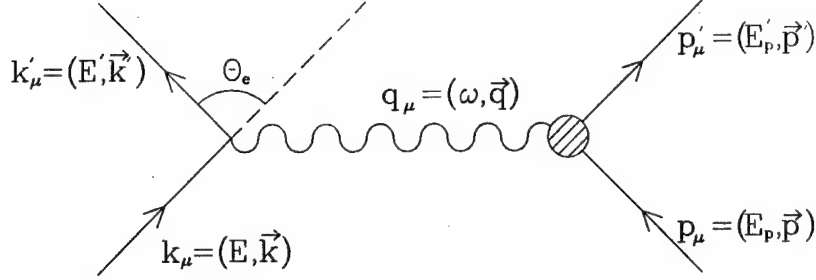


Figure 1.1 Feynman diagram for one-photon exchange in (e, e') .

σ_M is the Mott cross section. It represents the scattering off a spinless, pointlike particle and is given by:

$$\sigma_M = \frac{\alpha^2 \cos^2(\theta_e/2)}{4E^2 \sin^4(\theta_e/2)} . \quad (1.6)$$

R_L and R_T are the nuclear response functions to longitudinal and transverse photons, respectively. For the specific case of elastic (e, e') scattering from the nucleon this differential cross section is expressed as: ^[3]

$$\left[\frac{d\sigma}{d\Omega_e} \right]_{\text{Rosenbluth}} = \left[\frac{d\sigma}{d\Omega_e} \right]_{ns} \times \left[\frac{G_E^2(Q^2)}{1 + \tau} + \tau G_M^2(Q^2) \left(\frac{1}{1 + \tau} + 2 \tan^2 \frac{\theta_e}{2} \right) \right] \quad (1.7)$$

where $\tau = Q^2/4M_p^2$. A detailed derivation of this equation can be found in appendix A. The first term on the right side, the nonstructure differential cross section, is just the Mott cross section times a target recoil factor. G_E and G_M are called form factors and contain the additional information about the finite spatial extent of the nucleon's charge and magnetization distributions respectively. One can see from comparing the two cross section equations that

[3] M.N. Rosenbluth, Phys. Rev. **79**, 615 (1950).

R_L relates to the charge distribution and R_T relates to the magnetization distribution. The Rosenbluth formula (1.7) is valid for both protons and neutrons, but with different form factors (denoted as $G_{E(M)}^n$ for neutrons and $G_{E(M)}^p$ for protons). The accurate measurement of these form factors has consistently been one of the leading efforts of experimental nuclear physics. Likewise, any baryon structure model that wishes to be considered successful must be able to predict their values. Before describing the existing form factor measurements and models several points should be made about them.

1.2 The G_E and G_M Form Factors

As is shown in appendix A, G_E and G_M are closely related to the nucleon's charge distribution and magnetic moment distribution, respectively. Hence, as Q^2 goes to zero, $G_E^p \rightarrow 1$, $G_E^n \rightarrow 0$, $G_M^p \rightarrow \mu_p$, and $G_M^n \rightarrow \mu_n$. It should be noted that G_E and G_M (the Sachs form factors) are not the only possible pair of form factors. Often used are the Dirac (F_1) and Pauli (F_2) form factors. The two sets are simply related:

$$\begin{aligned} G_E &= F_1 - \frac{\kappa Q^2}{4M^2} F_2 \\ G_M &= F_1 + \kappa F_2 \end{aligned} \quad (1.8)$$

As Q^2 goes to zero; $F_1^p \rightarrow 1$, $F_2^p \rightarrow 1$, $F_2^n \rightarrow 1$, and $F_1^n \rightarrow 0$. These form factors predate the Sachs form factors. The use of the Sachs form factors has a more readily understood physical interpretation (Fourier transform of charge and magnetic moment distributions) and also avoids having a cross-term in the Rosenbluth equation. [4]

Even without a cross-term, the Rosenbluth equation presents a problem with respect to the extraction of G_E^2 : the τ term in front of G_M^2 . This causes the

[4] L.N. Hand, D.G. Miller, and R. Wilson, Rev. Mod. Phys. **35**, 335 (1963).

G_E^2 term to contribute less to the cross section, making its extraction harder, as Q^2 is increased. Compounding the problem for the neutron is the fact that G_E^n is much smaller (since it's chargeless) than G_M^n , making its extraction even more difficult.

A final problem for determining the neutron form factors is the fact that there are no free neutrons to scatter from, so instead of using a simple hydrogen target, the neutron form factors are determined mostly from scattering off a deuteron target. Thus the scattering is actually quasielastic instead of elastic. The deuteron is used for several reasons: it's the simplest nuclear target available, it is loosely bound, and its wave-functions are the best known. Since the deuteron is loosely bound, the neutron is barely off the mass-shell (provided the neutron's recoil momentum p_r is near zero). This is important since differences between bound and unbound nucleons are thought to be possible. Of course, the analysis becomes trickier with the introduction of deuteron wave functions and meson-exchange currents in the deuteron, not to mention differentiating between proton and neutron scattering. Since this experiment dealt with proton form factors, we were spared these additional problems.

1.3 Form Factor Models

Before looking at the existing data, a discussion of the many form factor models is in order. While the models are usually based somewhat on physical arguments, they are all at least partially fitted to the measured data. The most common approach is to try to fit a single underlying form factor to all four of the form factors, though in actuality it is the proton data that most constrains the models since its form factors have been measured more precisely.

1.3.1 Dipole Fit

The most commonly used fit is the dipole fit. Its form is:

$$G_D(Q^2) = \frac{1}{(1 + \frac{Q^2}{\lambda})^2} \quad (1.9)$$

λ is a fit parameter whose value is 0.71 (GeV/c)^2 based on the existent data. The dipole fit is so popular that data and other theories are often normalized with respect to it. Though it works fairly well, it is completely empirical. Note that $G_D(0) = 1$. In relation to G_D , the form factors are:

$$\begin{aligned} G_E^p(Q^2) &= G_D(Q^2) \\ G_M^p(Q^2) &= \mu_p G_D(Q^2) \\ G_M^n(Q^2) &= \mu_n G_D(Q^2) \quad ; \end{aligned} \quad (1.10)$$

hence these three form factors seem to scale in relationship to each other. Notice that they go to the correct values as Q^2 goes to zero. The dipole form is not appropriate for G_E^n as at $Q^2 = 0$ its value must go to zero. For G_E^n the best empirical fit seems to be:

$$G_E^n(Q^2) = \frac{-a\mu_n\tau}{1 + b\tau} G_D(Q^2) \quad (1.11)$$

For a Paris potential deuteron model, the fit values are $a = 1.25 \pm 0.13$ and $b = 18.3 \pm 3.4$. [5]

1.3.2 Vector Dominance Model Fits

A model that has been fruitful, though ultimately not definitive, is the vector dominance model (VDM). In this model, the form factors provide a physical understanding of nucleon structure based on dispersion relations. As

[5] B. Frois and S. Platchkov, *Modern Topics in Electron Scattering*, eds. B. Frois and I. Sick, World Scientific, (1991).

depicted in figure 1.2, [6] the virtual photon converts to a neutral vector meson (which may be isoscalar or isovector) prior to coupling with the nucleon. The absorptive parts of the form factors (the spectral function) are parameterized by pole terms at vector resonances, so that the form factors can be expressed as a sum over meson propagators times coupling strengths:

$$F^{IS(V)} = \sum_i \frac{a_i^{IS(V)}}{Q^2 + M_{IS(V)i}^2} . \quad (1.12)$$

(It is the coupling strengths $a_i^{IS(V)}$ and masses $M_{IS(V)i}$ that are usually fitted.)

The above form factors are related to the standard Dirac and Pauli ones by:

$$\begin{aligned} F_1^p &= F_1^{IS} + F_1^{IV} \\ F_2^p &= \frac{1}{\kappa_p} (F_2^{IS} + F_2^{IV}) \\ F_1^n &= F_1^{IS} - F_1^{IV} \\ F_2^n &= \frac{1}{\kappa_n} (F_2^{IS} - F_2^{IV}) , \end{aligned} \quad (1.13)$$

where $\kappa_p = 1.793$ and $\kappa_n = -1.913$. (Some fits use different normalizations.)

The VDM's need for resonances led to the predictions of the existence of the isovector vector meson ρ and the isoscalar vector meson ω . [7] The isoscalar strange ϕ meson is usually included, as well. A good fit cannot be achieved using the vector mesons alone, however, and all of the fits include additional empirical poles. Classic examples of this type of fit are the Mainz eight-pole fit [8] and the fit of Höhler *et al.*, [9] which treated the ρ exchange

[6] L. Andivahis *et al.*, Phys. Rev. D **50**, 5491 (1994).

[7] T.A. Griffy and L.I. Schiff, *High Energy Physics*, Vol. 1, ed. E.H. Burhop, Academic Press, (1967).

[8] G.G. Simon *et al.*, Nucl. Phys. **A333**, 381 (1980).

[9] G. Höhler *et al.*, Nucl. Phys. **B114**, 505 (1976).

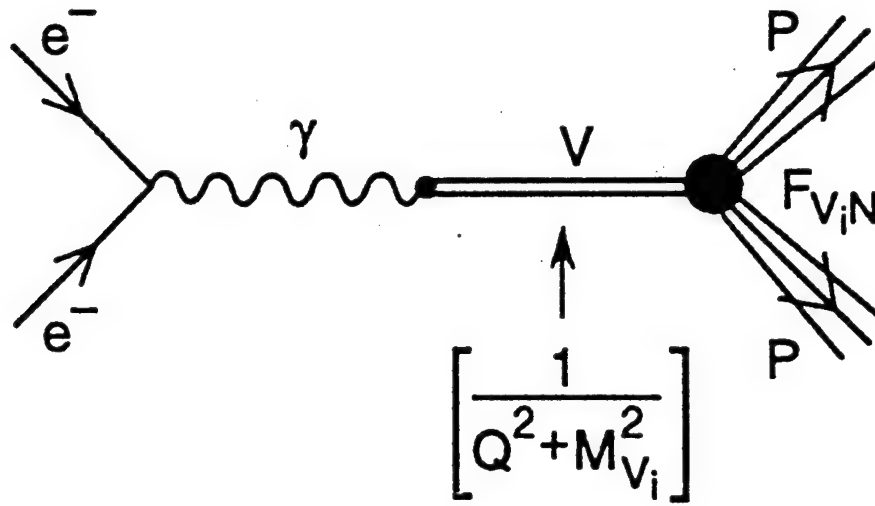


Figure 1.2 Diagram of Vector Dominance Model (VDM) from reference [6].

more completely than a simple pole term, taking the effects of the two-pion continuum into account. [10]

Some VDM models, called extended vector dominance models (EVDM), describe the effective interaction of the photon with the nucleon as having two pieces: the term involving vector mesons and a term involving direct interactions with the nucleon. In the time-like region ($q^2 > 0$) the vector meson contributions dominate near the meson poles. However, in the space-like region ($q^2 < 0$) where the intermediate mesons are far off-shell the model must be extended to include the non-negligible direct contributions.

A particularly successful EVDM model at intermediate energies is by Gari and Krümpelmann. [11] The Gari-Krümpelmann model incorporates quark dynamics at large Q^2 via perturbative QCD (pQCD). Notice the model's

[10] P. Mergell *et al.*, hep-ph/9506375 preprint (20 Jun 95).

[11] M. Gari and W. Krümpelmann, Z. Phys. **A322**, 689 (1985).

isovector F_1 term:

$$F_1^{IV}(Q^2) = \left[\frac{m_\rho^2}{m_\rho^2 + Q^2} \frac{g_\rho}{f_\rho} + \left(1 - \frac{g_\rho}{f_\rho}\right) \right] F_1(Q^2) \quad , \quad (1.14)$$

where $m_\rho = 0.776$ GeV,

$$F_1(Q^2) = \frac{\Lambda_1^2}{\Lambda_1^2 + \hat{Q}^2} \frac{\Lambda_2^2}{\Lambda_2^2 + \hat{Q}^2} \quad , \quad (1.15)$$

and

$$\hat{Q}^2 = Q^2 \frac{\log(\frac{\Lambda_2^2 + Q^2}{\Lambda_{QCD}^2})}{\log(\frac{\Lambda_2^2}{\Lambda_{QCD}^2})} \quad . \quad (1.16)$$

This gives a meson monopole fit at low Q^2 which dies out as Q^2 increases to leave a direct photon-quark coupling term. F_1 gives the expected behavior at high Q^2 , such as Q^{-4} scaling (which will be discussed in the next section). Both meson and quark features exist for $Q^2 \sim \Lambda_2^2$. Fits to the data gave the values: $g_\rho/f_\rho = 0.377$, $\Lambda_1 = 0.795$ GeV, $\Lambda_2 = 2.27$ GeV, and $\Lambda_{QCD} = 0.29$ GeV.

1.3.3 Quark Models

Many efforts have been made to model the form factors at high Q^2 based on quark theory. Dimensional scaling laws predicted that

$$G(Q^2 \rightarrow \infty) = \left(\frac{1}{Q^2} \right)^{n_H - 1} \quad , \quad (1.17)$$

where n_H is the number of valence quarks. ^[12] Perturbative QCD was later shown to give this Q^{-4} scaling result: ^[13]

$$G_M(Q^2) = C \frac{\alpha_s^2(Q^2)}{Q^4} \left[\ln \left(\frac{Q^2}{\Lambda_{QCD}^2} \right) \right]^{-4/3\beta} \quad , \quad (1.18)$$

^[12] S.J. Brodsky and G.R. Farrar, Phys. Rev. D 11, 1309 (1975); S.J. Brodsky and B.T. Chertok, Phys. Rev. D 14, 3003 (1976).

^[13] G.P. Lepage and S.J. Brodsky, Phys. Rev. Lett. 43, 545, 1625(E) (1979); G.P. Lepage and S.J. Brodsky, Phys. Rev. D 22, 2157 (1980).

and implied a decay of $G_M Q^4$ at high Q^2 as given by the running coupling constant $\alpha_s(Q^2)$:

$$\alpha_s(Q^2) = \frac{4\pi}{\beta \ln(Q^2/\Lambda_{QCD}^2)} \quad , \quad (1.19)$$

where β is a QCD one-loop function that equals 9 for a three-flavor quark system.^[10] The rate of decrease is determined by the scale parameter Λ_{QCD} . C is a model-dependent constant of unreliable value. Nonetheless, a recent update^[10] to Höhler *et al.*^[9] incorporated this large- Q^2 pQCD behavior into their VDM model. Their fit claimed to have poles identifiable with physical states in all but one case. Those poles were: $\omega, \phi, S'(1600), \rho$ (with two-pion cut), $\rho(1450), \rho(1650)$, and $\rho(1690)$. The $\rho(1690)$ is their one claimed unphysical state. According to the Particle Data Book,^[14] the mass of the second ρ is 1700 MeV, not 1650.

Unlike perturbative QCD, QCD sum rules are able to determine the overall magnitude of G_M^p and not just its evolution. This method uses sum rules to estimate wave function moments and then the wave functions themselves; after which perturbative calculations can be performed. These wave functions are quite different from nonrelativistic or asymptotic wave functions and imply that in the proton the u-quark whose spin is parallel to the proton's momentum carries around 65% of the proton's total momentum.^[15]

Additionally, the center-of-mass bag model has also been used to predict the form factors.^[16] In it, the SU(6) symmetry-breaking spin-dependent forces arise either from pQCD or from nonperturbative instanton effects. The fitted parameter is ξ , the ratio between the d-quark and u-quark distribution radii in

[14] M. Aguilar-Benitez *et al.*, Phys. Rev D **50**, 1173 (1994).

[15] V.L. Chernyak and A.R. Zhitnitsky, Phys. Rep. **112**, 173 (1984).

[16] X. Song and J.S. McCarthy, Phys. Rev. C **46**, 1077 (1992).

the proton. Small pion-cloud corrections are needed for $Q^2 < 0.3 \text{ GeV}^2/c^2$.

1.4 Method of Rosenbluth Separation

All of the form factor measurements presented in the next section with the exception of one (SLAC-NE4) were performed using the Rosenbluth separation method. Defining the quantity

$$\epsilon(\theta_e) = [1 + 2(1 + \tau)\tan^2(\theta/2)]^{-1} , \quad (1.20)$$

equation 1.7 can be rewritten as

$$\left[\frac{d\sigma}{d\Omega_e} \right]_{\text{Rosenbluth}} = \left[\frac{d\sigma}{d\Omega_e} \right]_{ns} \frac{1}{1 + \tau} \left[G_E^2(Q^2) + \frac{\tau}{\epsilon} G_M^2(Q^2) \right] . \quad (1.21)$$

ϵ is the virtual photon's longitudinal polarization, ranging from 0 to 1 as θ goes from $\pi \rightarrow 0^\circ$. For Rosenbluth separation it is convenient to define a reduced cross section that is a function of Q^2 and ϵ :

$$\begin{aligned} \left[\frac{d\sigma}{d\Omega_e} \right]_{\text{reduced}} &= \frac{\epsilon(1 + \tau)}{\left[\frac{d\sigma}{d\Omega_e} \right]_{ns}} \left[\frac{d\sigma}{d\Omega_e} \right]_{\text{Rosenbluth}} \\ &= \tau G_M^2(Q^2) + \epsilon G_E^2(Q^2) . \end{aligned} \quad (1.22)$$

Using this equation a set of measurements at fixed Q^2 but different values of E and θ_e can be used to determine the form factor values. The reduced cross sections are plotted versus ϵ with τG_M^2 as the intercept and G_E^2 as the slope. Figure 1.3 shows the Rosenbluth plots of Walker *et al.* [17]

The problem of determining the form factors from kinematically different measurements should be apparent. The extracted form factors are quite sensitive to systematic errors in E, E' , and θ . For example, one can maximize the count rate and longitudinal polarization at forward angles, but there the

[17] R.C. Walker *et al.*, Phys. Rev. D **49**, 5671 (1994).

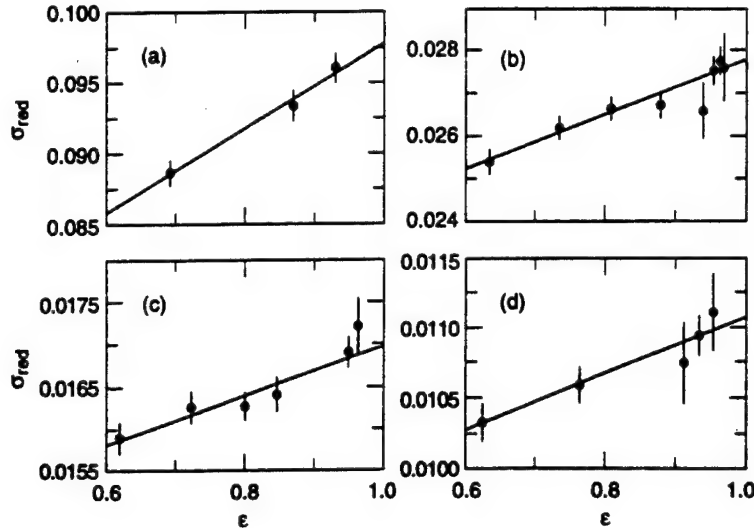


Figure 1.3 The Rosenbluth plots from reference ^[17] at (a) $Q^2 = 1.0$, (b) $Q^2 = 2.0$, (c) $Q^2 = 2.5$, and (d) $Q^2 = 3.0$ (GeV/c)². The error bars include statistical and systematic errors but not normalization errors.

cross section is very sensitive to variations in θ . Additionally, spectrometer acceptances large enough to get good statistics might require model folding over the acceptance range. As mentioned earlier, at high Q^2 , $\tau G_M^2 \gg G_E^2$ making the Rosenbluth fit's slope hard to determine.

1.5 Previous G_E^p and G_M^p Data

Figure 1.4 shows selected data from previous G_E^p and G_M^p measurements with particular emphasis on the intermediate- Q^2 values ($\approx 0.5 - 3.0$ (GeV/c)²). The solid line is the dipole fit (eqs. 1.9 and 1.10). The data are from: Walker *et al.* ^[17] (open diamonds), Bartel *et al.* ^[18] (open squares), SLAC-NE4 ^[19] (small

^[18] W. Bartel *et al.*, Nucl. Phys. B58, 429 (1973).

^[19] P.E. Bosted *et al.*, Phys. Rev. C 42, 38 (1990).

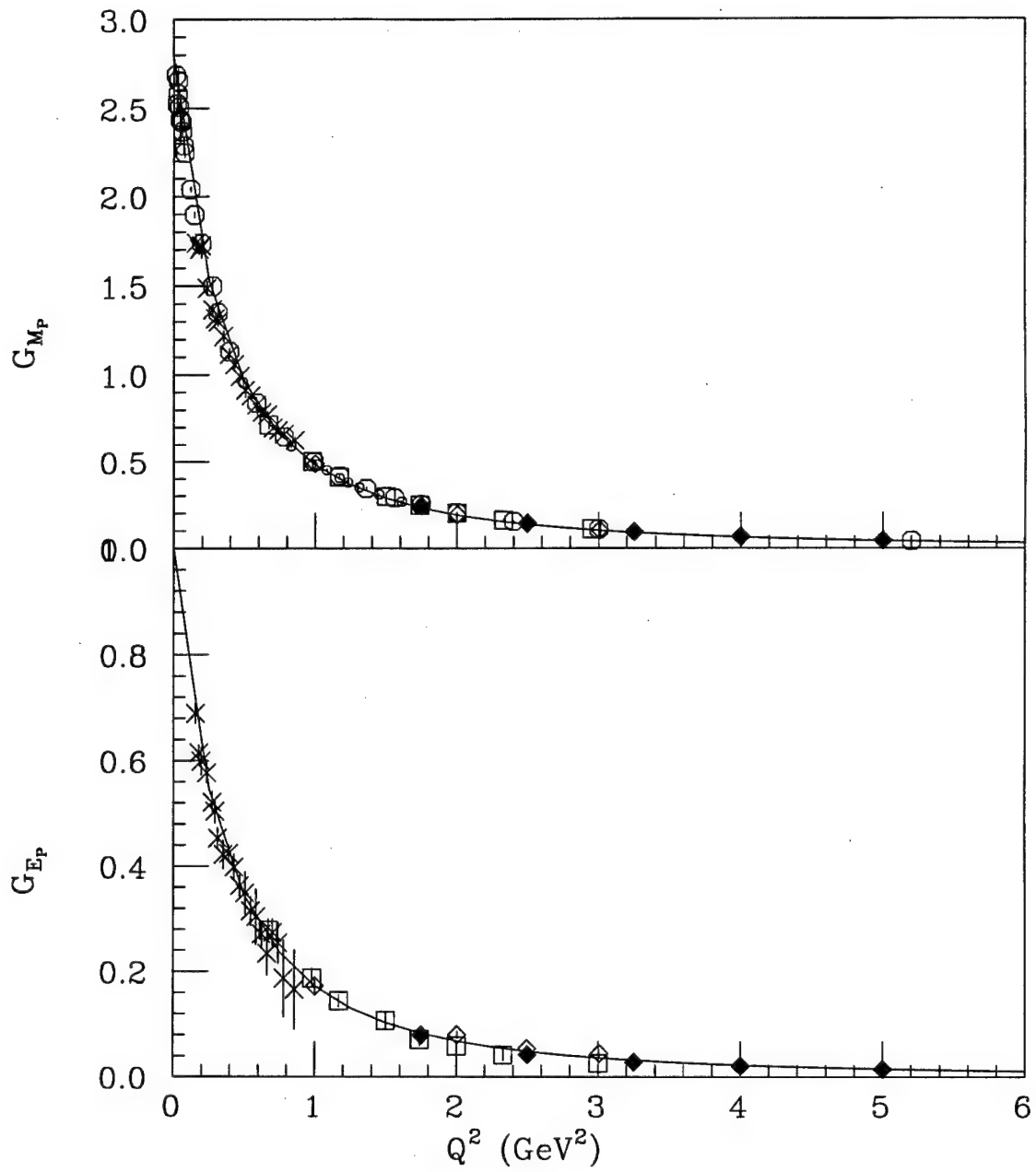


Figure 1.4 G_E^p and G_M^p data. Solid line is the dipole fit. Data are listed in the text.

open circles), SLAC-NE11 ^[6] ^[20] (shaded diamonds), Janssens *et al.* ^[21] (Xs), and Höhler *et al.* ^[9] (open circles). The SLAC-NE4 data are only for G_M^p . That experiment was done at $\theta_e = 180^\circ$, where the cross section depends entirely on G_M^2 (as can be seen in eq. 1.7, taking the nonstructure term's angle-dependence into account). Figure 1.5 shows the same data set normalized to the dipole fit.

For G_M^p the Mainz ^[8] (short dash) and Mergell *et al.* ^[10] (thin line) VDM fits and the extended VDM fit of Gari and Krümpelmann ^[11] (dots) seem to work well. The other fits are Janssens *et al.*'s three-pole fit ^[21] (thick dots), Höhler *et al.*'s VDM fit 8.2 ^[9] (dot-dash), and Blatnik and Zovko's extended VDM model with asymptotic constraints ^[22] (long dash). For G_E^p the data from the different measurements seems to diverge above 1 GeV² and a conclusion is difficult to reach. The remainder of this section will discuss the proton form factors in the low and high Q^2 regions. For figures and discussion of G_E^n and G_M^n measurements please see Markowitz. ^[23]

1.5.1 Low Q^2 Data

In the low- Q^2 region much of the form factor measurement effort has been focussed on obtaining the proton's root-mean-square (rms) charge radius. In the Breit frame (section A.2), $Q^2 = \vec{q}^2$ and the form factors are the Fourier

^[20] P.E. Bosted *et al.*, Phys. Rev. Lett. **68**, 3841 (1992).

^[21] T. Janssens *et al.*, Phys. Rev. **142**, 922 (1966).

^[22] S. Blatnik and N. Zovko, Acta Phys. Austr. **39**, 1 (1974).

^[23] P. Markowitz, Ph.D. dissertation, William & Mary (1992), unpublished.

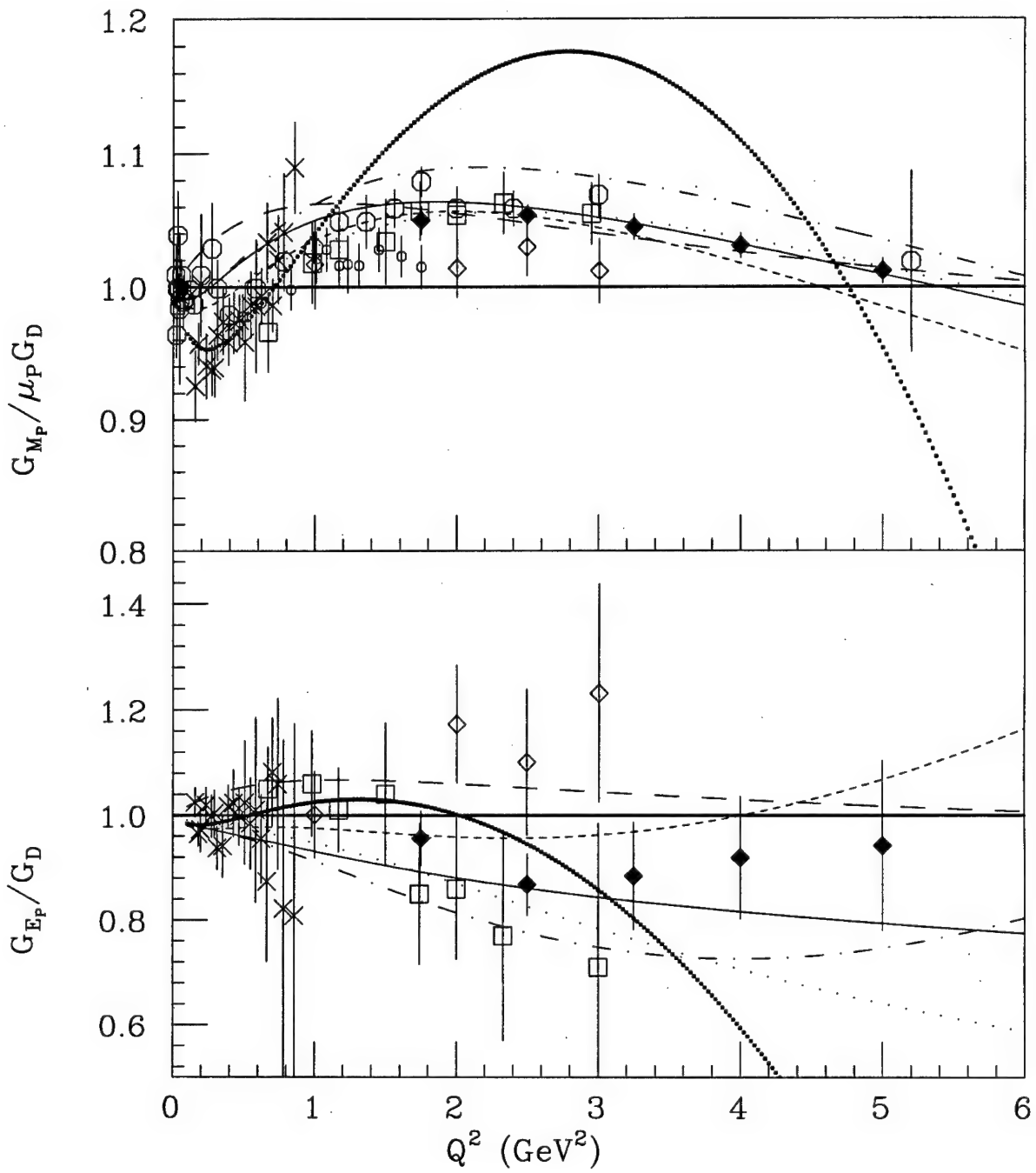


Figure 1.5 G_E^p and G_M^p data normalized with respect to the dipole fit. Data symbols and fits are listed in the text.

transforms of the charge and magnetic moment distributions: [24]

$$\begin{aligned} G_E(\vec{q}^2) &= \int \rho(\vec{x}) e^{i\vec{q} \cdot \vec{x}} d^3x \\ G_M(\vec{q}^2)(\vec{\sigma} \times \vec{q}) &= \int \vec{J}(\vec{x}) e^{i\vec{q} \cdot \vec{x}} d^3x \quad , \end{aligned} \quad (1.23)$$

where $G_{E(M)}(0)$ is given in eq. 1.10. These spatial distributions are not Lorentz invariant, though, and consequently are only useful in the nonrelativistic limit at low- Q^2 . Since the form factors are functions of a single variable they can be expanded in a Taylor series at $\vec{q}^2 = 0$:

$$G(\vec{q}^2) = \sum_{n=0}^{\infty} \frac{(\vec{q}^2)^n}{n!} \left. \frac{d^n G(\vec{q}^2)}{d(\vec{q}^2)^n} \right|_{\vec{q}^2=0} \quad (1.24)$$

Expanding the Fourier integral for the charge form factor gives:

$$\begin{aligned} G_E(\vec{q}^2) &= \int \left(1 + i\vec{q} \cdot \vec{x} - \frac{(\vec{q} \cdot \vec{x})^2}{2} + \dots \right) \rho(\vec{x}) d^3x \\ &= 1 - \frac{1}{6} |\vec{q}|^2 \langle r^2 \rangle + \dots \quad , \end{aligned} \quad (1.25)$$

where $\langle r^2 \rangle = \int r^2 \rho(r) 4\pi r^2 dr$. Matching terms in the two previous series equations gives the relationship:

$$\langle r^2 \rangle = -6 \left. \frac{dG(\vec{q}^2)}{d\vec{q}^2} \right|_{\vec{q}^2=0} \quad (1.26)$$

Applying this formula to the dipole fit gives the value of the proton's electric rms radius as 0.81 fm. [25] Early Stanford data gave a value near this (0.805 ± 0.011), [4] but a later result from Mainz determined by fitting the low- Q^2 data to a polynomial of second order gave 0.862 ± 0.012 fm. [8] This is consistent with new NIST (National Institute of Standards and Technology) measurements using Fourier-Bessel analysis which gave a value of 0.865 ± 0.020 fm. [26] Recent

[24] R.G. Sachs, Phys. Rev. **126**, 2256 (1962).

[25] F. Borkowski *et al.*, Z. Phys. **A275**, 29 (1975).

[26] M. McCord *et al.*, Nucl. Inst. Meth. **B56**, 496 (1991).

Lamb shift measurements ^[27] are consistent with the larger proton size. This discrepancy, unfortunately, limits the attainable precision of some important experimental tests of QED.

1.5.2 High- Q^2 Data

In the high- Q^2 region it is much easier to measure G_M than G_E due to the factor of τ in the Rosenbluth cross section. Above $Q^2 = 5 \text{ (GeV/c)}^2$, G_E only contributes a few percent to the cross section. Arnold *et al.* ^[28] measured G_M^p up to $Q^2 = 31.3 \text{ (GeV/c)}^2$ at the Stanford Linear Accelerator Center (SLAC). In their analysis they presumed that G_E^p continued to scale with G_M^p since any small deviation from this would have little effect at such high energies. They found (figure 1.6) that at around $Q^2 = 8 \text{ (GeV/c)}^2$ G_M^p scaled with respect to Q^{-4} as the naive dimensional scaling laws said and that after that there was a decrease of $Q^4 G_M^p$ with increasing Q^2 as predicted by pQCD. Mergell *et al.*'s fit, ^[10] however, shows that sizeable hadronic pole contributions still exist between 10 and 20 (GeV/c)^2 and that more data is probably needed before concluding that scaling has been seen.

The harder G_E^p term has been measured up to $Q^2 = 8.83 \text{ (GeV/c)}^2$ by Bosted *et al.* ^[6] ^[20] Their results (figure 1.7) show that G_E^p is most consistent with the dipole fit at high- Q^2 . They found G_M^p , on the other hand, to be most consistent with VDM models, particularly the one by Gari and Krümpelmann. ^[11]

In summary, then, there exists no model that is totally successful at

^[27] D.J. Berkeland *et al.*, Phys. Rev. Lett. **75**, 2470 (1995).

^[28] R.G. Arnold *et al.*, Phys. Rev. Lett. **57**, 174 (1986); A.F. Sill *et al.*, Phys. Rev. D **48**, 29 (1993).

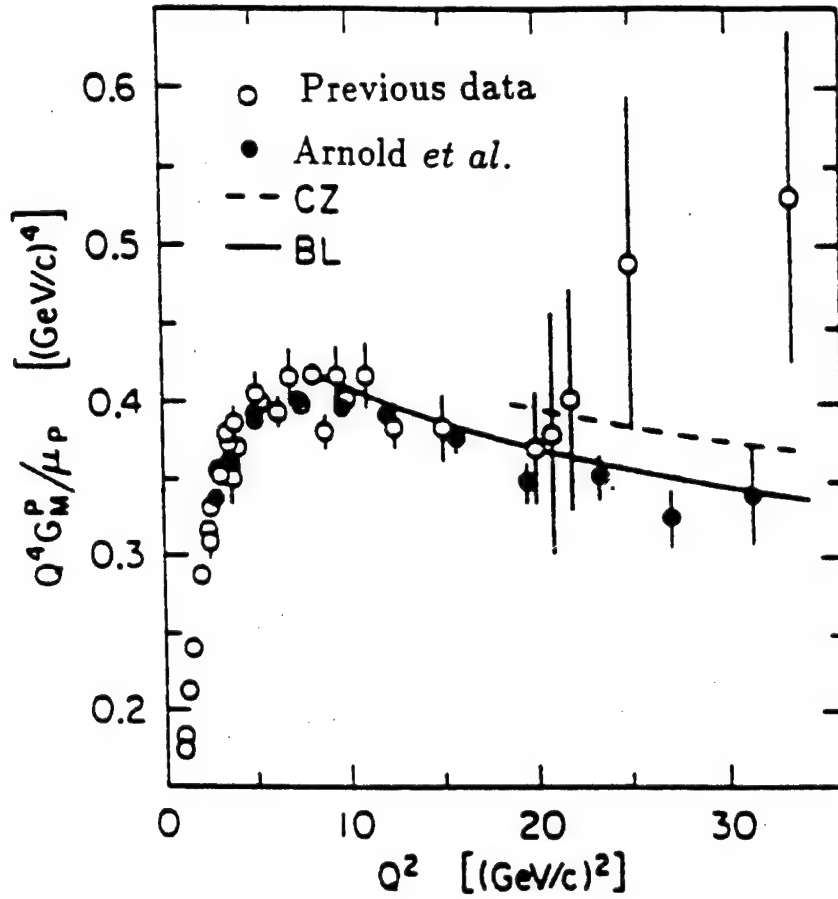


Figure 1.6 Q^{-4} Scaling of G_M^p at high- Q^2 .^[28] The fits use pQCD (BL)^[13] and sum rules (CZ)^[15] with $\Lambda_{QCD} = 100$ MeV.

explaining all (or even one) of the form factors over the entire Q^2 range.

1.6 Motivation for this Experiment

Hopefully by this point our motivation for this experiment is understood. G_E and G_M contain the unknown knowledge about nucleon structure and hence need to be known precisely to constrain nucleon models. At intermediate-energies, knowledge of the form factors helps to model the crossover area between a low-energy description in terms of meson degrees of freedom and

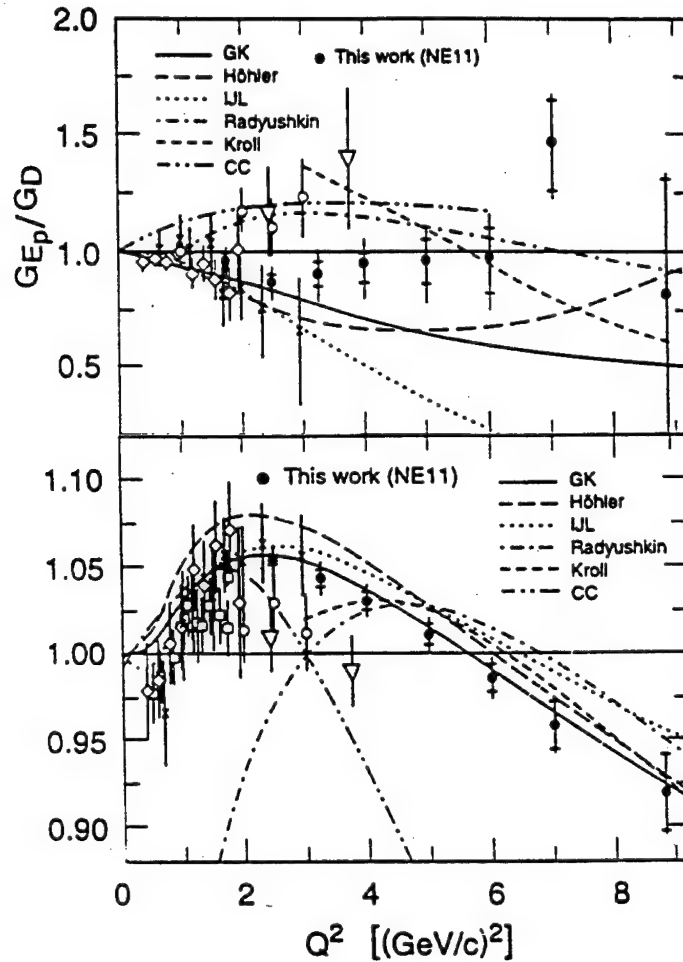


Figure 1.7 Proton form factors at high- Q^2 . Please see reference [6] for explanation of fits.

a high-energy description in terms of quarks and gluons. The systematic uncertainties involved with the Rosenbluth method and the limited precision of the G_E^p data at high- Q^2 point to the need for a new method of form factor measurement. Our method, polarization transfers in the $(\vec{e}, e' \vec{p})$ reaction, allowed for the simultaneous measurement of the form factors, reducing the systematic errors. Performing such an experiment at Bates Linear Accelerator

Center also served to lay the ground work for similar future experiments ^[29] at the next generation of electron-scattering labs such as the Continuous Electron Beam Accelerator Facility (CEBAF).*

[29] CEBAF PR 93-027, "Electric Form Factor of the Proton by Recoil Polarization", C.F. Perdrisat and V. Punjabi, co-spokespersons.

* CEBAF was renamed the Thomas Jefferson National Accelerator Facility on May 24, 1996.

Chapter 2

The $(\vec{e}, e' \vec{p})$ Reaction

2.1 Electron-Proton Coincidence Scattering

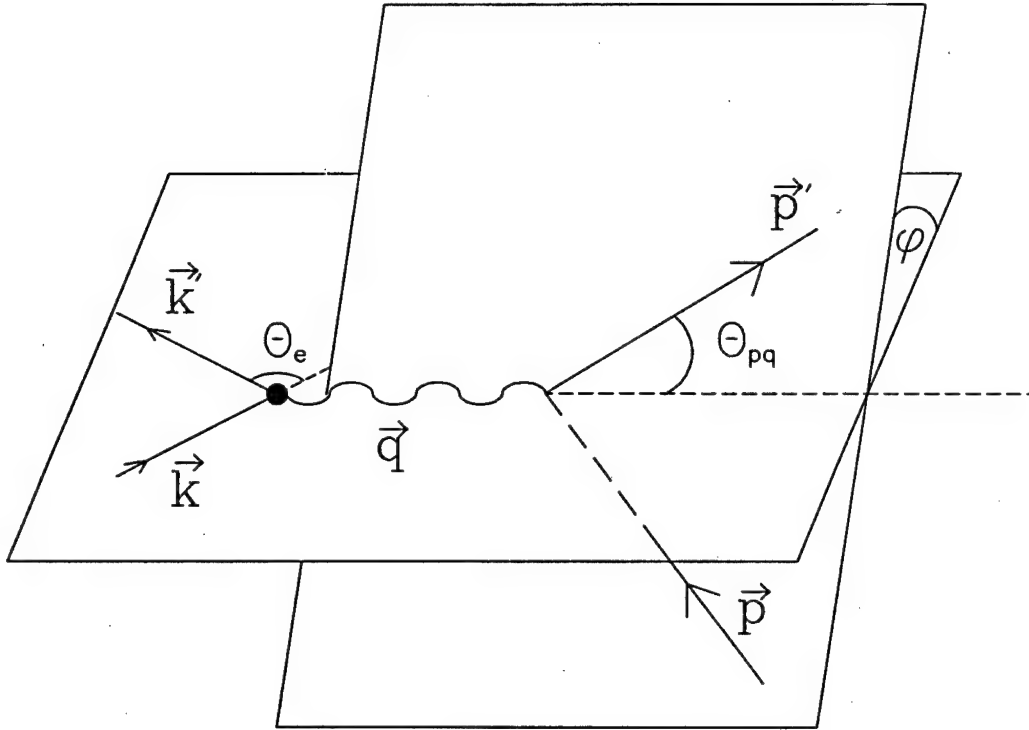
Measurement of proton polarizations necessitates use of the coincidence $(e, e' p)$ reaction rather than the simpler (e, e') reaction described in the previous chapter. Figure 2.1 shows an $(e, e' p)$ reaction. (Our reaction was actually $(\vec{e}, e' \vec{p})$ since the incoming electron and outgoing proton polarizations were known, but that does not affect the coincidence kinematics.) The angle θ_{pq} between \vec{p}' and \vec{q} is given by

$$\theta_{pq} = \cos^{-1} (\hat{p}' \cdot \hat{q}) \quad . \quad (2.1)$$

“Parallel kinematics” occur when \vec{p}' and \vec{q} are parallel and θ_{pq} equals 0 or 180 degrees. The angle between the scattering planes of the electron and the proton is

$$\begin{aligned} \phi_{planes} &= \cos^{-1} \left[\frac{(\vec{k} \times \vec{k}') \cdot (\vec{q} \times \vec{p}')}{|\vec{k} \times \vec{k}'| |\vec{q} \times \vec{p}'|} \right] \\ &= \tan^{-1} \left[\frac{\vec{p}' \cdot (\hat{q} \times \vec{k}_{\perp})}{\vec{p}' \cdot \vec{k}_{\perp}} \right] , \end{aligned} \quad (2.2)$$

where $\vec{k}_{\perp} = \vec{k} \times \hat{q}$. The first equation is easier to visualize while the second is better for computational purposes. It allows the quadrants to be easily determined since the numerator (denominator) is positive in quadrants 1 and 2 (1 and 4) and negative in 3 and 4 (2 and 3). If ϕ_{planes} equals 0 or 180 degrees the kinematics are called “in-plane kinematics”. For a hydrogen target it is always the case that $\theta_{pq} = 0^\circ$ and $\phi_{planes} = 0^\circ$.

Figure 2.1 The $(e, e' p)$ reaction.

2.2 Polarizations

Measuring the outgoing proton's polarization requires a second scattering. In our case this is done by scattering the protons from carbon nuclei in graphite blocks in the polarimeter. The \vec{p} - ^{12}C angular distribution is ^[30]

$$I(\theta, \phi) = I_0(\theta) [1 + A_c(\theta) \vec{p}_B^{fp} \cdot \hat{n}] \quad , \quad (2.3)$$

where $I_0(\theta)$ is the angular distribution for no polarization, $A_c(\theta)$ is the analyzing power, \vec{p}_B is the transverse polarization of the proton before it scatters, and

[30] E. Aprile-Giboni *et al.*, Nucl. Inst. Meth. **215**, 147 (1983).

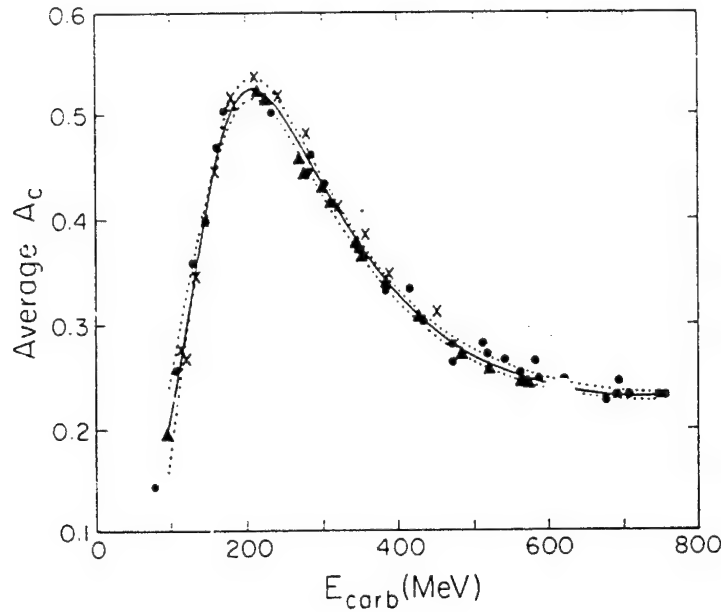


Figure 2.2 The angle-averaged (5° - 20°) \vec{p} - ^{12}C analyzing power as a function of proton energy.

$\hat{n}(= \hat{p}' \times \hat{p}'' / |\hat{p}' \times \hat{p}''|)$ lies in the plane of the second scattering. For our polarimeter's coordinate system (described in section 4.1.4) this leads to:

$$I(\theta, \phi) = I_0(\theta) [1 - p_x^{fp} A_c(\theta) \sin \phi + p_y^{fp} A_c(\theta) \cos \phi] \quad (2.4)$$

The analyzing power is a function of θ and T_p , the proton's kinetic energy. Figure 2.2 ^[31] shows the angle-averaged analyzing power as a function of T_p . Notice its peak at 200 MeV. Our experiment's kinematics were chosen so that the proton kinetic energies would range near this value. Figure 2.3 ^[30] shows the analyzing power's θ -dependence for a given proton energy. At small angles ($\sim < 3^\circ$) the $^{12}\text{C}(p, p')$ elastic cross section, as shown in figure 2.4, is dominated by multiple Coulomb scattering which has zero analyzing power. These events,

[31] M.W. McNaughton *et al.*, Nucl. Inst. Meth, **A241**, 435 (1985).

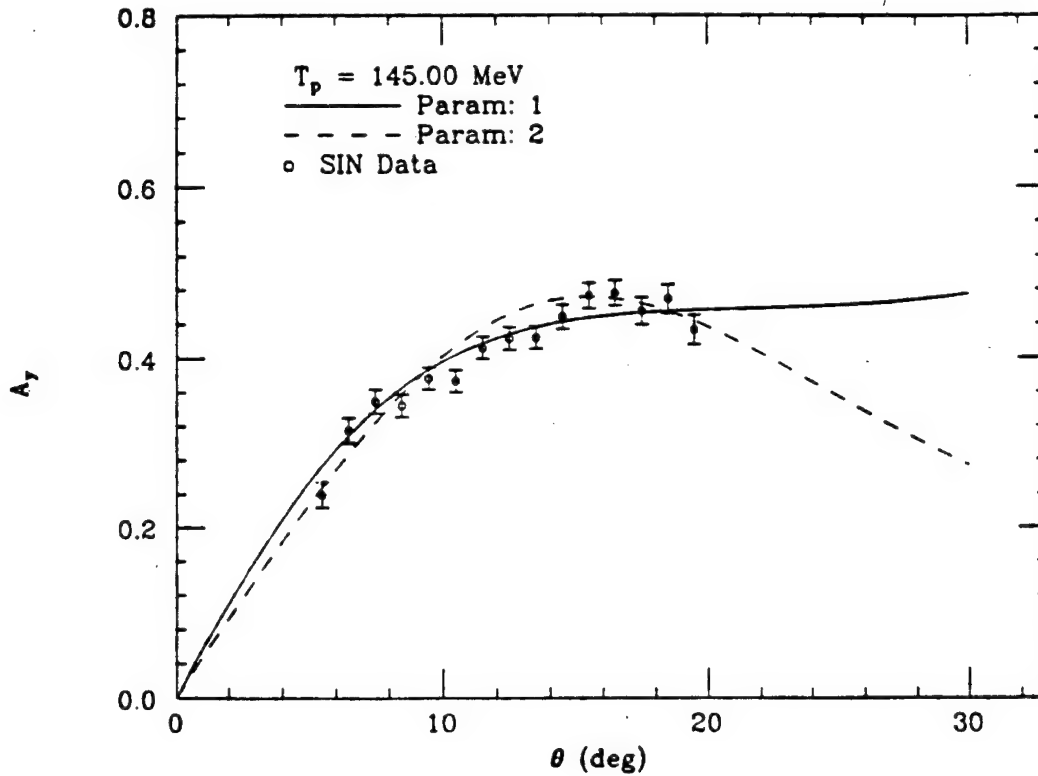


Figure 2.3 θ -dependence of $A_c(\theta)$ for a given proton energy.

however, account for a large majority of all the scattering events. Hence there is a need for the experimental hardware to reject small-angle events. Since the cross section decreases with θ , the useful events are primarily in the range from 5° - 20° .

Assuming conservation of angular momentum and parity, an electron that is longitudinally polarized will, in the first Born approximation, only transfer longitudinal and transverse polarizations for in-plane kinematics. Normal polarization may, however, be induced by final state interactions. Thus normal polarization is independent of the electron beam's helicity. For hydrogen, there aren't any final state interactions. (Two-photon exchange, however, can result in a very small normal polarization.)

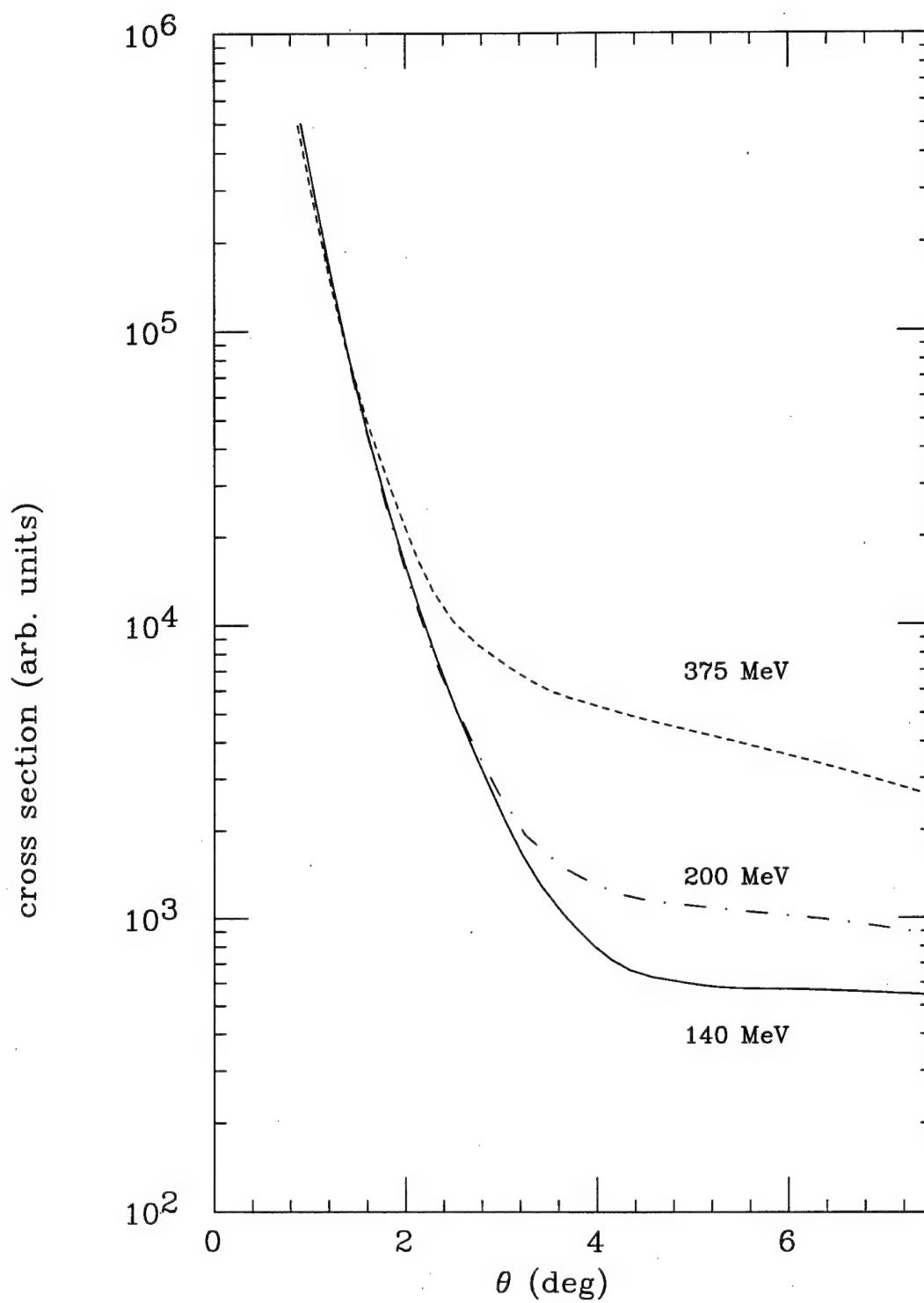
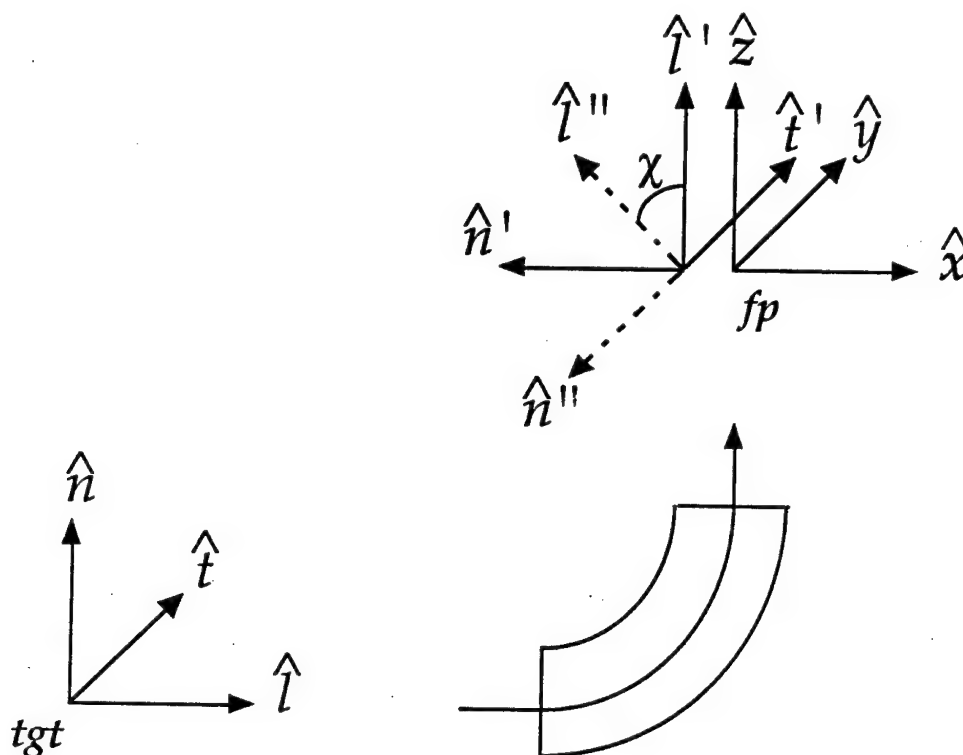


Figure 2.4 Proton-carbon elastic cross section vs. scattering angle.



$\hat{n}', \hat{l}', \hat{t}'$ momentum c.s. @ fp

$\hat{n}'', \hat{l}'', \hat{t}''$ spin c.s. @ fp

Figure 2.5 Transformation of target polarization to focal plane coordinates. χ is the angle the proton's spin precesses relative to its momentum.

Equation 2.4 allows for the determination of only two of the three polarization components. If precession of spin occurs due to magnetic fields between the target and the focal plane, however, it is possible to extract the third polarization component. For a vertically-bending proton spectrometer,

one must take into account the rotation displayed in figure 2.5:

$$\begin{aligned}\hat{x}_{fp} &= -\cos \chi \hat{n}_{tgt} - \sin \chi \hat{l}_{tgt} \\ \hat{y}_{fp} &= \hat{t}_{tgt} \\ \hat{z}_{fp} &= -\sin \chi \hat{n}_{tgt} + \cos \chi \hat{l}_{tgt}\end{aligned}\quad (2.5)$$

where χ is the angle the spin precesses relative to the momentum. (χ is discussed further in chapter 3.) Since \hat{n}_{tgt} is helicity-independent while \hat{l}_{tgt} is not, they can be separated by making measurements at both helicity states using the relationships:

$$\begin{aligned}p_n^{tgt} &= -\frac{p_n^{fp}(+h) + p_n^{fp}(-h)}{2 \cos \chi} \\ p_l^{tgt} &= -\frac{p_n^{fp}(+h) - p_n^{fp}(-h)}{2 \sin \chi}\end{aligned}\quad (2.6)$$

Equation 2.4 becomes:

$$I(\theta, \phi) = I_0(\theta) [1 - (p_n^{tgt} \cos \chi + p_l^{tgt} \sin \chi) A_c(\theta) \sin \phi - p_t^{tgt} A_c(\theta) \cos \phi] \quad , \quad (2.7)$$

where the p_n^{tgt} term should be near zero for hydrogen. Using this equation, the polarizations at the target can be measured if one knows χ and the analyzing power. As is shown in appendix A, knowing p_l and p_t allows one to determine the ratio G_E/G_M by the relationship:

$$\frac{p_t^{tgt}}{p_l^{tgt}} = -\frac{2M}{(E + E') \tan \frac{\theta}{2}} \frac{G_E}{G_M} \quad .$$

It is also possible to measure the beam helicity with the FPP using the target polarizations: [29]

$$\begin{aligned}h &= \frac{p_l^{tgt} \sin \chi}{\frac{E+E'}{M_p} \sin \chi \sqrt{\tau(1+\tau)}} \\ &\times \left[\left(\frac{E+E'}{2M_p} \right)^2 \sin^2 \chi \left(\frac{p_t^{tgt}}{p_l^{tgt} \sin \chi} \right)^2 + \tau [\cot^2(\frac{\theta_e}{2}) + 2(1+\tau)] \right]\end{aligned}\quad (2.8)$$

Chapter 3

Experimental Equipment Setup

3.1 Accelerator Facility

This experiment was performed at the Bates Linear Accelerator Center - a facility operated by the Massachusetts Institute of Technology (M.I.T.) that is located in Middleton, Massachusetts. Figure 3.1 shows a layout of the laboratory. The accelerator is designed to accelerate electrons (either polarized or unpolarized) in the 100-1000 MeV range with beam currents up to 50 μA . Beam energies above approximately 490 MeV are achieved by routing the beam through a recirculator for a second pass through the accelerator. This experiment used polarized electrons of approximately 580 MeV and was singles-rate limited to currents of less than 20 μA . The beam pulses ranged from 12 to 17 μsec long and the beam's pulse repetition rate was 600 Hz for a duty factor of 1%. Bates's South Hall Ring, a pulse stretching device, should produce a duty factor of 85% but was not available for our use.

This experiment used the South Hall's beam line B, which is detailed in figure 3.2. The beam energy is determined to about two-tenths of a percent using the calibrated EB1 chicane magnet. Three beam line toroids - BT1, BT2, and BT3 - measure the charge passing through the beam line. BT3 was connected to a Brookhaven Instrument Co. (BIC) current integrator which was calibrated by injecting a known current into a single loop ("Q-loop") in the toroid's transformer. Charge integration was started and stopped by the experimental gate and the integrator's output was recorded in a scaler. BT1



Figure 3.1 *Layout of Bates Linear Accelerator Center.*

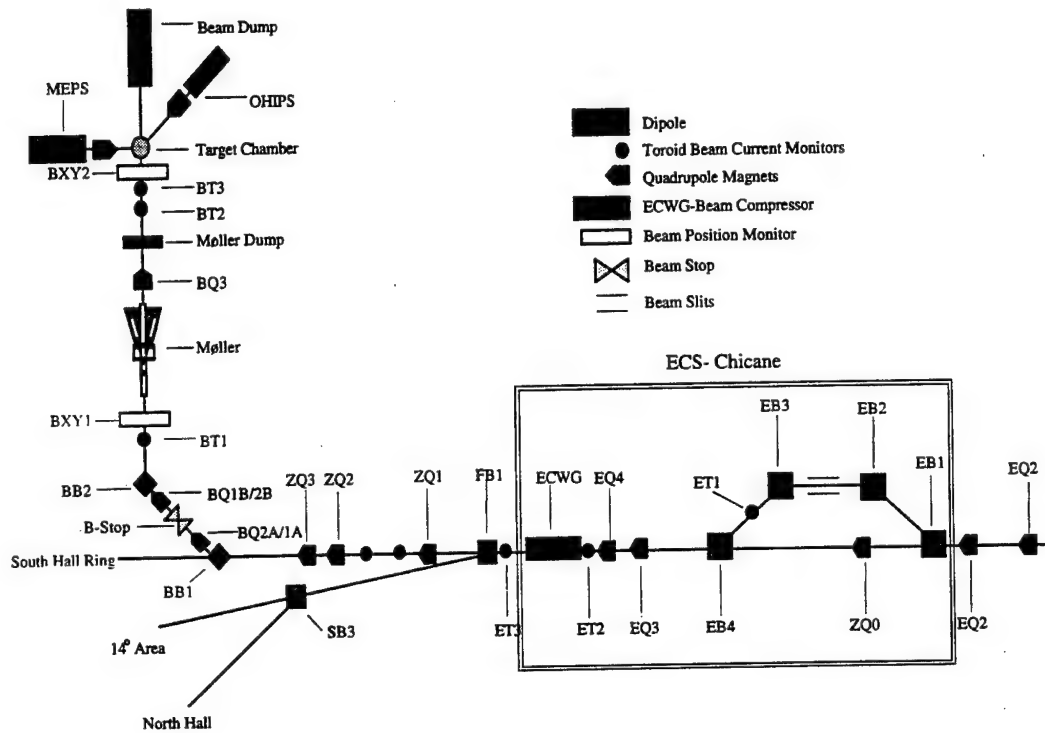


Figure 3.2 Beam line B layout.

and BT2, conversely, went to a charge integrator that was gated by the AND of the experimental gate with the computer-not-busy. This integrator's output went to an ADC, allowing the charge in each beam pulse to be individually measured. Of every 600 beam bursts, 20 contained no electrons, providing a pedestal measurement for the ADC which was subtracted from the measured charge to determine the actual charge delivered. BT1 and BT2 were calibrated in the same manner as BT3 so that we knew the nC/channel in the ADC.

Also in the beam line are several beam position monitors. (We used two.) These monitors are actually resonant cavities with dipoles at both ends. Depending on the beam's position, the different ends sense the passing beam's electromagnetic field at different times, allowing the beam position to

be determined. There is also a BeO flip target* 1 m upstream from the target for viewing the beam's position. Photomultiplier tubes were used to monitor the beam's halo. One was located near the target while another was near the Møller polarimeter. The polarimeter is the last major component of the B beam line and will be described in the next section.

3.2 Polarized Beam

3.2.1 Polarized Source

This experiment used a polarized beam of 25 to 35 percent polarization and currents up to about $20\mu\text{A}$. The accelerator's polarized injector is illustrated in figure 3.3. The longitudinally polarized electrons are produced from a Gallium-Arsenide crystal using circularly polarized laser light. The electrons are then accelerated to 60 kV in the photocathode gun and then an additional 320 kV in the source's accelerating column. A Wien filter can be used at this point to rotate the beam's polarization. Two 45° magnets then bend the beam to inject it into the main accelerator line. At this point its 380 kV injection energy is the same as that of the unpolarized beam when it comes out of its thermionic source. The injector is differentially pumped using ion pumps (which have no moving parts) with a vacuum in the vicinity of the crystal of $\approx 10^{-11}$ torr for hydrogen and $\approx 10^{-13}$ torr for more damaging water and carbon. [32]

The laser light used in the injector is from a 9 watt Ti-Sapphire laser which is optically driven by a 30 watt CW argon laser. The argon laser light is pulsed with a repetition rate of 600 Hz using a mechanical chopper (a slotted

* A flip target is a target that can quickly be put into the beam line with the press of a button or the flip of a switch, but has only one setting rather than an adjustable position range.

[32] M. Farkhondeh, private explanatory tour of source.

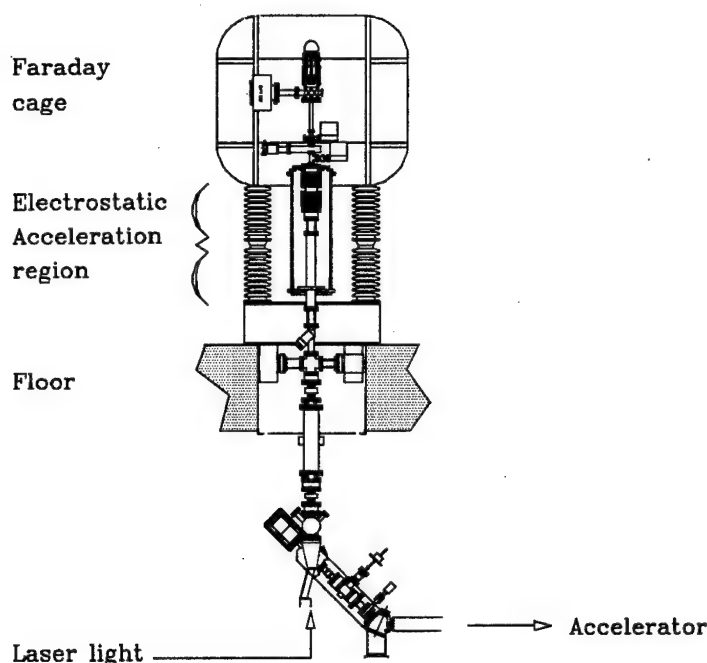


Figure 3.3 Layout of polarized source.

wheel), which increases the power output of the Ti-Sapphire laser. The argon laser's output lies in the 450-500 nm range while the Ti-Sapphire laser's light is at or near 752 nm. The laser beam's intensity can be modified from the control room prior to entering the injector. Pockels cells are used to set the beam burst size and to change the linearly polarized light to right or left circularly polarized. (A Pockels cell is an electro-optical device containing a birefringent crystal whose phase retardation is proportional to the applied voltage, allowing the polarization of the incident beam to be changed. ^[33]) The beam's helicity is flipped on a pulse-to-pulse basis. Each cycle of the 60 Hz line voltage is divided into 10 time bins. The helicity for the first 10 bins is (pseudo-)randomly

^[33] E. Hecht, *Optics*, Addison-Wesley, (1987).

determined while the next 10 bins are the complement of the previous 10. Then there are random bins again and so on.

The GaAs crystal has a band gap of 1.52 eV, with the $S_{1/2}$ state serving as the conduction band and the $P_{3/2}$ state serving as the valence band. For positive(negative) helicity light, optical selection rules require $\Delta m_j = +1(-1)$. For positive(negative) helicity light three times as many electrons go to the $m_j = -1/2(+1/2)$ state as to the $m_j = +1/2(-1/2)$ state, giving a theoretical polarization of 50%.^[34] We typically had polarization of 25% to 35%. Strained crystals (thin GaAs grown on a $\text{GaAs}_{(1-x)}\text{P}_{x(=0 \rightarrow 0.29)}$ buffer) remove the m-state degeneracy in the $P_{3/2}$ state so that polarizations on the order of 80% can be achieved. This was tried for our experiment but the quantum efficiency (the number of electrons produced per incident photon) was too low.

The GaAs crystal is coated with a thin film (< 1 atomic layer) of Cs and NF_3 to reduce its work function and allow electrons in the conduction band to be emitted from the crystal. The quantum efficiency of the crystal was around 1%. The quantum efficiency is very sensitive to surface contamination so occasionally the crystal needs to be reactivated. This procedure takes about an hour. First the surface of the crystal is heated. Then it is sprayed alternatively with Cs and NF_3 several times.

3.2.2 Spin Precession in Beam

After coming out of the polarized source, the longitudinally polarized beam goes through a 360° bend in the recirculator (if the energy desired is high enough to warrant this) and a 90° bend to get into the South Hall. Due to the precession of spin this will change the direction of the beam's polarization.

^[34] D.T. Pierce *et al.*, Rev. Sci. Inst. **51**, 478 (1980).

This can be compensated for by using the Wien filter, which rotates the spin using crossed electron and magnetic fields. There are, however, certain “magic” energies which do not require the use of the Wien filter. Our energy, 574 MeV was one of these.

The spin precession of a charged particle traveling in an electromagnetic field is given by the Thomas equation: ^[35]

$$\frac{d\vec{s}}{dt} = \frac{e}{mc} \vec{s} \times \left[\left(\frac{g}{2} - 1 + \frac{1}{\gamma} \right) \vec{B} - \left(\frac{g}{2} - 1 \right) \frac{\gamma}{\gamma + 1} (\vec{\beta} \cdot \vec{B}) \vec{\beta} - \left(\frac{g}{2} - \frac{\gamma}{\gamma + 1} \right) \vec{\beta} \times \vec{E} \right] . \quad (3.1)$$

In our case $\vec{E} = 0$ and $\vec{\beta} \cdot \vec{B}$ is small so the spin precession reduces to

$$\begin{aligned} \frac{d\vec{s}}{dt} &= \frac{e}{mc} \vec{s} \times \left(\frac{g}{2} - 1 + \frac{1}{\gamma} \right) \vec{B} = \vec{s} \times \vec{\omega}_s \\ \vec{\omega}_s &= \frac{e}{mc} \left(\frac{g}{2} - 1 + \frac{1}{\gamma} \right) \vec{B} . \end{aligned} \quad (3.2)$$

Likewise, the equation of motion for a charged particle moving in an electromagnetic field is

$$\frac{d\vec{p}}{dt} = e(\vec{E} + \frac{\vec{v}}{c} \times \vec{B}) . \quad (3.3)$$

Using $\vec{E} = 0$ again and the relationship $\vec{p} = m\gamma\vec{v}$ gives

$$\begin{aligned} \frac{d\vec{p}}{dt} &= e \left(\frac{\vec{p}}{\gamma mc} \times \vec{B} \right) = \vec{p} \times \vec{\omega}_p \\ \vec{\omega}_p &= \frac{e}{\gamma mc} \vec{B} . \end{aligned} \quad (3.4)$$

The total spin precession with respect to the beam’s direction can now be written as:

$$\begin{aligned} \Delta\omega &= \omega_s - \omega_p = \frac{eB}{mc} \left(\frac{g}{2} - 1 \right) \\ &= \omega_p \gamma \left(\frac{g}{2} - 1 \right) . \end{aligned} \quad (3.5)$$

^[35] J.D. Jackson, *Classical Electrodynamics*, John Wiley & Sons, (1975).

There are two areas in the accelerator where the beam is bent: the recirculator (if used) and the 90° entrance to the South Hall; so that the final spin angle χ_s^{final} relative to the beam is

$$\Delta\chi_s^{final} = \left(\frac{g}{2} - 1\right)(\chi_p^{recirc}\gamma^{recirc} + \chi_p^{hall}\gamma^{hall}) , \quad (3.6)$$

where $\gamma^{recirc} = \frac{E^{recirc}}{mc^2}$ and $\gamma^{hall} = \frac{E^{final}}{mc^2}$. The “preaccelerator” beam energy is 20 MeV. Therefore the equation relating the final beam energy with the beam energy after the first pass through the accelerator but before being bent through the recirculator is $E^{final} = E^{recirc} + (E^{recirc} - 20)$ so that γ^{recirc} can be expressed as: $\gamma^{recirc} = \frac{E^{final} + 20}{2mc^2}$. Using $\chi^{recirc} = 2\pi$ and $\chi^{hall} = \pi/2$, the “magic” energies can now be determined by setting $\Delta\chi^{final} = n\pi$. The South Hall’s “magic” energies are 280 (which doesn’t use the recirculator), 574, and 868 MeV for $n = 1, 2, 3$. We used 574 MeV for our beam energy.

3.2.3 Møller Polarimeter

Approximately 20m upstream from the target on beam line B is a Møller polarimeter to measure the beam polarization. It employs elastic scattering of the spin polarized electron beam with the spin polarized Møller target electrons. The device and the theory behind its operation are described in Arrington *et al.* [36] and Wagner *et al.* [37]

The cross section for polarized, elastic electron-electron scattering may be written as

$$\left(\frac{d\sigma}{d\Omega}\right) = \left(\frac{d\sigma_0}{d\Omega}\right) \left(1 + \sum_{i,j} P_B^i A_{ij} P_T^j\right) , \quad (3.7)$$

[36] J. Arrington *et al.*, Nuc. Inst. Meth. **A311**, 39 (1992).

[37] B. Wagner *et al.*, Nuc. Inst. Meth. **A294**, 541 (1990).

where $\frac{d\sigma_0}{d\Omega}$ is the unpolarized cross section, $P_B^i(P_T^j)$ are the polarization components of the beam(target), and A_{ij} are the nine asymmetries. z is the direction of the beam and x lies on the detected scattering plane. In the extreme relativistic limit, the asymmetries are, to lowest order in QED:

$$\begin{aligned} A_{zz} &= -\frac{(7 + \cos^2 \theta_{cm}) \sin^2 \theta_{cm}}{(3 + \cos^2 \theta_{cm})^2} \\ A_{xx} &= -A_{yy} = -\frac{\sin^4 \theta_{cm}}{(3 + \cos^2 \theta_{cm})^2} \\ A_{zz} &= A_{zz} = -\frac{2 \sin^3 \theta_{cm} \cos \theta_{cm}}{\gamma(3 + \cos^2 \theta_{cm})^2} \\ A_{xy} &= A_{yx} = A_{yz} = A_{zy} = 0 \end{aligned} \quad (3.8)$$

where γ is the Lorentz factor relating the lab and center-of-mass frames. By setting $\theta_{cm} = 90^\circ$ these reduce to $A_{zz} = -\frac{7}{9}$ and $A_{xx} = -A_{yy} = -\frac{1}{9}$ with the cross-terms going to zero.

By taking measurements in both longitudinal directions and assuming that the beam and target are polarized only along the beam, the measured asymmetry should be

$$A = A_{zz} P_B^z P_T^z \quad (3.9)$$

where $P_T^z = P_T \cos \theta_T$. (θ_T is the target angle.) Since the target can only be magnetized in its plane, it was typically tilted at a relatively small target angle of $\pm 30^\circ$ with respect to the beam so that the longitudinal polarization could be measured. Assuming $\cos \theta_B \approx 1$ and averaging the asymmetries gives

$$P_B = -\frac{9}{7P_T \cos(30^\circ)} \frac{A_{+30^\circ} + A_{-30^\circ}}{2} \quad (3.10)$$

Due to Mott scattering and other backgrounds, the measured asymmetry is actually

$$A_{meas} = A \left(\frac{1}{1 + B/S} \right) \quad (3.11)$$

where B is the background rate and S is the Møller scattering rate. Our signal to background ratio was approximately 2:1. Using the two Čerenkov detectors in coincidence mode would have reduced background but would have imposed more stringent requirements on beam position stability, detector efficiency, and mechanical alignments. Thus we used them for separate measurements (singles mode). Each Møller run included both a so-called real scan to determine the signal to background ratio and a peakscan to accumulate statistics for the asymmetry measurement. The scans were performed by varying the current of the quadrupole used to bend the scattered electrons away from the beam line and taking measurements for set periods of time. The polarization was measured about once a day or whenever the polarized source's crystal was reactivated.

Figure 3.4 shows the polarimeter's layout. There are two thin foil targets ($13\text{ }\mu\text{m}$ and $25\text{ }\mu\text{m}$ thick) of Supermendur, an alloy consisting of 49% Fe, 49% Co, and 2% "Vacoflux". Also in the target ladder are BeO and Al targets used for alignments and an empty target to allow the beam to pass through. The target is polarized by a magnetic field from Helmholtz coils around the target. The field reaches nearly 150 Gauss and the target polarization measures about 8%. Downstream from the target is a lead disk collimator to define the scattering angle of interest. Our scattering angle was 2.42° , which is 90° in the center-of-mass system. Behind the collimator is a 25 cm diameter quadrupole magnet which bends the scattered electrons away from the beam line to the Čerenkov detectors while letting the main beam pass through unaffected.

3.3 Target

This experiment was the first to use a new target built at M.I.T.-Bates called the Basel Loop target, pictured in figure 3.5. It had separate liquid hydrogen and deuterium targets as well as solid BeO (34.51 mg/cm^2) and

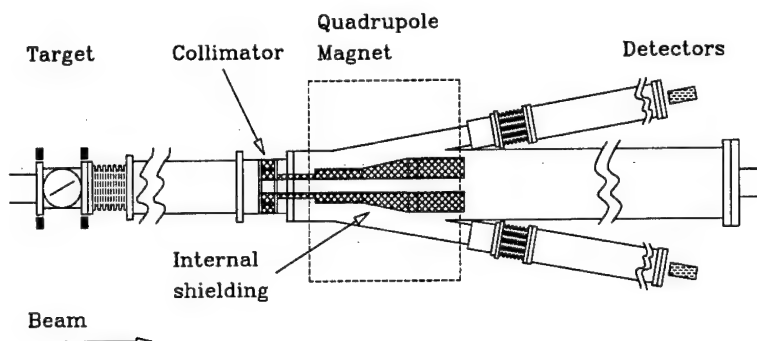


Figure 3.4 *Møller polarimeter.*

C (91.46 mg/cm^2) targets and a blank target. The liquid target loops were identical and were cooled in series to approximately 20 K by gaseous He from a 200 W refrigerator. The temperatures were measured with diodes and carbon glass resistors. Internal heaters were used to maintain a constant temperature as the beam was turned off and on. Internal fans were used to lessen local boiling and to improve the heat exchanger's cooling efficiency. The gas-handling systems for the two loops were separate - the chief difference being that the deuterium loop was designed to vent to a storage tank due to deuterium's expense. Pressure transducers were located at the gas fill lines and the target pressure was ideally slightly above 1 atmosphere. Each loop had a capacity of 1.5 liters. The thin target cell walls were made of Havar, which has the following composition: 42% Co, 19.5% Cr, 19.1% Fe, 12.7% Ni, 2.7% W, 2.2% Mo, 1.6% Mn, and 0.2% C. Further target properties are listed in table 3.1. An IBM-compatible personal computer in the counting bay was used to control the heaters and monitor the temperature and pressure.

3.4 MEPS

The scattered electrons were detected in the Medium Energy Pion

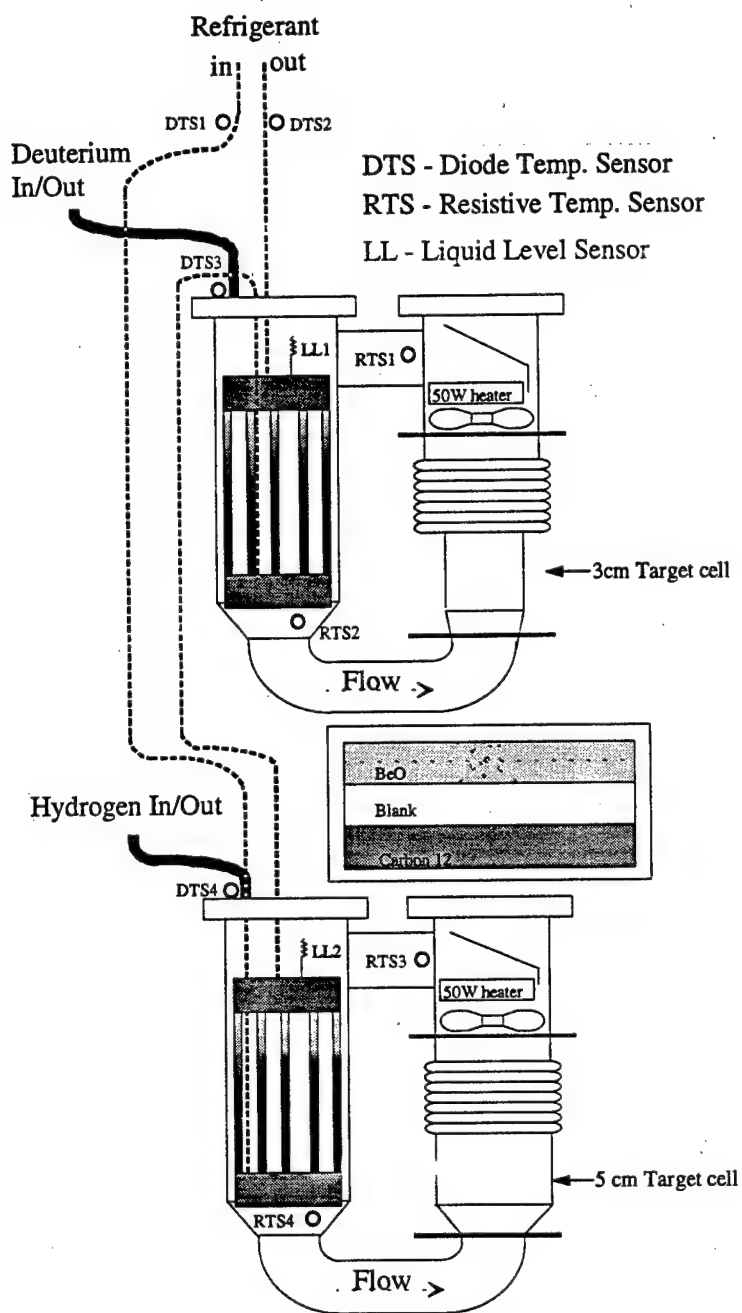


Figure 3.5 Basel Loop target.

Target	LH ₂	LD ₂
Cell Diameter (cm)	5	3
Cell Wall Thickness (μm)	25.4	10.16
Cell Wall Density (g/cm^2)	0.042	0.017
Nominal Temperature (K)	20.3	23.7
Liquid Density (g/cm^3)	0.071	0.16
Liquid Density (g/cm^2)	0.36	0.48

Table 3.1 Target Parameters

Spectrometer (MEPS). The layout of the spectrometer is shown in figure 3.6 and some of its properties are listed in table 3.2. MEPS is a QQSD spectrometer (two quadrupoles followed by a split dipole). The focusing in the vertical bend plane (the momentum dispersion direction) is point-to-point ($\langle x|\theta \rangle = 0$). In the transverse plane, however, it is parallel-to-point ($\langle y|y \rangle = 0$ and $\langle y|\phi \rangle \neq 0$), allowing the scattering angle (ϕ) to be better determined since the well determined focal plane y position is directly proportional to the scattering angle. (These TRANSPORT matrix elements are described in more detail in chapter 4.) The magnets' power supplies were set in the counting room via a computer dedicated to that purpose. The dipole field was measured internally using a Rawson-Lush probe while the quadrupole fields were assumed to scale linearly with the magnets' currents. A 2-in thick lead collimator was at the front of MEPS. The dimensions of its opening were ± 2.59 cm vertically and ± 3.78 cm horizontally for an acceptance of 14 msr.

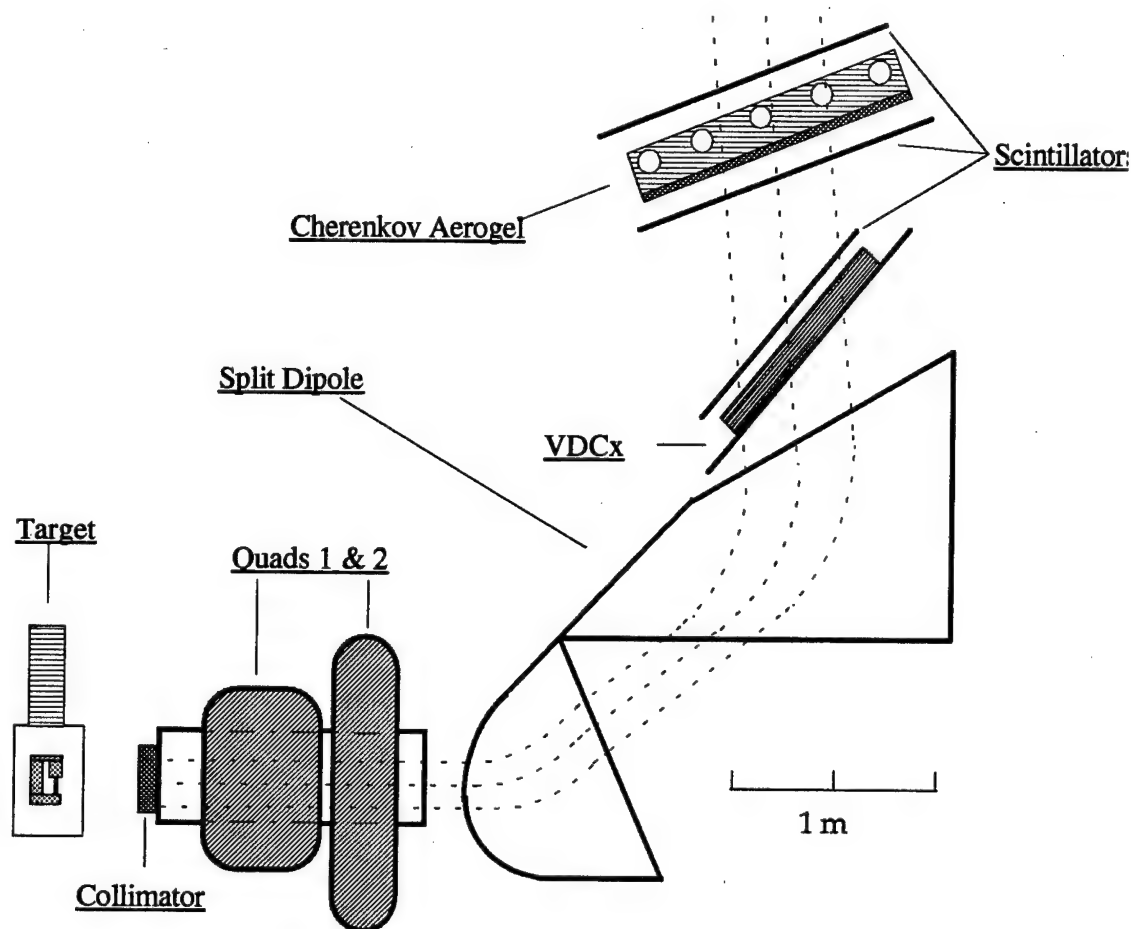


Figure 3.6 MEPS spectrometer layout.

The MEPS focal plane detector system consists of three scintillators, an aerogel Čerenkov detector, and a two-plane vertical drift chamber (VDCX, where the 'X' stands for the "crossed" planes). The aerogel had an index of refraction of 1.05 so that particles traveling at or above 95% the speed of light would produce Čerenkov radiation. Ten photomultiplier tubes (PMTs) aligned transverse to the momentum dispersion direction detected light in the diffusion cavity above the aerogel. This detector is used to differentiate electrons from pions, but at our kinematics there were few pions so we did not use the Čerenkov detector's information.

Maximum Solid Angle	20 msr
Momentum Acceptance	$\pm 10\%$
Maximum Momentum	414 MeV/c
Momentum Resolution	$5 \cdot 10^{-4}$
Angular Range	$35^\circ - 140^\circ$
Radius of Curvature	0.75 m
Front Drift Distance	0.53 m
Flight Path	4.7 m
Bend Angle	110°
Focal Plane Dispersion	1.9 cm/%

Table 3.2 MEPS Parameters

3.4.1 MEPS Scintillators and Pilot

The three scintillators of the MEPS focal plane are made of NE-110 plastic. MS0 is directly above the VDCX and has dimensions of 17.8 cm by 58.4 cm. It is 1/4 inch thick. MS3 and MS4 are above and below the aerogel detector respectively. Both have an active area of 20.3 cm by 91.0 cm and are 1/8 inch thick. All three scintillators are each connected to two PMTs via Lucite light guides. The PMTs on MS3 and MS4 are at the ends but for MS0 they are attached next to each other on the side.

A coincidence of all three scintillators was used to generate the MEPS

June 29, 1994

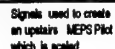


Figure 3.7 *MEPS pilot logic.*

pilot. * Figure 3.7 details the MEPS pilot logic. After the six scintillator PMT signals were discriminated the signal-pairs from MS3 and MS4 were

* *Pilot* is the French word for trigger. We referred to our individual spectrometer triggers as pilots, reserving the word *trigger* for the final data-readout signal.

sent to a meantimer, which makes the timing relatively independent of the the event position along the device. Due to the side-by-side placement of the PMTs for MS0, their signals were OR'ed instead. MS4MT was widened using a discriminator and MS3MT was delayed, so that it defined the timing of the 3-fold coincidence MEPS pilot (MPI). MPI was sent to OHIPS, the proton spectrometer, via a 90Ω 105ns cable for use in the trigger logic, as well as to be scaled and have its timing information recorded in a time-to-digital converter (TDC). The six analog PMT signals and the three logic signals (MS0OR, MS3MT, and MS4MT) were sent upstairs to the counting bay on 50Ω cable where they were scaled and sent to a TDC. The analog signals's pulse shape information was also recorded on an analog-to-digital converter (ADC). Amplification was necessary to send the signals upstairs. An upstairs (counting bay) version of MPI was also created to check for discrepancies against the downstairs (South Hall) one.

3.4.2 MEPS VDCX

The MEPS vertical drift chamber has two planes of 128 wires each. The wire planes of the two chambers are 3.81 cm apart. They are oriented orthogonally to one another and 45° relative to the dispersive and transverse directions. The active area of each plane is 7×25 inches. The anode wires are $20\ \mu\text{m}$ diameter gold-plated tungsten wire placed 4.23 mm apart. $50\ \mu\text{m}$ diameter beryllium-copper guard wires separate the anode wires forming field "cells", as shown in figure 3.8. Aluminized mylar at high voltage (≈ -9.0 kV) lies on both sides of each plane. The entire chamber is tilted with respect to the spectrometer's central momentum ray at an angle of approximately 45° so that a particle track will generate signals in several "cells". [38]

[38] D. Caditz, B.S. Thesis, M.I.T. (1983), unpublished (Bates Internal Report #85-04).

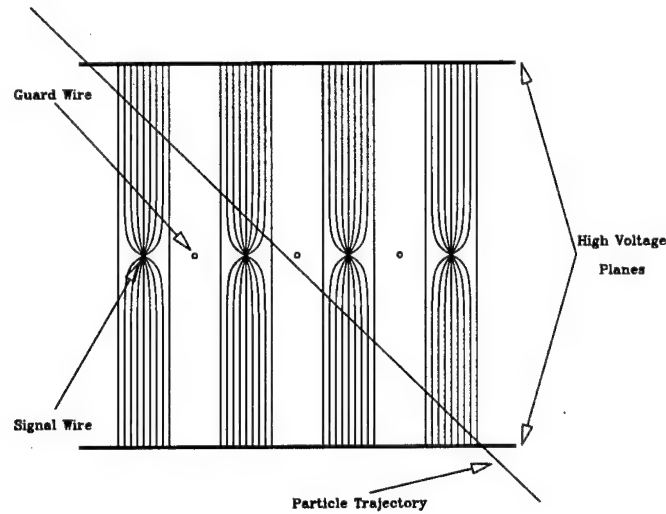


Figure 3.8 VDCX layout with field lines.

The chambers operate with a gas mixture of roughly 50% argon and 50% isobutane. When a charged particle travels through the chamber it ionizes argon atoms. The released electrons are accelerated by the electric field towards the anode wire and quickly achieve a terminal drift velocity of $\approx 5 \text{ cm}/\mu\text{s}$. The electrons also ionize other argon atoms producing an avalanche. The isobutane is used to absorb photons radiated by the excited argon atoms. Otherwise the photons can cause additional avalanches. Near the anode wire, however, the rapidly increasing electric field overcomes the quenching and the avalanche created is detected as a voltage pulse in the wire. ^[39] The maximum drift time for the MEPS planes is around 250 ns. The particle trajectories can then be determined by using the drift times recorded from the different anode wires. (This is discussed in the next chapter.)

^[39] W.R. Leo, *Techniques for Nuclear and Particle Physics Experiments*, Springer-Verlag, (1987).

The MEPS VDCX is instrumented with the LeCroy 4290 Drift Chamber Operating System (DCOS), consisting of 16 channel LeCroy 2735 amplifier/discriminator (a/d) cards, 32 channel 4291B TDCs, a 4298 system controller, and a 4299 databus interface. Figure 3.9 displays this system. Chamber artwork (applied circuit traces) carries signals from the VDCX wires to connectors for 16 channel twisted-pair, shielded ECL cable. (We typically referred to the shielded ECL cable as “black” cable due to its color and the unshielded cable as “ribbon” cable.) These cables go to the a/d cards, whose threshold can be set from upstairs. (We set them at 3 volts.) The signals then leave the VDCX hut on ribbon cables to the TDCs in a CAMAC (Computer Automated Measurement And Control) crate on the back of MEPS. The TDCs were operated in common stop mode and drift times for all the wires that fired during an event were read, allowing multiple particle trajectories. The system controller receives data from the TDCs through the CAMAC crate’s back plane and generates a stream of packed module and wire data words. The packed data is then sent upstairs through 50-channel flat ECL cable to a databus interface. This interface is necessary for the CAMAC readout system (which is described in section 3.8). The DCOS system can be calibrated using software to generate starts and stops within the system controller and to adjust the slopes and pedestals of the TDCs.

3.5 OHIPS

The proton arm for our experiment was the One-Hundred Inch Proton Spectrometer (OHIPS) to which we added a newly-built focal plane polarimeter (FPP). OHIPS is a QQD spectrometer whose magnets are controlled upstairs in the counting bay and whose dipole field is measured with a Rawson-Lush probe just like MEPS. Also, like MEPS, the focusing is point-to-point in the momentum dispersion direction ($\langle x|\theta \rangle = 0$), but, unlike MEPS, the focusing in

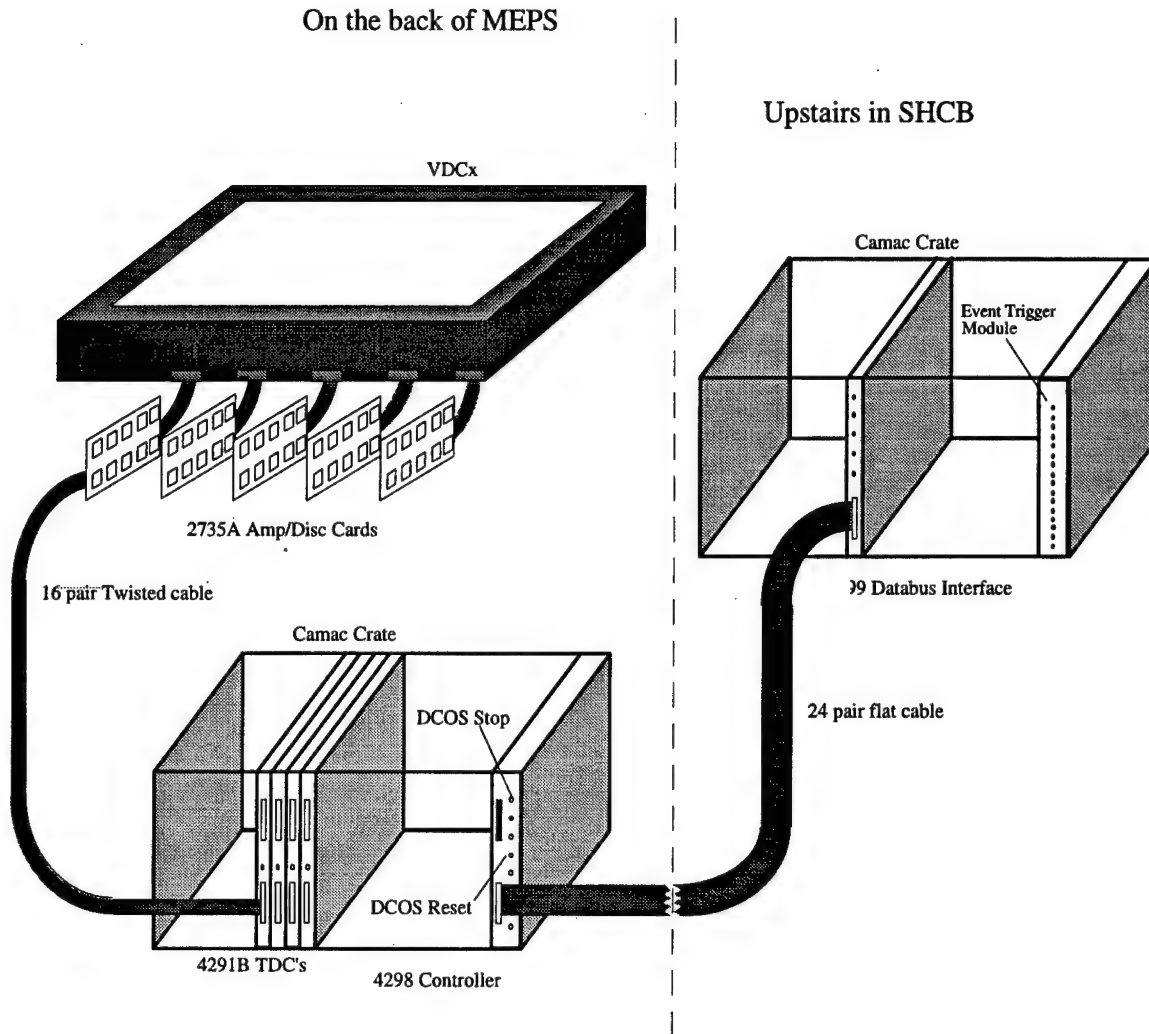


Figure 3.9 *DCOS system for the MEPS VDCX.*

the transverse direction is point-to-point ($\langle y|\phi \rangle = 0$) as well. This allows for better resolution of the scattering-point along the beam in an extended target and also allows the target walls to be excluded. The first quadrupole in OHIPS had a vertical focus and the second a horizontal focus. This focus is referred to as a "VH" or "reverse" focus and provides a large vertical angle acceptance but a smaller horizontal angle acceptance than a "HV" or "normal" focus. The collimator at the front of OHIPS was 5.1 cm thick and was beveled with

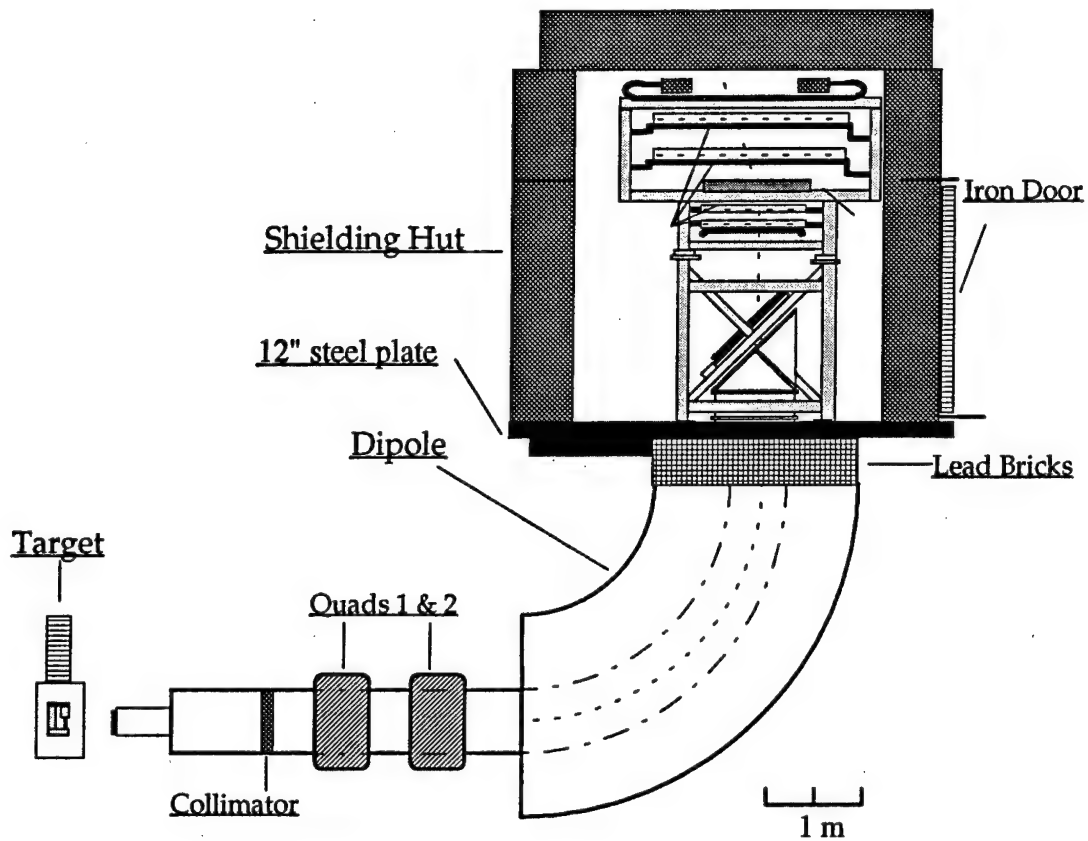


Figure 3.10 OHIPS layout.

frontface dimensions of ± 4.129 cm horizontally by ± 12.263 cm vertically and backface dimensions of ± 4.271 cm by ± 12.687 cm. The drift distance at the front of OHIPS can be adjusted to allow for increased angular acceptance at the expense of angular resolution, or vice versa. Figure 3.10 gives a sideview of OHIPS and table 3.3 lists some of OHIPS's properties. Please note that by equation 3.5, OHIPS's 90° bend precesses the spin relative to momentum by the angle $\chi = \gamma 161.4^\circ$.

Solid Angle	7.5 msr
Momentum Acceptance	$\pm 5\%$
Maximum Momentum	1300 MeV/c
Momentum Resolution	
Design	$1 \cdot 10^{-3}$
Best Obtained	$1.4 \cdot 10^{-3}$
Angular Range	$19^\circ - 140^\circ$
Radius of Curvature	100 in
Front Drift Distance	1.6 m
Flight Path	9.3 m
Bend Angle	90°
Focal Plane Dispersion	4.2 cm/%

Table 3.3 OHIPS Parameters

Many modifications were made to OHIPS in the fall of 1993 so that the FPP could be placed on top of it. The shielding hut was redesigned and made larger. To keep the weight under control the shielding walls were made thinner but it was still necessary to add cross struts to the shielding hut platform supports. An air conditioner and a dehumidifier were placed inside the shielding hut to make the climate suitable for operating the FPP whose a/d cards generated a lot of heat. Unfortunately, the air conditioner often dripped water on the FPP's discriminator card power supply so a gutter system had to be rigged up. A new support structure for the OHIPS VDCX was built to

facilitate the support of the FPP and also to allow for better alignment between the spectrometer, the VDCX, and the FPP. A new, larger electronics platform was put on the back of OHIPS to handle the FPP's additional electronics. The old wooden ladders on OHIPS were replaced with safer molded aluminum ladders and OHIPS got a fresh paint job.

3.5.1 OHIPS Focal Plane and Pilot

The proton arm focal plane detector system consisted of five scintillators, a VDCX, and the focal plane polarimeter. Figure 3.11 shows the focal plane including detail of the polarimeter. Scintillator OS0 was directly above the VDCX while FS1 was right below the first FPP wire chamber. FS2 consisted of three scintillators: FS2AB, FS2CD, and FS2EF; which were positioned above the large, top FPP wire chamber and overlapped slightly. Each scintillator had two PMTs attached to it via Lucite light pipes. Table 3.4 gives the dimensions of the scintillators.

Scintillator	Width (cm)	Length (cm)	Thickness (mm)
OS0	20.3	65.0	5.0
FS1	37.0	71.0	6.4
FS2(AB,CD,EF)	145.0	32.0	13.0

Table 3.4 OHIPS Scintillator Dimensions

As detailed in figure 3.12, the OHIPS pilot was generated by a

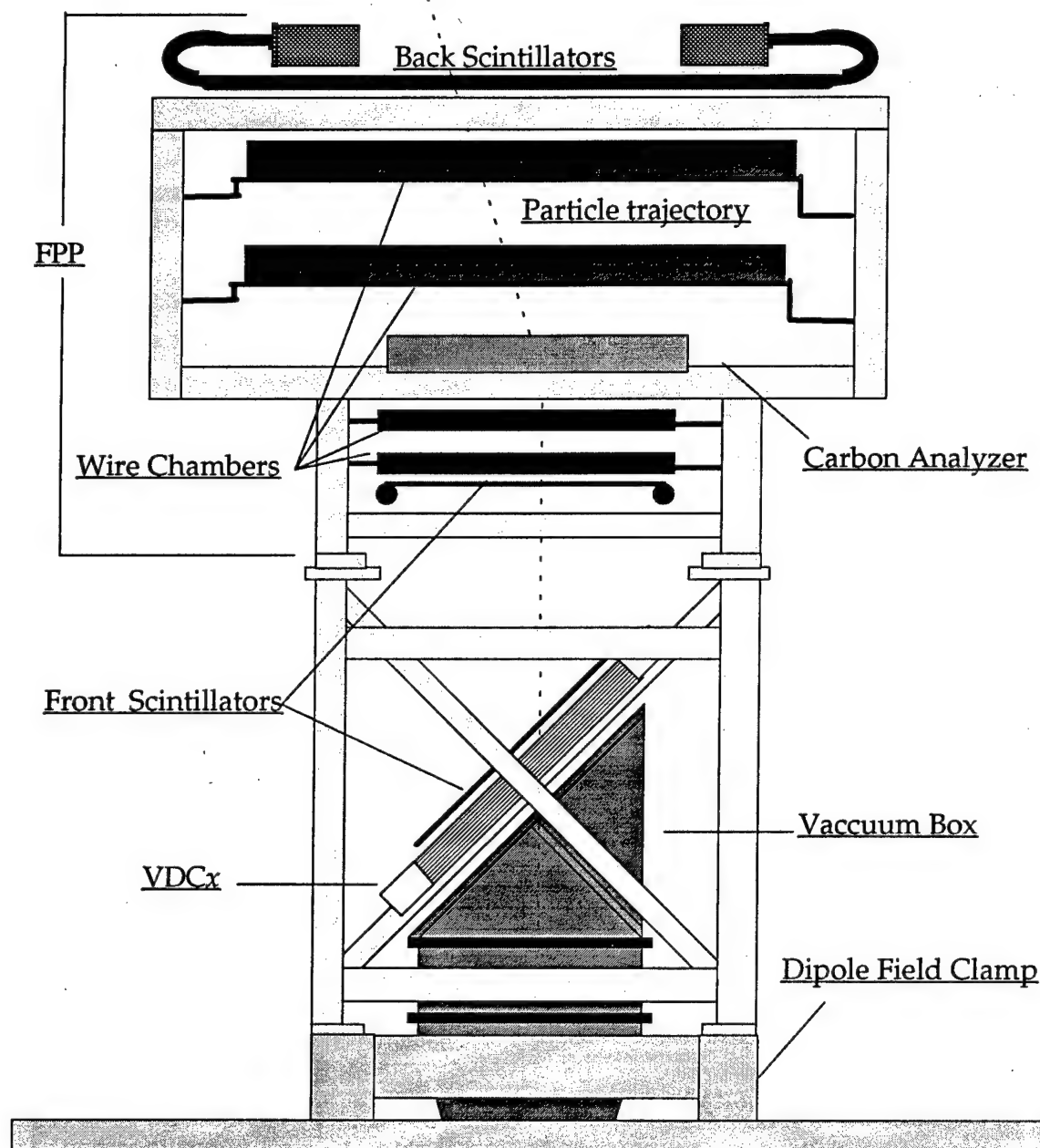


Figure 3.11 OHIPS focal plane including FPP detail.

coincidence of the the three scintillator planes. This can be thought of as the first (and simplest) level of a three-level FPP trigger (which will be described

fully in section 3.7). The ten scintillator PMT signals were fanned-out to ADCs and discriminators. The two discriminated signals for each scintillator were meantimed, producing five meantime signals that, together with the ten discriminated signals, were sent to a Phillips 761 NIM/ECL converter before being sent through ribbon cable and/or a LeCroy 4418 Programmable Delay Module (PDM) to a LeCroy 4434 Scaler, a LeCroy 4300B/4303 FERA/FERET TDC, and a LeCroy 2365 Programmable Logic Unit (PLU). Since the full trigger electronics take over 900 ns to generate the TDC start signal, the logic signals were delayed using the PDMs and long rolls of ribbon cable.

In the PLU the three FS2 meantimed-signals were OR'ed to produce FS2OR. This was looped back through the PLU so that it could be AND'ed with OS0MT and FS1MT to produce the OHIPS pilot (OPI). The timing was determined by OS0MT. Using software, it was easy to change the PLUs programming so that the pilot logic could be set up differently. With all of the looping back through PLUs, delaying through ribbon cables, and fanning-out through PDMs and ECL/NIM converters; our three-level electronics became rather complicated. A more in-depth description is given in McIntyre and Warren. [40]

3.5.2 OHIPS VDCX

The OHIPS VDCX is very much like MEPS's. It also has two crossed planes separated by 3.81 cm. The chamber is tilted approximately 45° with respect to the central momentum ray. Each plane has 128 wires, though we only read-out 110 of them. The chief difference between the two is the readout system. OHIPS uses a delay-line system rather than DCOS.

[40] J. McIntyre and G. Warren, Bates Technical Note #94-01.

this system only four wires per plane can be read out, unlike MEPS. Both ends of the delay line are TDC'ed and have distinct and different times. The left and right times for a signal occurring on anode wire n out of a total number of wires N on the delay line is:

$$\begin{aligned} t_R &= (n - 1)\tau + t_d \\ t_L &= (N - n)\tau + t_d \end{aligned} \quad (3.12)$$

where t_d is the drift time associated with the anode wire (as was pictured in figure 3.8). By taking the sum and difference of t_L and t_R , t_d and n can be solved for, respectively, as

$$t_d = \frac{(t_R + t_L) - (N - 1)\tau}{2} \quad (3.13)$$

and

$$n = \frac{(t_R - t_L) + (N + 1)\tau}{2\tau} \quad (3.14)$$

Using the wire numbers and drift times the particle trajectories can then be determined in the software.

3.6 FPP

This experiment inaugurated a focal plane polarimeter (FPP) on OHIPS. The FPP was built by a collaboration of the University of Virginia, M.I.T., and William & Mary over about a three year period. Figure 3.11 shows the FPP in detail. It consists of a graphite analyzer, four multiwire proportional wire chambers (MWPCs), and two scintillator planes (mentioned in the OHIPS discussion). The graphite lies above a pair of MWPCs and below a pair of larger MWPCs, allowing the particle's track to be determined both before and after it scatters in the analyzer. The FPP was calibrated at the Indiana University Cyclotron Facility (IUCF) in February 1993. This is described in appendix B.

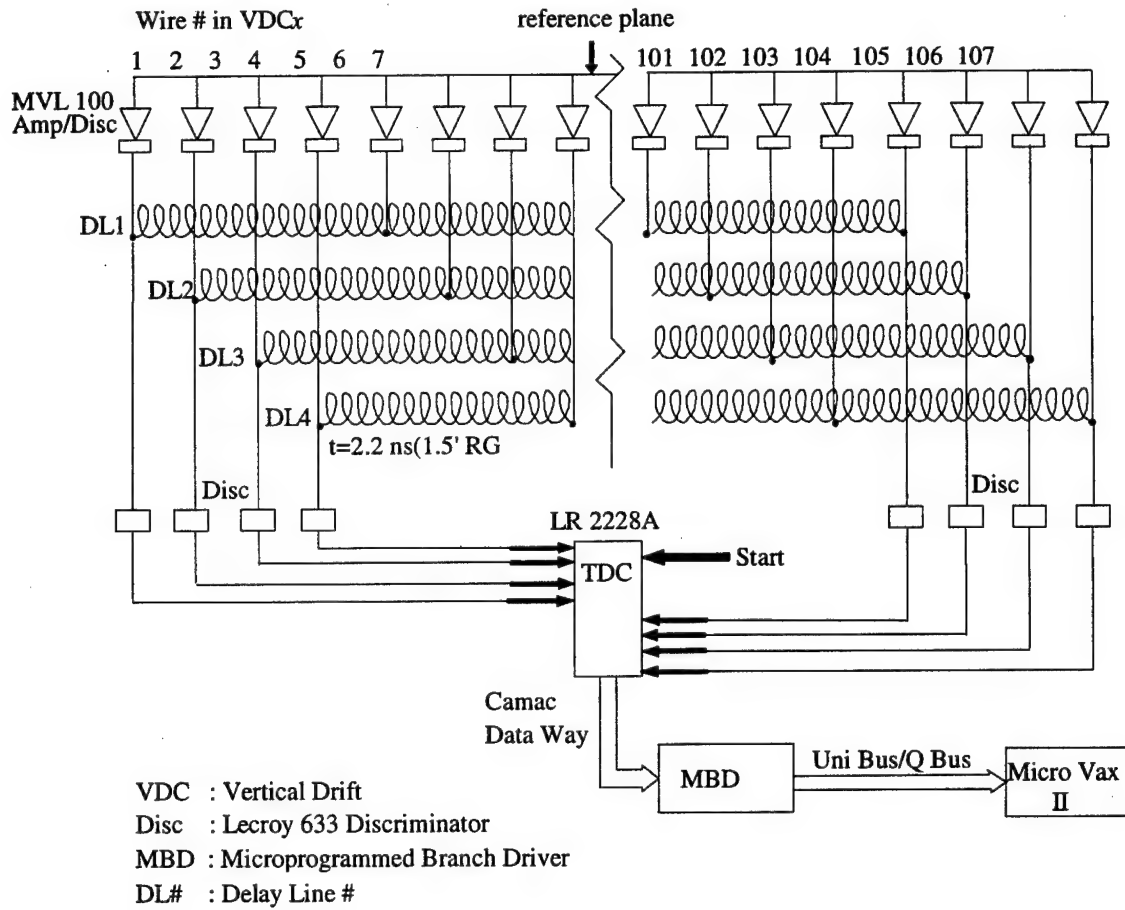


Figure 3.13 OHIPS delay line system.

The FPP was designed to satisfy four basic requirements: ^[41]

- 1) Resolution of scattering angle in graphite to $\leq 1^\circ$.
- 2) Able to reject small scattering angles ($\approx < 5^\circ$) quickly (substantially less than $1\mu\text{s}$).

^[41] R.W. Lourie *et al.*, IUCF Scientific and Technical Report, 135 (May 1992 - April 1993).

- 3) Complete azimuthal scattering angle coverage for 10% momentum acceptance and 20° scattering in the FPP.
- 4) Suitable for extended targets up to 10 cm in length.

Requirements #3 and #4 set the sizes of the MWPCs and requirement # 1 set their wire spacing. Requirement #2 is met by the FPP's fast, small-angle rejection system described later in this section. As was explained in section 2.2, this system was necessary as approximately 95% of the events undergo only small-angle multiple Coulomb scattering and are not useful for measuring polarizations. This also means that the graphite analyzer must be thin enough so that the multiple Coulomb scattering angles are smaller than those angles which are not rejected. The graphite analyzer is composed of slabs of many sizes from 0.5 cm to 10 cm that can be exchanged and stacked on top of each other so that up to 30.5 cm of graphite are available, allowing the FPP to operate over the full range of possible Bates proton energies. We used thicknesses of 5 to 10 cm. The FPP support structure has three different settings for supporting the large chamber directly above the graphite so that the separation between the two top chambers can be as large as possible for better scattering angle determination.

3.6.1 FPP MWPCs

MWPCs are similar to VDCs. The main difference is that no drift time information is recorded, just the presence of a hit, making the position resolution for individual chambers less accurate. The FPP MWPCs, also, do not have ground wires between the anode wires like the OHIPS VDCX does. There are, however, ground wires at the ends of the wire planes so that the fields at the plane edges are relatively uniform. The chambers' gas mixture was 50% argon and 50% isobutane bubbled through refrigerated isopropyl alcohol.

Outflow occurred through silicon oil to prevent backflow and to allow the flow rate to be monitored.

The anode wires are 20 μm gold-plated tungsten wire soldered and epoxied under tension to copper artwork on G-10 fiberglass frames. The artwork carries the signals to tabs on the exterior of the chamber. Each chamber has both x and y planes, which were positioned normal to the spectrometer's central momentum ray. Between and on both sides of the wire planes are planes of stretched 1/4 mil aluminized-mylar. We operated the MWPCs at 4.7-4.8 kV. As dictated by the thicknesses of the G-10 frames, the x and y planes are 1/2" apart in the small chambers and 1" apart in the large frames. Table 3.5 lists dimensions and parameters of the FPP MWPCs.

Chamber	1	2	3	4
Width (cm)	38.0	38.0	93.0	93.0
Length (cm)	74.0	74.0	148.0	148.0
Wire Spacing (in)	1/12	1/12	1/6	1/6
Number of X Wires	336	336	336	336
Number of Y Wires	176	176	208	208
X Distance to X1 (cm)	0	14.6	42.2	87.1
Y Distance to X1 (cm)	-1.3	13.3	39.7	84.5

Table 3.5. *FPP MWPC Parameters. X1 is 73.98 cm above the OHIPS VDCX origin and 22.3 cm below the bottom face of the graphite analyzer. Chamber 3 has 2 other possible settings.*

3.6.2 FPP Electronics

3.6.2.1 MWPC Readout System

The FPP MWPCs were read out much like the MEPS VDCX. Instead of DCOS, however, it used Proportional Chamber Operating System (PCOS) III. Shielded twisted-pair (black) ribbon cables took the signals to LeCroy 2735PC a/d cards. The card thresholds could be set via computer in a range of 1-7.5 volts. We typically had the threshold at about 5 volts but had to set many higher to avoid "hot" or "ringing" wires, a frequent problem that we were often battling. The cards were plugged into custom-made artwork boards that could handle 16 cards each. These boards were attached to racks, which were attached to the FPP support structure. The rack bottoms contained three cooling fans each. Ribbon cables took the discriminated signals from the cards to the PCOS crates outside of the shielding hut. With so many cables and racks things were quite crowded in the shielding hut. The cables often became loose or the connections did not line up properly resulting in "dead" wires, another problem we were frequently fighting.

The signals next went into LeCroy 2731A 32-channel delay latch modules (DCLs). There were six CAMAC crates containing all these DCLs, each controlled by a LeCroy 2738 PCOS III system controller in the rightmost slot. Planes X1, X2, Y1, and Y2 each had their own crate, whereas planes X3 and X4 shared a crate, as did Y3 and Y4. The DCLs had variable delays between 300 and 600 ns that were set via software. Ours was set at 339 ns. This gives the coincidence electronics enough time to generate a gate defining the time interval over which valid wire chamber signals may be recorded. When the coincidence electronics sends the controller this gate, called "E1", the controller sends this information on to the DCLs which "latch" any signals that fall within

the E1 gate and set their LAM (Look-At-Me). It is important to note that by adjusting the time of the E1 gate you can effectively adjust the wire-cell size of the MWPCs since a drift time that is too long (or too short if you mess up!) will not fall within the gate. Our E1 width was 75 ns.

Subsequently, the controller reads the information in modules whose LAMs are set and repackages the data. It takes the controller 100 ns to look for LAMs and 100 ns per module to read out the data. The controller has a look-up memory which allows logical addresses to be assigned within a crate. This is particularly important when more than one plane is in a crate. The six controllers are daisy-chained together to a LeCroy 4299 databus interface for data readout. Figure 3.14 schematically shows the PCOS system.

3.6.2.2 Small-Angle Rejection System

The FPP's MWPC readout electronics were equipped with a small-angle rejection system to quickly reject the approximately 95 percent of events with scattering angles too small to be useful. Figure 3.15 gives the electronic diagram for this system, which is described in detail in Lourie *et al.* ^[42] Each PCOS system crate controller outputs one 16-bit data word for each hit in its plane(s). Bits 1-9 contained the wire and slot numbers while bit 11 distinguished between planes 3 and 4. The wire number information went to two LeCroy 2378 Arithmetic Logic Units (ALUs). These units can calculate sums and differences of two data words. The ALUs were strobed by a four-fold coincidence of the Data Ready signals from each of the three PCOS crates and bit 11 from crate X3/X4, which meant that the hit is in plane 4. (The setup for Y was identical.) One of the ALUs calculated (*plane 2 wire#* - *plane 1 wire#*) while the other calculated (*plane 4 wire#* - (*plane 1 wire#*)/2), giving scattering

[42] R.W. Lourie *et al.*, Nuc. Inst. Meth. A306, 83 (1991).

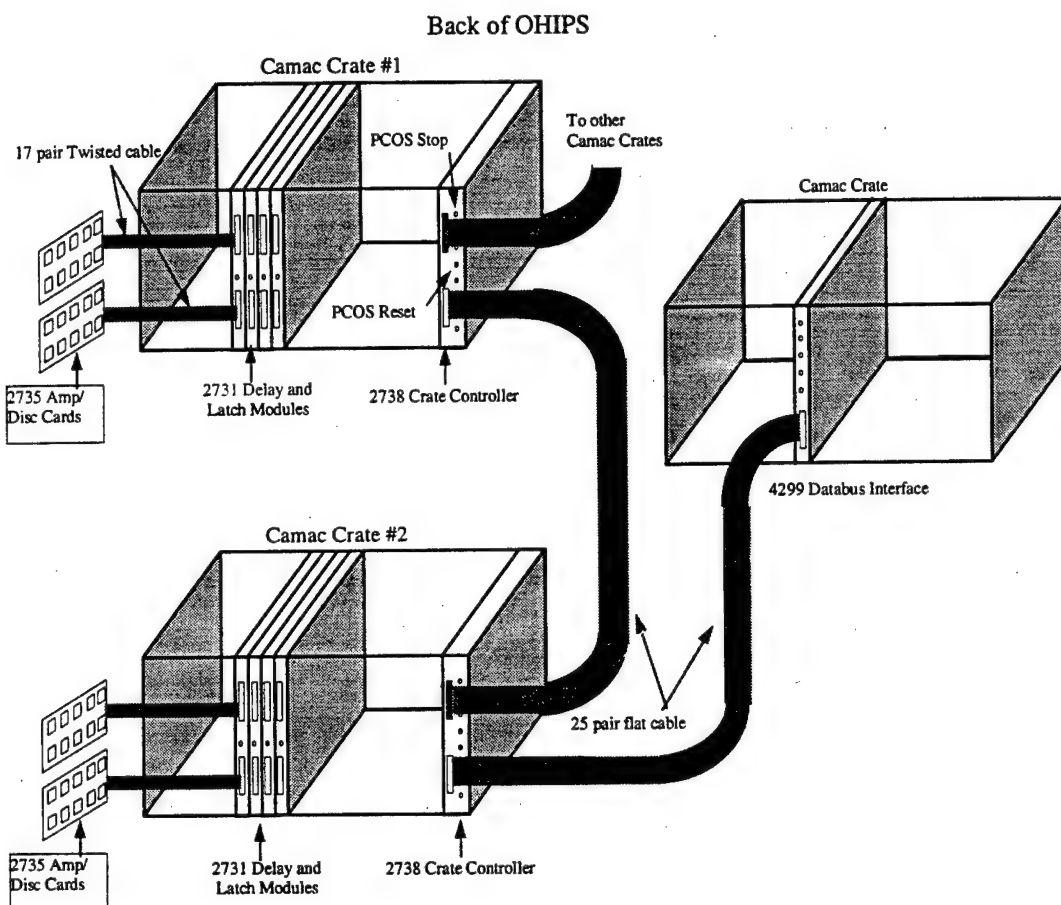


Figure 3.14 *PCOS III system.*

angle information before and after the graphite. (The factor of 2 was due to the fact that the wires in the lower planes are twice as dense as the wires in the upper planes). These differences were fed into a LeCroy 2372 Memory Lookup Unit (MLU) and combined to form the address of a single bit in the MLU. The MLU was preprogrammed so that bits corresponding to good scattering angles were set. The output bit was AND'd with the strobe to handle the problem of performing logic with ECL levels rather than NIM pulses. Finally, a coincidence (FPASS) checked to see if either X or Y passed the small-angle

June 7, 1994

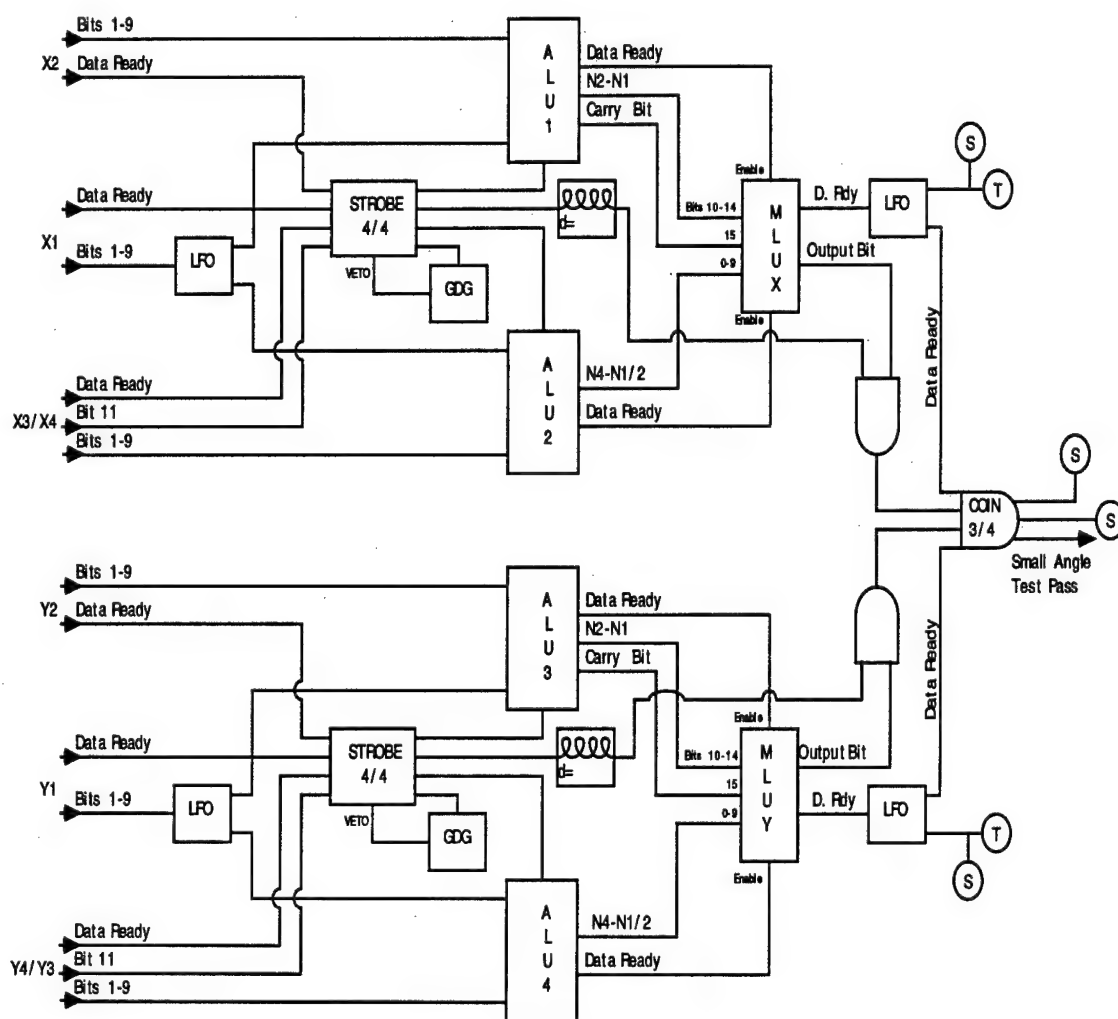


Figure 3.15 *FPP small-angle rejection system.*

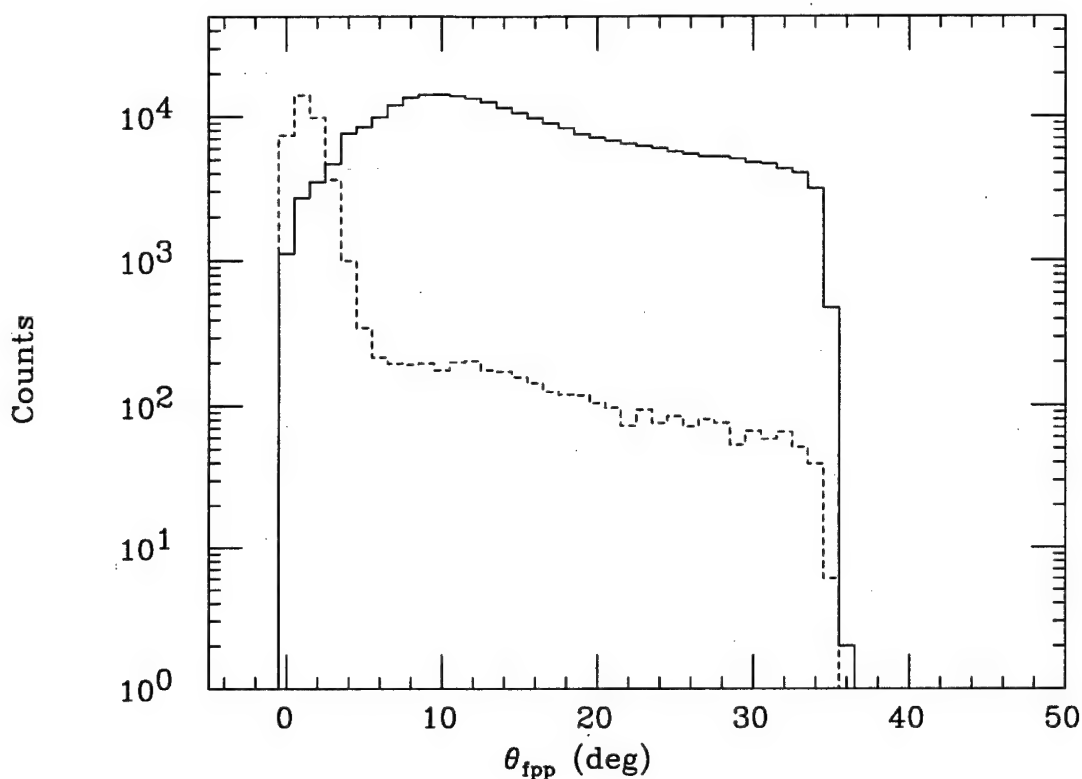


Figure 3.16 FPP angular distribution with (solid line) and without (dashed line) the small-angle rejection system.

3.6.2.3 Multi-hit Rejection System

In addition to small-angle events, the FPP electronics were also able to reject events which had more than two hits in any single plane (which occurred about three-fifths of the time). It used a LeCroy 4532 ECL Majority Logic Unit (MALU). This module works by summing the inputs (in this case Data Ready signals from the various planes) and seeing if they pass a user-set threshold. The MALU was gated using a delayed strobe so that the MALU would not sum its inputs until after the first two hits had occurred. Since planes 3 and 4 were in the same PCOS crate a plane bit was used to distinguish between plane 3 and plane 4 events, which were read out first. This also meant that plane 3's

multi-hit events could not be tested for rejection.

3.7 Coincidence Trigger Electronics

Figure 3.17 gives a functional overview of this experiment's electronics. Level 1 used scintillators to generate pilots, as was discussed earlier. Level 2 included the coincidence logic between MEPS and OHIPS and the generation of "prescales" (events randomly accepted for taping regardless of subsequent trigger logic for diagnostic purposes). In either case, data from one (or both) of the spectrometers were "latched" pending level 3. Level 3 used the results of the FPP rejection-systems described in the previous section to generate either CAMAC enables and the event data CAMAC read signal (PROMPT8), or reset the spectrometers' readout electronics. Inhibits were used to make sure that data was not interfered with by other data during decision and readout times.

3.7.1 Level 2 Trigger Electronics

Level 2 started with the pilots OPI and MPI generated in level 1. (Figure 3.18 shows this level's electronics logic.) These were AND'ed to form the coincidence pilot (CPI). OPI was much narrower (around 10 ns) and delayed so it determined the timing. In order to study non-coincidence electron and proton events, and also coincidence events that did not have good FPP events, prescale events were made by AND'ing the pilots with pulses from signal generators. These signal generators were in the counting bay so that they could be easily controlled by the experimenters. OPI, MPI, and CPI were used to create the prescales OPS, MPS, and CPS, respectively; with the timing set by the pilots. CPI was also AND'ed with helicity plus and minus signals from the control room, with the results scaled so that any helicity-dependence could be noted.

Each of the latches OLATCH and MLATCH were formed in NIM MALUs.

Overview of FPP Electronics

March 14, 1996

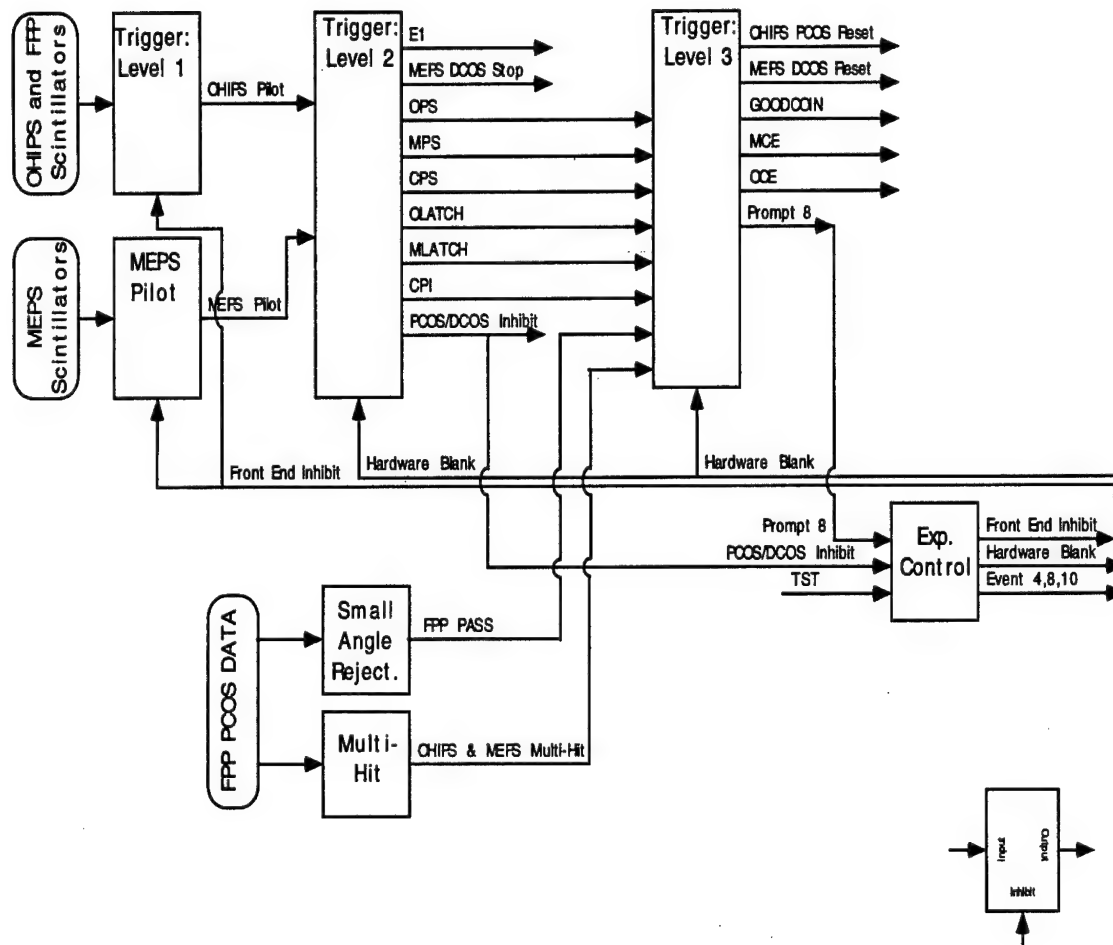


Figure 3.17 Overview of experiment electronics.

requiring a level of 3. The MALU inputs for OLATCH were OPS, CPI, and two copies of OPI (making it required); which set the timing and reduced the output signal's jitter. MLATCH was made the same way. A copy of MLATCH was sent back to MEPS and used as a DCOS stop. A copy of OLATCH was

FPP Trigger: Level 2

June 7, 1994

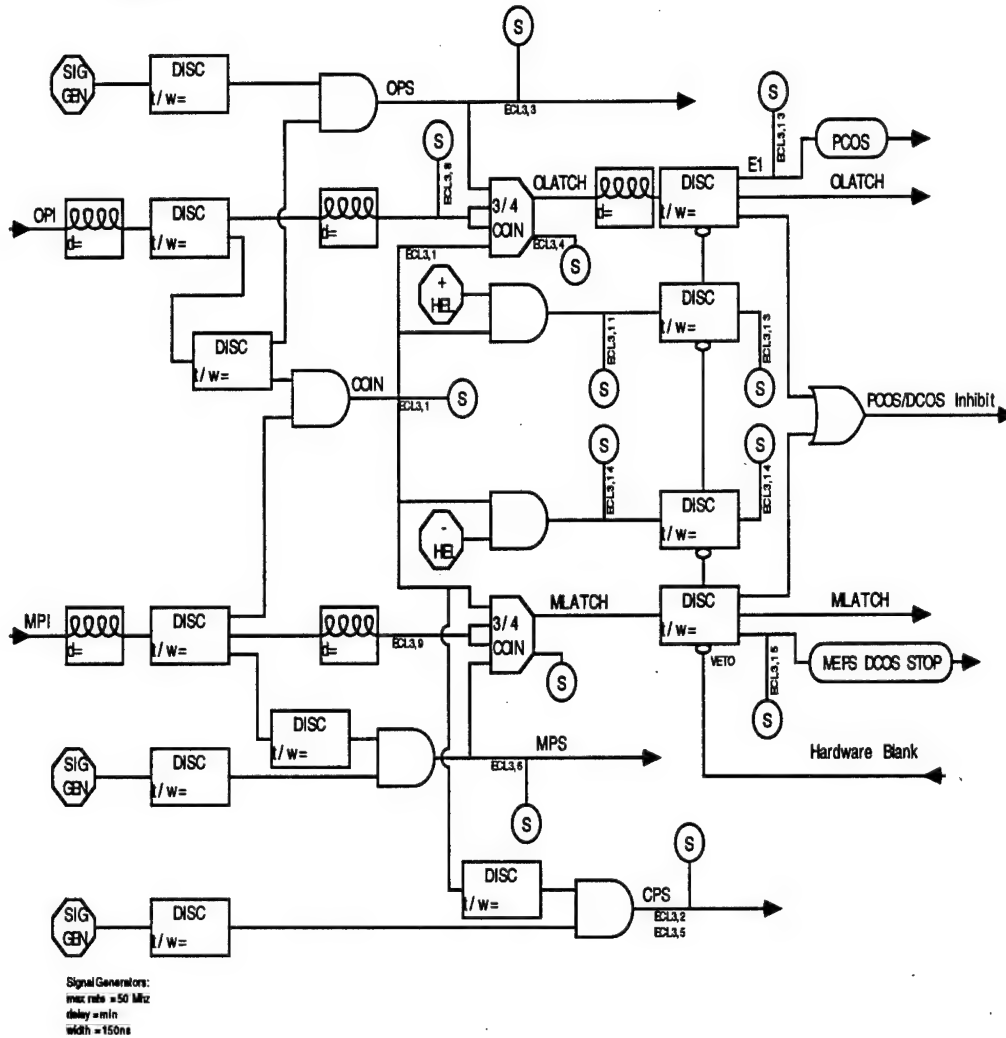


Figure 3.18 Level 2 trigger electronics.

used as the E1 signal for latching the FPP wire signals in PCOS. All 8 signals from this level needed in the next (3 pilots, 3 prescales, and 2 latches) were delayed over 650 ns using a PDM and ribbon cable. This time was needed for the PCOS readout and small-angle rejection test to be completed.

FPP Trigger: Level 3

June 17, 1994

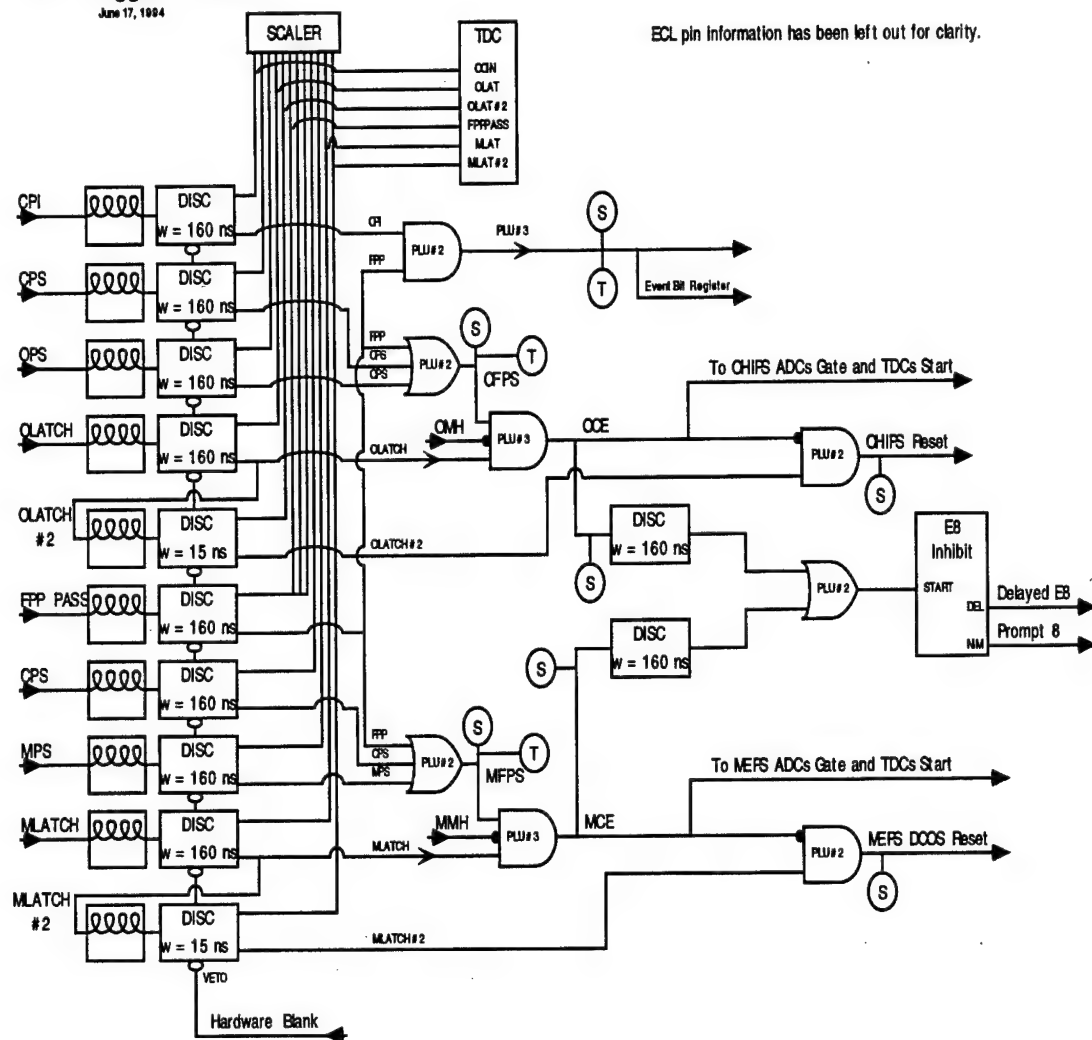


Figure 3.19 Level 3 trigger electronics.

3.7.2 Level 3 Trigger Electronics

Figure 3.19 shows the third and last level of the trigger electronics. Level 3 used the 8 signals from level 2 and FPPASS. CPI and FPPASS were AND'ed to

make COIN_EVENT. This was wired to a Schlumberger bit register, as were OPS, MPS, and CPS so that the event type could be identified by which bits were set. FPASS, CPS, and OPS were OR'ed in a PLU, the result of which was then AND'ed in a subsequent PLU with OLATCH and a logically inverted multi-hit signal. (In other words, if the event was a multihit and passed the MALU, this AND will fail.) This made up the OHIPS CAMAC Enable (OCE) signal, which was used to start the OHIPS TDCs and ADC gates. The AND of a logically-inverted OCE and a delayed OLATCH was used to reset PCOS system crate controllers and databus interfaces. A similar procedure made MCE and the MEPS resets. OCE and MCE were OR'ed to create PROMPT8, which meant that an event occurred that we wished to read out. Upstairs, an AND of MPI and MCE started a TDC that was stopped by an AND of OPI and OCE. This gave us a coincidence time-of-flight (CTOF) spectrum.

3.7.3 Experimental Control Electronics

When the electronics was deciding whether it was interested in an event or not, or when it was reading out an event, new data needed to be inhibited so as not to corrupt the old data. Likewise, once the electronics had decided that an event was of interest, it needed a way to trigger the data acquisition system (described in section 3.8) to readout the data. These jobs were handled by our experimental control electronics, which are shown in figure 3.20

There were two types of trigger inhibits: Hardware Blank and Frontend Inhibit. The Hardware Blank signal was used to inhibit new data at the second and third levels of the trigger while a decision was made whether or not to read out an event. (The first level was not inhibited due to the fact that since charge is counted for a whole beam burst the number of pilot scalers also needs to be counted for a whole beam burst.) Several such decisions could be made within a burst but once a decision was made to record an event the Hardware

FPP - Experimental Control

March 14, 1996

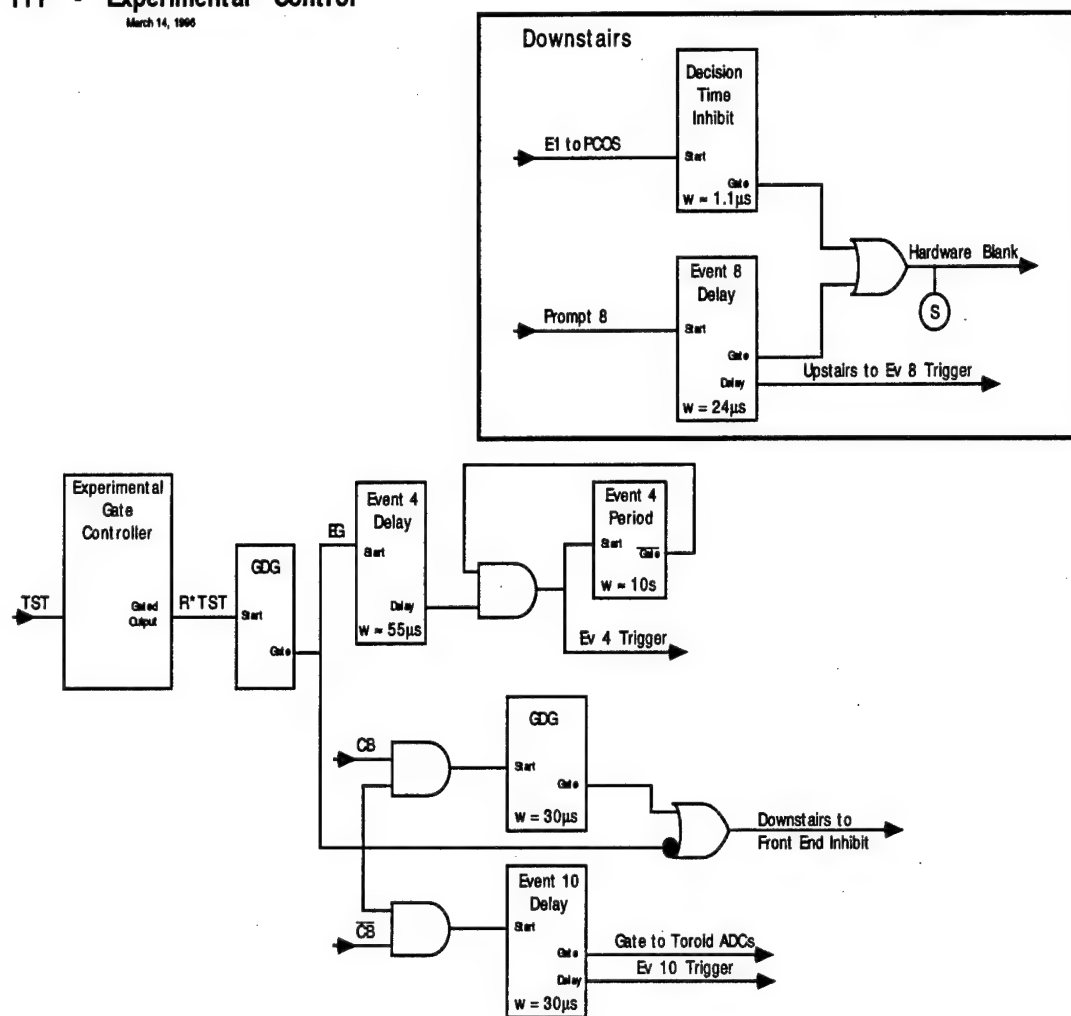


Figure 3.20 Experimental control electronics.

Blank would inhibit the rest of the beam burst. The Frontend Inhibit, on the other hand, inhibited all three trigger levels while an event was being read out to prevent new data from corrupting the event. (It was also used for other reasons, which are mentioned later.) This typically inhibited the next two bursts entirely

while an event was being recorded.

The Hardware Blank signal inhibited data by inhibiting the discriminator outputs. It was created from an OR between E1 and PROMPT8 signals that had been widened in gate-delay generators (GDGs). The E1 gate-delay generated signal was $1.1\mu\text{s}$ long while PROMPT8's was $24\mu\text{s}$. The two signals overlapped. The E1 signal came first and inhibited new data while the PCOS system was read out, the small-angle rejection decision was made, and resets were made (if necessary). If the coincidence electronics decided to record the event, PROMPT8 triggered event 8 (which did this) and inhibited the rest of the beam burst.

Upstairs, a Timeslot Trigger signal was received from the control room when beam was delivered. This signal was input to the experimental gate controller. The experimental gate controller received start and stop signals from an output register that was controlled by the data acquisition computer. It could also be disabled (i.e., stopped due to a problem) with signals from the output register or from trip signals from OHIPS or MEPS wire chambers. The gun controller started and stopped the BT3 current integrator.

The GUN signal was used with some gate-delay generators (GDGs) to create the event 4 (scaler-read) trigger every 12 seconds. Trigger signals were input to the trigger module described in section 3.8. The trigger module also put out a computer busy signal. The GUN was AND'ed with the computer busy signal. An OR of this signal with the not-GUN created the Frontend Inhibit signal, which was sent downstairs to inhibit the OHIPS and MEPS Scintillator and OHIPS VDCX discriminators, thereby inhibiting data collection when the computer was busy or when there was no GUN (i.e., run and timeslot trigger). The computer-busy generated by an event 8 (physics event) was about 4 msec long and thus inhibited the two beam bursts subsequent to the event burst.

The GUN was also AND'ed with the computer-not-busy signal. This signal started two GDGs: one whose output gated the BT1 and BT2 ADCs and a second which was stopped by a PROMPT8 signal. The output signal of this second GDG was AND'ed with a pulse generator. The output of this AND was scaled and served as a monitor of when events occurred within beam bursts. In addition, the signal which started these two GDGs also triggered event 10, which read out the beam position monitors and toroid ADCs, as well as the helicity bit and a timeslot scaler received from the control room.

3.8 Data Acquisition System

Of the many crates of electronics that this experiment used, only five contained modules such as scalers, TDCs, ADCs, and databus interfaces that we wished to read data from or write to. (Of course, additional crates were reached through the databus interfaces.) These five CAMAC crates had CAMAC crate controllers in their right-most slots that were daisy-chained together using Branch Highway Cable. This cable was terminated at one end and connected to a Microprogrammable Branch Driver (MBD) at the other. The MBD was connected with flat cable to a card in a Digital Equipment Corp. MicroVax II computer, on which our data acquisition software ran. The data acquisition system used in this experiment was called 'Q'. It was developed at LAMPF (Los Alamos Meson Physics Facility) to be used with VAX's VMS (Virtual Memory System) computer operating system and ran as a subprocess in DCL (Digital Command Language). The two main tasks of Q are the data acquisition and the analysis.

Q acquired data on an event-by-event basis. Events were triggered either via software or by input signals to the trigger module located in the first CAMAC crate. Events 0-3 and 13 were software triggered. (Event 13 was actually triggered by the cryotarget PC via a Kinetic Systems 3340

communication interface.) Lower numbered triggers take precedence over higher numbered ones. Event 0 was triggered at the end of a run to disable the run controller. Event 1 disabled the controller if a run was suspended. Event 2 was triggered to reset the electronics and enable the run controller if a run was resumed. Event 3 was triggered at the start of a run to initialize the electronics and enable the run controller. Event 13 dealt with reading out target parameters. Event 8 was the physics data readout event. Event 4 read out scalers. Event 6 read the beam profile monitor while event 10 read the beam current monitor and related information.

When the Q subprocess is initialized, a special QAL (Q Acquisition Language) code is loaded into the MBD. The QAL code defines the various CAMAC modules and tells, for each particular event-type, which ones are to be written to, read, cleared, LAM enabled, etc. The read-out order defines the structure of the raw data arrays. The raw data structure for the main data events (8) and the scalers (4) are given in tables 3.6 and 3.7 respectively. By bit testing the Schlumberger register, readout for single arm and prescale events was sped up by setting the appropriate data words to zero in software rather than actually reading the irrelevant modules.

Data acquired by Q was immediately written to disk. A batch process continuously searched for completed runs and copied them (using Q) to tape. Other computers were used for offline analysis. Online analysis was performed when the computer was not busy acquiring data. User-supplied FORTRAN codes analyzed the raw data into useful information such as particle kinematics and measured polarizations. Q allowed the user to create histograms of the data (raw or calculated), subject the data to various tests, and set-up and change parameter values. Figure 3.21 is a flowchart of the experiment's analysis code. Details of the analysis are described in the next chapter. One of my main activities in preparation for this experiment was writing and modifying the

many different codes used by this system and combining the many pieces into one complete package.

Array Element	Word Description
1	Event Bit Register
2	Trigger TDC Flag
3	OPI TDC
4	MPI TDC
5	OPS TDC
6	MPS TDC
7	CPI TDC
8	FPASS TDC
9	OLATCH TDC
10	OR (CPS,FPASS,OPS) TDC
11	MLATCH TDC
12	OR (CPS,FPASS,MPS) TDC
13	OLATCH #2 TDC
14	OCE TDC
15	MCE TDC
16	MLATCH #2 TDC
17	CPS TDC
18	Hardware Blank TDC
19-20	Beam Position Monitor
21	OHIPS Delay Line TDC Flag
22-31	OHIPS Scintillator ADCs
32-41	OHIPS Scintillator TDCs
42-46	OHIPS Meantimer TDCs
47	OHIPS F2MT OR TDC
48-63	OHIPS Delay Line TDCs
64	MEPS Scintillator ADC Flag
65-70	MEPS Scintillator ADCs
71-80	MEPS Aerogel ADCs
81	MEPS Aerogel Sum ADC
82-87	MEPS Scintillator TDCs
88	MEPS S0 OR TDC
89-90	MEPS Scintillator MT TDCs
91	CTOF TDC
92-100	MEPS Aerogel TDCs
101	MEPS Aerogel Sum TDC
102	MEPS DCOS Flag
103-127	25 MEPS DCOS Words
128	FPP TDC Flag
129-130	FPP MLU Data Ready TDCs
131-136	FPP Crate Data Ready TDCs
137	FPP PCOS Flag
138-183	46 PCOS Wire Chamber Words

Table 3.6 Event 8 Data Array Structure.

Array Element	Word Description
1-6	MEPS Scintillators
7	MEPS S0 OR
8	MEPS S3 MT
9	MEPS S4 MT
10	BT3
11	MPI upstairs
12	blank
13-22	MEPS Aerogels
23	MEPS Aerogel Sum
24	Gun
25	Gun and Computer Not Busy
26	Gun and Computer Not Busy and H^-
27	Gun and Computer Not Busy and H^+
28	Gun
29	Gun and Computer Not Busy
30-39	OHIPS Scintillators
40-44	OHIPS MTs
45	OHIPS FS2 OR
46	CPI
47	CPS
48	OPS
49	OLATCH
50	CPS
51	MPS
52	MLATCH
53	MPI
54	MEPS DCOS Stop
55	PCOS E1 Start
56	CPI and H^+
57	CPI and H^-
58	CPI and H^+ (1/burst)
59	CPI and H^- (1/burst)

Table 3.7. Event 4 Scaler Data Array Structure (cont. on next page). Header word is not included.

Array Element	Word Description
60	Hardware Blank
61	OPI
62	CPI (1/burst)
63	FPASS
64	FPASS
65	CPS (1/burst)
66	OPS (1/burst)
67	FPASS
68	CPS (1/burst)
69	MPS (1/burst)
70	OLATCH (1/burst)
71	MLATCH (1/burst)
72	OLATCH #2 (1/burst)
73	OCE (1/burst)
74	MCE (1/burst)
75	MLATCH #2 (1/burst)
76	OR (CPS,FPASS,OPS) (1/burst)
77	OR (CPS,FPASS,MPS) (1/burst)
78-93	OHIPS Delay Lines
94	PROMPT8
95	COIN_EVENT
96-101	PCOS Crate Data Readies
102-103	PCOS MLU Data Readies
104	PCOS Small-angle Pass
105	PCOS Multi-hit Pass
106	OHIPS Reset
107	MEPS Reset
108	OPI τ
109	OPI 2τ
110	MPI τ
111	MPI 2τ
112	CPI τ
113	CPI 2τ

Table 3.7. Event 4 Scaler Data Array Structure (cont.).

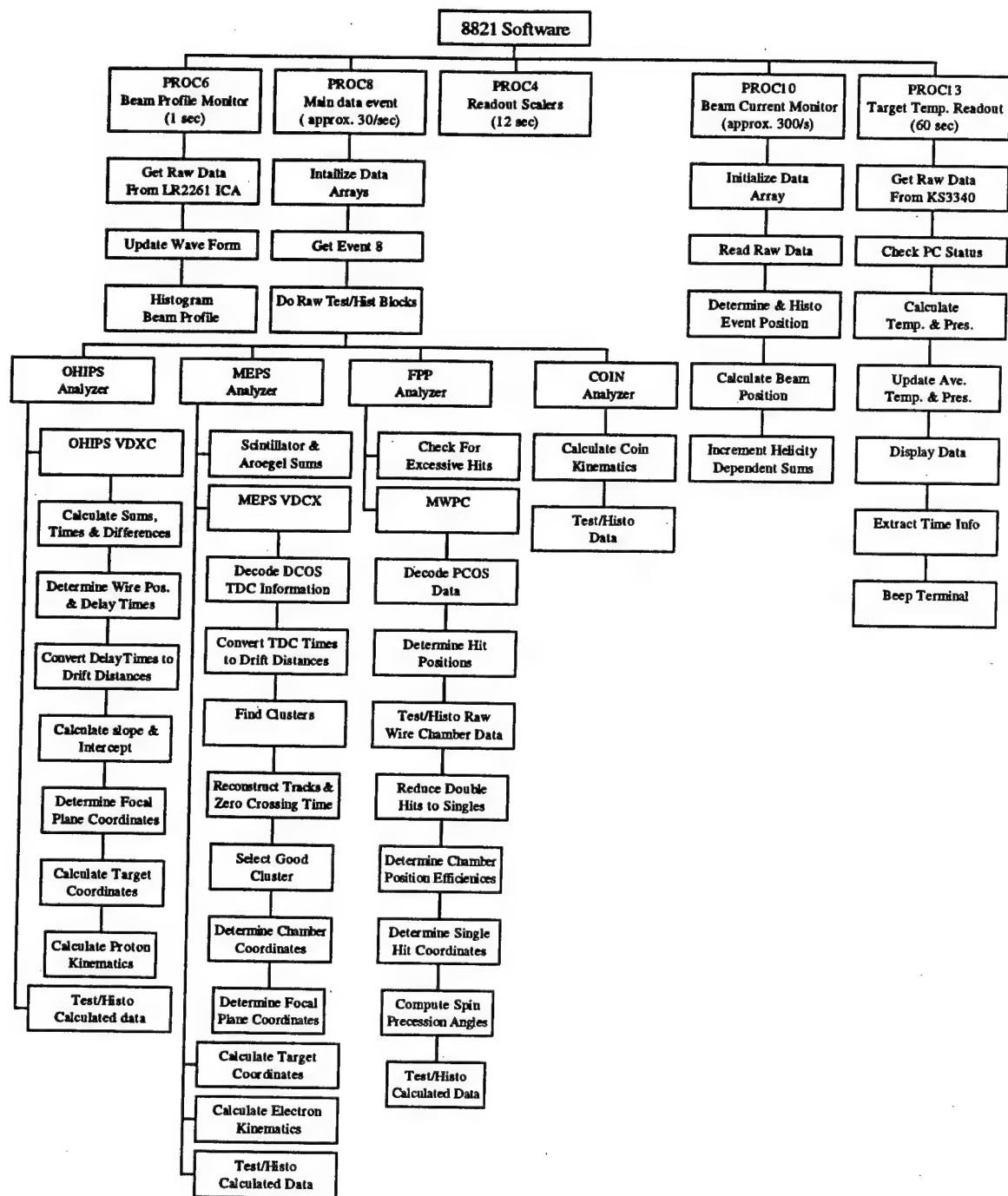


Figure 3.21 Computer analysis flowchart.

Chapter 4

Data Analysis

At the end of the previous chapter an overview and flowchart of the experiment's data analysis code was given. In this chapter the specifics of the analysis will be discussed. First comes the extraction of information from the VDCXs of OHIPS and MEPS, as well as coincidence information. Next the FPP MWPC analysis is described, showing how the second-scattering angles are determined. Last is the extraction of polarizations at the focal plane and their subsequent determination at the target, taking spectrometer magnet effects into account.

4.1 OHIPS VDCX Analysis

As was described in section 3.5.2, the OHIPS VDCX delay line signals from both the right and left sides can be added and subtracted to give the drift times and wire numbers for an event. These quantities, modified by offsets, are shown in figure 4.1. They are formed for each of the eight delay lines (4 per plane). While converting from wire numbers to wire positions is quite straightforward, converting from drift times to drift distances is a little more involved.

4.1.1 Determination of Drift Distances

As shown in figure 3.8 and described in section 3.4.2, a released electron in a VDC travels at a constant velocity until very near the anode wire. Since a spectrum of drift times, i.e., the number of events per time bin, is proportional

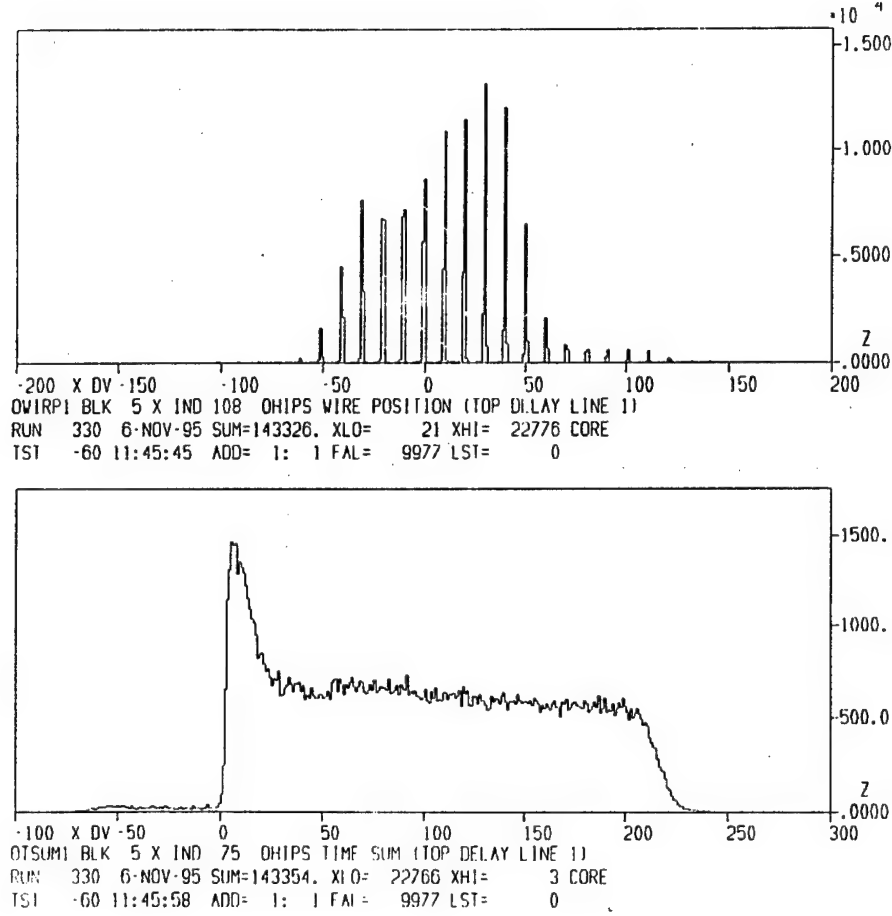


Figure 4.1 Raw VDCX spectra. The top figure shows wire numbers while the second figure shows the drift times for the same delay line.

to the the drift velocity (v_d):

$$\frac{dN}{dt} = \frac{dN}{ds} \frac{ds}{dt} = \frac{dN}{ds} v_d ; \quad (4.1)$$

figure 4.1b has a long flat region formed by those events whose tracks passed through the constant parallel field line section of the cell. The spectrum's peak results from those tracks passing through the radial field line area of the cell

near the anode wire. Though the actual drift velocity does not increase much until very near the wire, v_d is effectively increased due to the shortest field line now being a radial one perpendicular to the inclined track instead of a parallel one near the edge of the cell. ^[43] The gradual fall-off at the end of the spectrum's flat region reflects the rising probability at large drift times that another wire on the same delay line could have a shorter drift time and thus be the "hit" for that delay line instead.

Our method for converting the drift times to drift distances for the different regions is based on the work of Bates-ELSSY spectrometer users who spent much time investigating this problem. ^[44] Starting with a set of high-quality drift time histograms, each histogram is divided into four regions: before the peak, after the peak but before the flat region, the flat region, and the fall-off tail. By positioning channel 1 on the first significant channel of the peak's leading edge, the drift distance for a particular drift time histogram channel is:

$$\text{drift dist.} = \text{drift dist. of prev. channel} + v_r \cdot \text{drift time} / \text{histogram channel} \quad , \quad (4.2)$$

where v_r is the effective drift velocity for the region the channel is in. In the flat region and the fall-off tail, the effective drift velocity is just the terminal drift velocity (v_t) of ≈ 5 cm/ μ s. For the peak's trailing edge, however, the effective drift velocity is:

$$v_r = v_t \cdot \frac{\# \text{ of counts in channel}}{\text{avg. } \# \text{ of counts/channel in flat region}} \quad , \quad (4.3)$$

while for the leading edge it is taken to be:

$$v_r = v_t \cdot \frac{\# \text{ of counts in peak channel}}{\text{avg. } \# \text{ of counts/channel in flat region}} \quad . \quad (4.4)$$

^[43] W. Bertozzi *et al.*, Nuc. Inst. Meth. 141, 457 (1977).

^[44] D. Jordan *et al.*, Bates Internal Report #92-03.

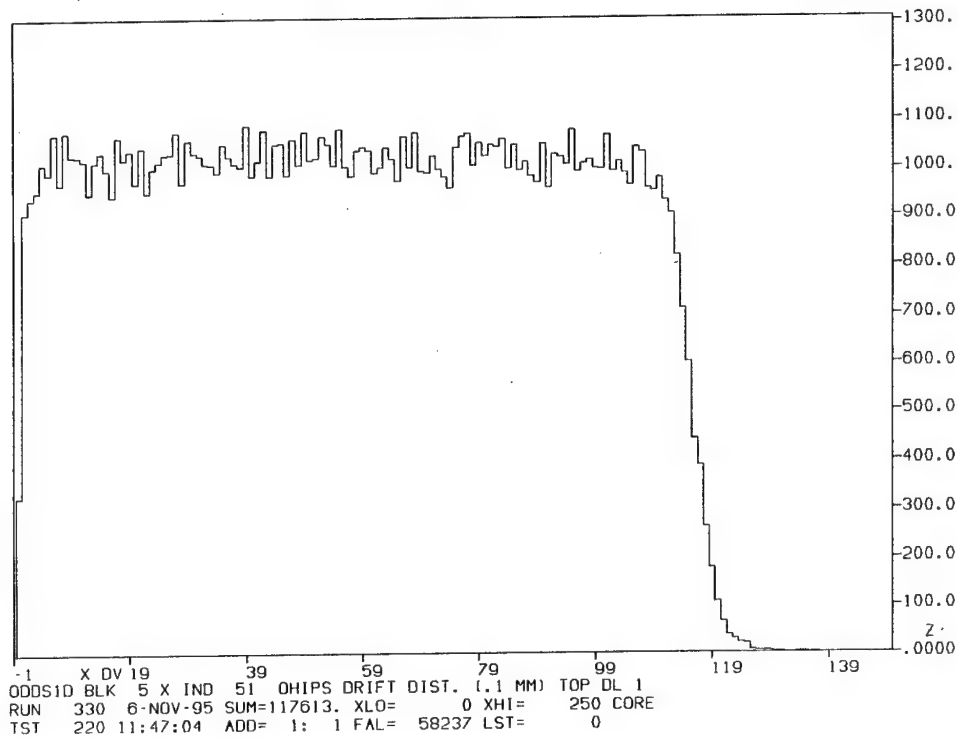


Figure 4.2 VDCX drift distance spectra calculated from the previous figure's drift time spectra.

These drift distance values for particular drift time histogram channels are then made into lookup tables, a separate table for each VDC plane. Once the lookup table has been made, any similar drift time histogram can be converted to drift distances. Figure 4.2 shows a drift distance histogram made in this manner.

4.1.2 Determination of Wire Plane Coordinates

The next step in the VDCX analysis is to convert the drift times and wire positions to a track trajectory. An important part of doing this is determining which drift times (which are all positive) act as positive coordinates and which act as negative coordinates in relation to the wire plane. The track's slope and

wire-plane intercept were determined using a least squares linear fit. Due to the large error possible in very small drift distances, ^[45] those wire-hits with drift distances less than 1 mm were not used. All tracks with four consecutive hits or three hits with no more than one wire gap (which could have been because of the previously mentioned very small drift distance) were fit and those with $\chi^2 < 0.2$ were accepted.

The analysis code was also designed to handle an OHIPS VDCX problem that has been noticed by previous experiments: ^[45] namely, a delay time difference jitter that is on the order of one delay line spacing, causing the wire position to be shifted by four wires. For events which the algorithms could not handle or returned high χ^2 values, analysis attempts were made by shifting each wire position by four in either direction and examining if a better fit could be obtained. Given the adjacent wire and χ^2 requirements, it is extremely unlikely that this could produce false data. This increased the number of analyzed OHIPS events by about 2%.

For an event to be considered good its track inclination had to be within an acceptable range determined by the physical orientation of the chambers. This test was performed by putting a box cut on the 2-D histogram of slope 1 vs. slope 2.

4.1.3 Determination of Focal Plane Coordinates

Once the intercept and slope are known for each of the two planes, the focal plane coordinates can be calculated. Figure 4.3a shows the orientation of the two planes to each other. First, the top and bottom planes are projected

^[45] S.D. Penn, Ph.D. dissertation, MIT(1993), unpublished.

onto a single intermediate one via the relationships:

$$\begin{aligned} u'_T &= -u_T - \frac{m_T D_{ch}}{2} \\ u'_B &= u_B + \frac{m_B D_{ch}}{2} \end{aligned} \quad (4.5)$$

where m_i are the track slopes (run over rise), u_i are the wire-plane intercepts, and D_{ch} is the separation between the two planes. The next step is to rotate the projected coordinates to a system with x' towards the direction of increasing momentum:

$$\begin{pmatrix} x' \\ y_f \end{pmatrix} = \begin{pmatrix} \cos \gamma & \sin \gamma \\ -\sin \gamma & \cos \gamma \end{pmatrix} \begin{pmatrix} u'_B \\ u'_T \end{pmatrix} \quad \gamma = 45^\circ \quad (4.6)$$

as shown in figure 4.3b. Finally, a rotation about y_f to account for the VDCX's tilt with respect to the central momentum ray is needed:

$$\begin{pmatrix} x_f \\ z_f \end{pmatrix} = \begin{pmatrix} \cos \Omega & -\sin \Omega \\ \sin \Omega & \cos \Omega \end{pmatrix} \begin{pmatrix} x' \\ z' \end{pmatrix} \quad \Omega = 45.3^\circ \quad (4.7)$$

as shown in figure 4.3c. Since $z' = 0$, $x_f = x' \cdot \cos \Omega$. In the past θ_f and ϕ_f were also calculated using the slopes and rotation angles but with the addition of the FPP it is more accurate to perform a linear fit using the VDCX position coordinates and those of the two FPP chambers in front of the carbon block.

4.1.4 Determination of Target Coordinates

Determining target coordinates from the focal plane coordinates requires an understanding of the spectrometer's optics. These are approximated by a second order TRANSPORT matrix that relates the target coordinates $x_t = (x_t, y_t, \theta_t, \phi_t, \delta)$ to the focal plane coordinates $x_f = (x_f, y_f, \theta_f, \phi_f, \delta)$ by the equation

$$x_f^i = \sum_j M_{ij} x_t^j + \sum_{j,k} T_{ijk} x_t^j x_t^k \quad (4.8)$$

where M_{ij} (T_{ijk}) is the first(second) order TRANSPORT matrix. Figure 4.4 shows the two coordinate systems as they relate to each other. Both coordinate

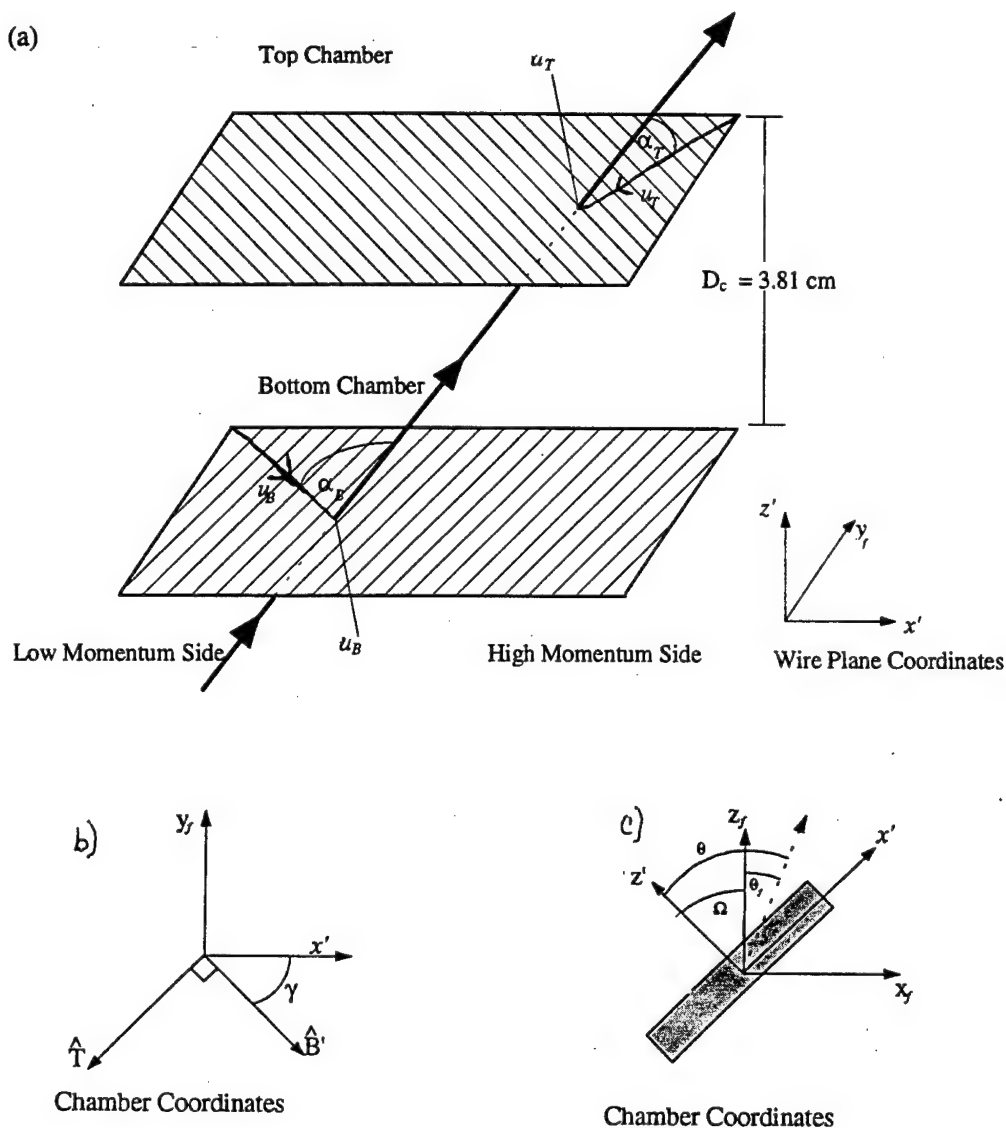


Figure 4.3 OHIPS VDCX coordinate systems. 4.3a shows the orientation of the two planes with respect to each other. 4.3b and 4.3c show the rotations about z' and y_f , respectively.

systems have \hat{z} along the spectrometer's central momentum ray and \hat{x} in the dispersion direction in the magnet's bend plane. θ and ϕ are the angles relative to \hat{z} in the x and y direction, respectively. δ is the relative momentum from

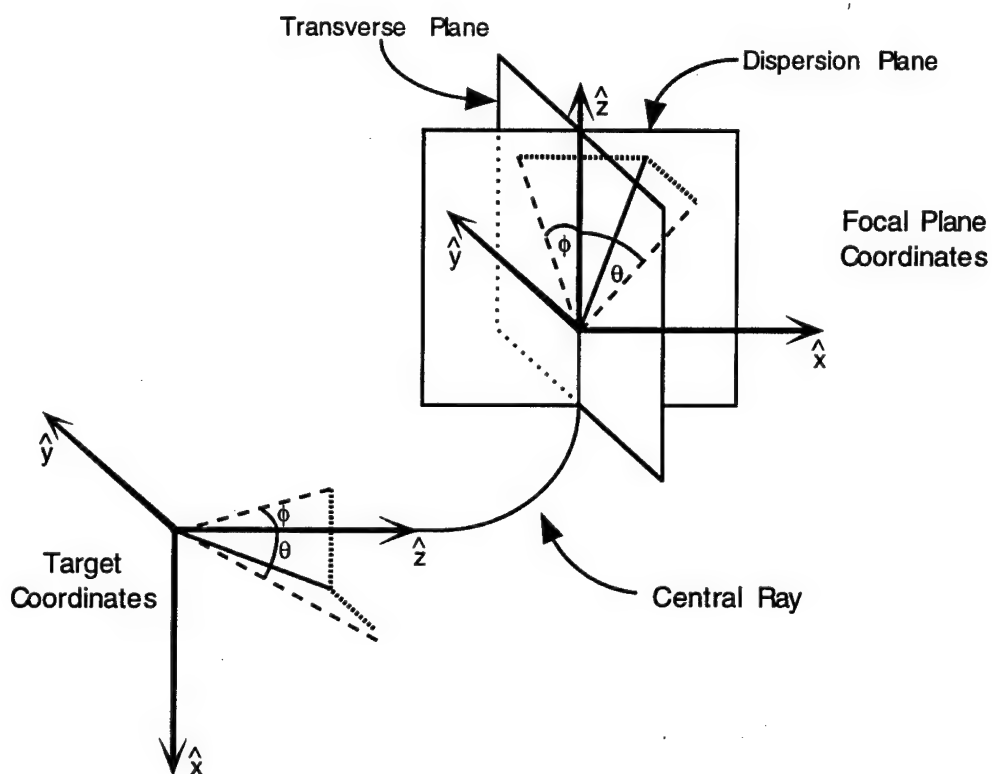


Figure 4.4 *The target and spectrometer focal plane coordinate systems.*

which the proton's momentum can be determined:

$$P = P_c + \delta P_c \quad , \quad (4.9)$$

where P_c is the central momentum in the spectrometer (as set by the dipole's magnetic field).

Keeping the dominant terms in equation 4.8, the OHIPS focal plane

coordinates are

$$\begin{aligned}
 x_f &= \langle x|x \rangle x_t + \langle x|\delta \rangle \delta \\
 y_f &= y_{off} + \langle y|y \rangle y_t + \langle y|y\theta \rangle y_t \theta_t + \langle y|y\delta \rangle y_t \delta + \langle y|\phi\delta \rangle \phi_t \delta + \langle y|\phi\theta \rangle \phi_t \theta_t \\
 \theta_f &= \theta_{off} + \langle \theta|\theta \rangle \theta_t + \langle \theta|\theta\delta \rangle \theta_t \delta + \langle \theta|\delta \rangle \delta + \langle \theta|\delta^2 \rangle \delta^2 \\
 \phi_f &= \phi_{off} + \langle \phi|y \rangle y_t + \langle \phi|\phi \rangle \phi_t + \langle \phi|\phi\theta \rangle \phi_t \theta_t \\
 &\quad + \langle \phi|\phi\delta \rangle \phi_t \delta + \langle \phi|y\delta \rangle y_t \delta + \langle \phi|y\theta \rangle y_t \theta_t .
 \end{aligned} \tag{4.10}$$

Since there are four equations but five unknowns; x_t , the out-of-plane coordinate at the target, is not determined but assumed to be zero since the beam spot is small. This makes

$$x_f = \langle x|\delta \rangle \delta , \tag{4.11}$$

which we used in our actual target coordinate determination equations:

$$\begin{aligned}
 \delta &= \frac{x_f}{\langle x|\delta \rangle} \\
 \theta_t &= \frac{\theta_f - \theta_{off} - \langle \theta|\delta \rangle \delta - \langle \theta|\delta^2 \rangle \delta^2}{\langle \theta|\theta \rangle + \langle \theta|\theta\delta \rangle \delta} \\
 a &= \langle y|y \rangle + \langle y|y\delta \rangle \delta + \langle y|\theta y \rangle \theta_t \\
 b &= \langle y|\phi\theta \rangle \theta_t + \langle y|\phi\delta \rangle \delta \\
 c &= \langle \phi|y \rangle + \langle \phi|\theta y \rangle \theta_t + \langle \phi|y\delta \rangle \delta \\
 d &= \langle \phi|\phi \rangle + \langle \phi|\phi\delta \rangle \delta + \langle \phi|\phi\theta \rangle \theta_t \\
 y_t &= \frac{d(y_f - y_{off}) - b(\phi_f - \phi_{off})}{ad - cb} \\
 \phi_t &= \frac{a(\phi_f - \phi_{off}) - c(y_f - y_{off})}{ad - cb} .
 \end{aligned} \tag{4.12}$$

The values for these matrix elements and offsets (listed in table 4.1) were determined by putting a sieve slit collimator of known hole spacings in the front

of OHIPS and quasielastically scattering electrons through the spectrometer. Then by measuring at the focal plane the positions of the peaks associated with the different sieve slit holes, the matrix elements in the above equations could be adjusted so as to best reproduce the physical placement of the sieve slit holes. Those matrix elements involving δ were determined by taking elastic data at different magnet settings, thus moving the location of the elastic peak at the focal plane. (This is known as a focal plane scan.) Matrix elements involving y_t were determined from runs using a thin, tilted BeO target so that the y position was both known and variable.

Element	Value	Element	Value
$\langle x \delta\rangle$	4.149	$\langle\theta \delta\rangle$	10.16
y_{off}	0	$\langle\theta \delta^2\rangle$	-0.0656
$\langle y y\rangle$	-1.345	ϕ_{off}	0
$\langle y y\delta\rangle$	-0.0533	$\langle\phi y\rangle$	-0.380
$\langle y y\theta\rangle$	0.00195	$\langle\phi y\theta\rangle$	0.000538
$\langle y \theta\phi\rangle$	-0.000523	$\langle\phi y\delta\rangle$	-0.011768
$\langle y \phi\delta\rangle$	0.00879	$\langle\phi \phi\rangle$	-0.756
θ_{off}	9.527407	$\langle\phi \theta\phi\rangle$	-0.00149
$\langle\theta \theta\rangle$	-0.4963	$\langle\phi \phi\delta\rangle$	0.04257
$\langle\theta \theta\delta\rangle$	-0.01529		

Table 4.1. OHIPS 1st and 2nd order optics matrix elements for a 1.60 m first drift space, VH focus.

4.2 MEPS VDCX Analysis

4.2.1 Determination of Analyzable Events

Though the MEPS VDCX chamber is quite similar to OHIPS's, the read-out system is very different. Rather than a delay-line system, MEPS uses the DCOS system in which drift times for all the fired wires are read. Since one is not limited to four wires as in OHIPS, multiple particle trajectories can be read. This makes the analysis more complicated but also less corruptible.

In our analysis, MEPS events with more than 24 wire hits were not accepted. Since DCOS was operated in common stop mode, all of the drift times needed to be "mirrored" by subtracting them from a maximum time and then using an offset to make the drift time spectra start at zero, as shown in OHIPS figure 4.1a. The drift times were converted to drift distances in the same manner as in OHIPS.

The analysis code next looked for active wire clusters. Starting with the lowest active wire number, the first cluster went until a second hole (no active wire) was found or the highest allowed active wire number was reached. The next cluster then started at the next active wire and so on. A maximum of eight clusters were accepted, though the cluster distribution (shown in the top of figure 4.5) peaked strongly at one. The maximum number of wires in a cluster that the code would accept was sixteen. The peak number was four or five (as is seen in the bottom of figure 4.5). To be analyzable, a cluster had to have at least three hits.

For each analyzable cluster, the wire with the minimum drift time was chosen to be the pivot wire. Two situations were tried to determine the cluster's track (slope and intercept): 1) the drift times of active wires below the pivot

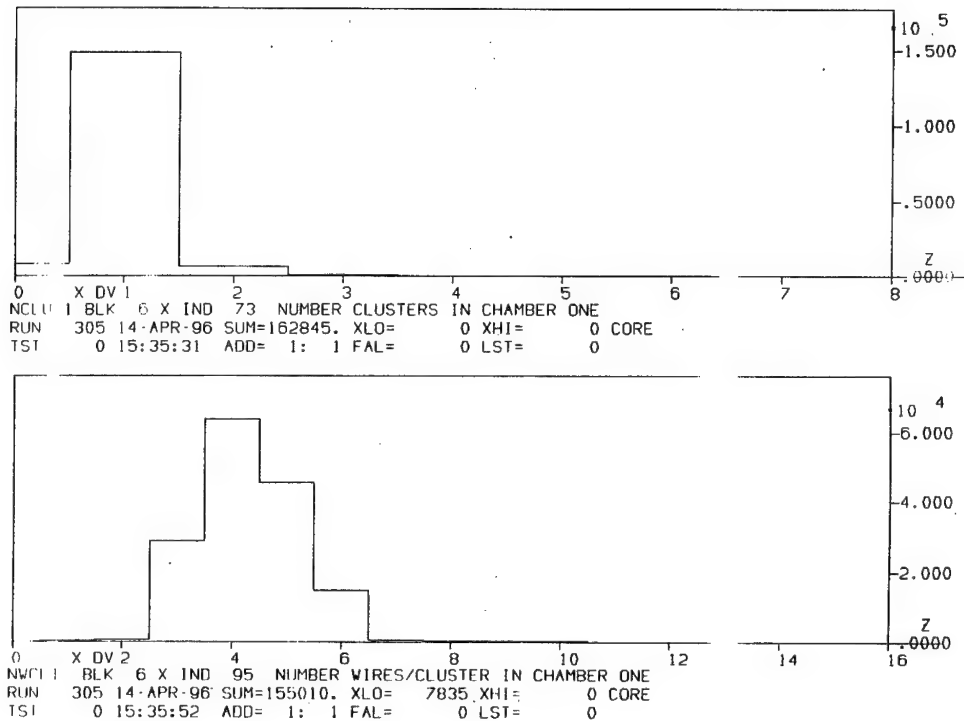


Figure 4.5 MEPS cluster spectra. The top figure shows the number of clusters per event and is strongly peaked at one. The second figure shows the number of wires per cluster.

were taken to be negative or 2) the drift times of active wires below the pivot and the pivot were taken to be negative. (The negative drift times had to be in the low wires for the required positive slopes.) The situation that gave the lowest χ^2 in a linear fit was then used.

All the analyzed clusters were then compared to see which had the smallest zero crossing time, i.e., which required the smallest timing offset to make the drift distances above and below the pivot point line up. If both planes had

pivots, good clusters, and good slopes an event was analyzable.

4.2.2 Determination of Focal Plane Coordinates

Determination of the focal plane coordinates worked much as in OHIPS. Due to a different orientation of the wire planes with respect to each other, the equivalent of equation 4.6 for MEPS is:

$$\begin{pmatrix} x' \\ y_f \end{pmatrix} = \begin{pmatrix} \cos \gamma & \sin \gamma \\ \sin \gamma & -\cos \gamma \end{pmatrix} \begin{pmatrix} u_B \\ u_T' \end{pmatrix} \quad \gamma = 45^\circ \quad (4.13)$$

As shown in figure 4.3c, θ_f is related to the track slopes by

$$\begin{aligned} \theta_f &= \theta - \Omega \\ &= \tan^{-1} \left(\frac{dx'}{dz'} \right) - \Omega \\ &= \tan^{-1} \left[\cos \gamma \frac{du_B}{dz'} + \sin \gamma \frac{du_T'}{dz'} \right] - \Omega \\ &= \tan^{-1} \left[\frac{\cos \gamma}{m_B} + \frac{\sin \gamma}{m_T} \right] - \Omega \\ &= \tan^{-1} \left[\frac{m_T \cos \gamma + m_B \sin \gamma}{m_B m_T} \right] - \Omega \quad , \end{aligned} \quad (4.14)$$

while ϕ_f is given by

$$\begin{aligned} \phi_f &= \tan^{-1} \left(\frac{dy_f}{dz_f} \right) \\ &= \tan^{-1} \left[\frac{dy_f/dz'}{dz_f/dz'} \right] \\ &= \tan^{-1} \left[\frac{\frac{\sin \gamma}{m_B} - \frac{\cos \gamma}{m_T}}{\cos \Omega + \left(\frac{\cos \gamma}{m_B} + \frac{\sin \gamma}{m_T} \right) \sin \Omega} \right] \\ &= \tan^{-1} \left[\frac{m_T \sin \gamma - m_B \cos \gamma}{m_B m_T \cos \Omega + (m_T \cos \gamma + m_B \sin \gamma) \sin \Omega} \right] \quad . \end{aligned} \quad (4.15)$$

4.2.3 Determination of Target Coordinates

For MEPS we used reverse matrix elements as given by the inverse of eqn. 4.8:

$$x_t^i = \sum_j (M_{ij})^{-1} x_f^j + \sum_{j,k} (T_{ijk})^{-1} x_f^j x_f^k, \quad (4.16)$$

so that the target coordinates were determined by

$$x_t = 0$$

$$\delta_t = \langle \delta | x \rangle x_f + \langle \delta | x^2 \rangle x_f^2$$

$$\theta_t = \theta_{off} + \langle \theta | x \rangle x_f + \langle \theta | \theta \rangle \theta_f + \langle \theta | x^2 \rangle x_f^2 + \langle \theta | \theta x \rangle \theta_f x_f + \langle \theta | y^2 \rangle y_f^2 + \langle \theta | \theta^2 \rangle \theta_f^2$$

$$\begin{aligned} \phi_t = & \phi_{off} + \langle \phi | x \rangle x_f + \langle \phi | y \rangle y_f + \langle \phi | \phi \rangle \phi_f + \langle \phi | x^2 \rangle x_f^2 \\ & + \langle \phi | xy \rangle x_f y_f + \langle \phi | \theta \phi \rangle \theta_f \phi_f + \langle \phi | \theta y \rangle \theta_f y_f \end{aligned}$$

$$y_t = y_{off} + \langle y | x \rangle x_f + \langle y | \phi \rangle \phi_f + \langle y | y \rangle y_f + \langle y | \phi^2 \rangle \phi_f^2. \quad (4.17)$$

Table 4.2 gives the relevant MEPS reverse matrix elements.

4.3 Scattering Angles

MEPS and OHIPS both detect particles in the same plane. This plane is horizontal and at the height where the beam hits the target. From fig. 4.4 it should be clear that ϕ_t is in-plane while θ_t is out-of-plane. Therefore, the in- and out-of-plane proton scattering angles (denoted as horizontal and vertical, respectively) are defined as:

$$\begin{aligned} \theta_p^h &= \theta_{hall}^{OHIPS} - \phi_t^{OHIPS} \\ \theta_p^v &= \theta_t^{OHIPS} \end{aligned} \quad (4.18)$$

Element	Value	Element	Value
$\langle \delta x \rangle$	0.5521	$\langle \phi \phi \rangle$	-0.34877
$\langle \delta x^2 \rangle$	0.000777	$\langle \phi y \rangle$	-10.756
θ_{off}	-9.7003	$\langle \phi x^2 \rangle$	-0.0153835
$\langle \theta x \rangle$	0.26617	$\langle \phi xy \rangle$	0.19069
$\langle \theta \theta \rangle$	-0.38908	$\langle \phi \theta \phi \rangle$	-0.0021425
$\langle \theta x^2 \rangle$	-0.02387	$\langle \phi \theta y \rangle$	0.010918
$\langle \theta \theta x \rangle$	0.0019076	y_{off}	3.1830
$\langle \theta \theta^2 \rangle$	0.0003005	$\langle y x \rangle$	-0.24770
$\langle \theta y^2 \rangle$	0.091117	$\langle y \phi \rangle$	0.83792
ϕ_{off}	0	$\langle y y \rangle$	-6.3145
$\langle \phi x \rangle$	0.10358	$\langle y \phi^2 \rangle$	-0.0025595

Table 4.2. MEPS reverse matrix elements.

and the corresponding electron angles as:

$$\begin{aligned}\theta_e^h &= \theta_{hall}^{MEPS} + \phi_t^{MEPS} \\ \theta_e^v &= -\theta_t^{MEPS} .\end{aligned}\tag{4.19}$$

θ_{hall}^{OHIPS} and θ_{hall}^{MEPS} are the positive in-plane angles between the beam-dump pipe ($\theta = 0$) and the spectrometers. The electron's actual scattering angle is thus:

$$\theta_e = \cos^{-1}(\cos \theta_e^h \cos \theta_e^v) .\tag{4.20}$$

4.4 Coincidence Spectra

4.4.1 Time-of-Flight Spectra

Any coincidence experiment is going to have both true coincidences and accidentals. The rate of these accidentals is proportional to the individual spectrometer's singles rates and the coincidence resolving time ($\Delta^c t$):

$$R_A = \frac{R_e R_p \Delta^c t}{d.f.} , \quad (4.21)$$

where $d.f.$ is the accelerator's duty factor. Proof of the occurrence of true coincidence events is provided by the coincidence time-of-flight (CTOF) TDC spectra. The accidentals that get into this spectrum will have, in general, a flat time distribution while the time-correlated coincidence events will result in a narrow spike on top of the flat background. An example of this spectrum for this experiment is shown in figure 4.6. For experiments with appreciable background, one normally has to correct this spectrum for pathlength and velocity variations in order to improve the signal to noise ratio. Such was not the case for us, given our kinematics and simple hydrogen target.

4.4.2 Missing Energy Spectra

Two quantities that are useful for determining if the coincidence kinematics are properly understood are the missing energy and momentum. For elastic scattering from hydrogen, these should both be zero. The missing energy is equal to:

$$E_m = \omega - T_p = E - E' - T_p . \quad (4.22)$$

The missing momentum, also referred to as the recoil momentum, is given by:

$$\vec{p}_r = \vec{k} - \vec{k}' - \vec{p}' . \quad (4.23)$$

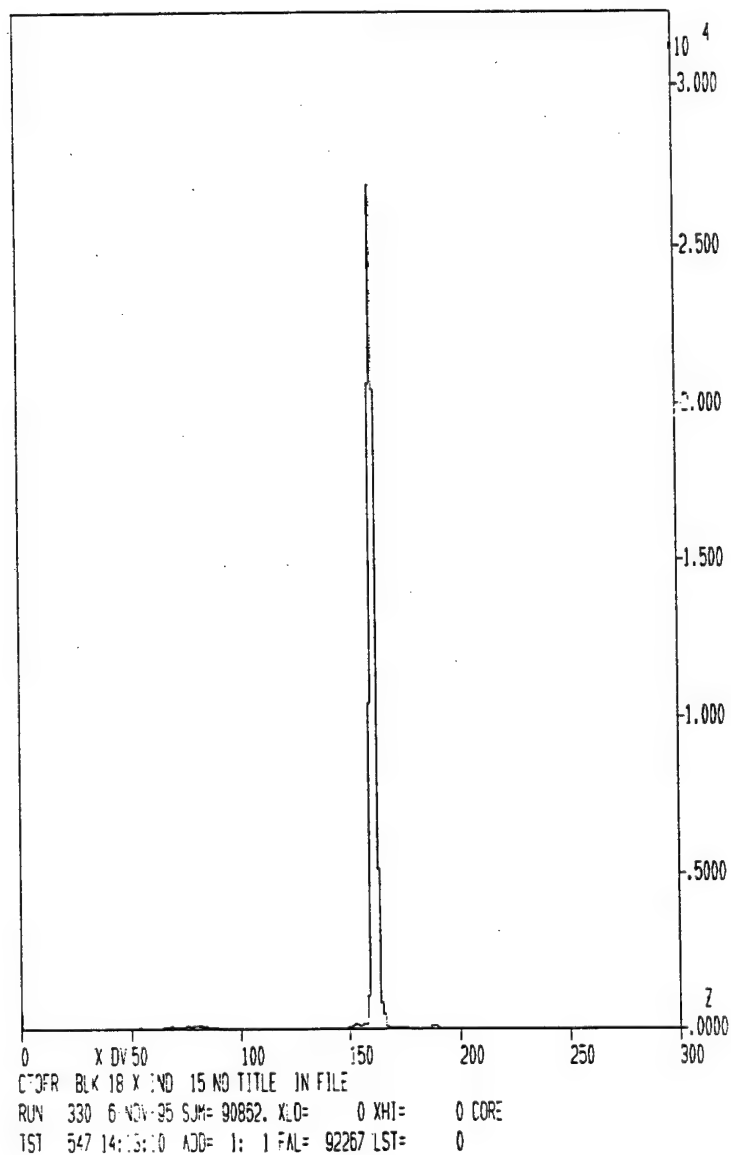


Figure 4.6 CTOF TDC spectrum with no corrections.

In order for these spectra to peak at zero, the input quantities have to reflect what happened at the scattering point inside the target. This means that corrections have to be made for energy losses in the target.

There are two basic types of electron energy losses in targets: radiation and

ionization losses. At our experiment's energies, radiation losses cause a larger average energy loss than ionization losses in hydrogen. However, the energy loss probability goes like $1/E_\gamma$ so that the most probable energy loss is zero. The most probable ionization losses, however, are nonzero so that:

$$E = E_o - \epsilon_{ion} \quad (4.24)$$

The most probable energy loss due to ionizing atomic electrons (Landau straggling) is given by: ^[46]

$$\epsilon_{ion} = \xi \left[\ln \frac{\xi}{\epsilon'} + 0.37 \right] \quad (4.25)$$

where

$$\xi = \frac{2\pi N_a e^4 t \rho Z}{m_e c^2 A} \quad (4.26)$$

where ρ is the material density and t is its thickness, and

$$\epsilon' \cong 2.718 \frac{(1 - \beta^2) I^2}{2m_e} \quad (4.27)$$

$I = Z \cdot 1.35 \times 10^{-5}$ MeV and is the average atomic ionization potential. Losses in the target walls were insignificant. Roughly speaking, the incoming and scattered electron both lost about 0.9 MeV from ionization losses.

The proton's energy losses were calculated using RASP ^[47] - a program based on nuclear data tables. ^[48] ^[49] The energy losses were dominated by those occurring in the hydrogen itself, rather than in the target walls. Total losses in the target were approximately 2 MeV.

[46] H. Überall, *Electron Scattering from Complex Nuclei*, Vol. B, Academic Press (1971).

[47] C.S. Whisnant, private communication.

[48] W. Barkas and M. Berger, *Tables of Energy Losses and Ranges of Heavy Charged Particles*, NASA-SP-3013 (1964).

[49] J. Janni, *At. Data and Nucl. Data Tables* **27**, nos. 4-5 (1982).

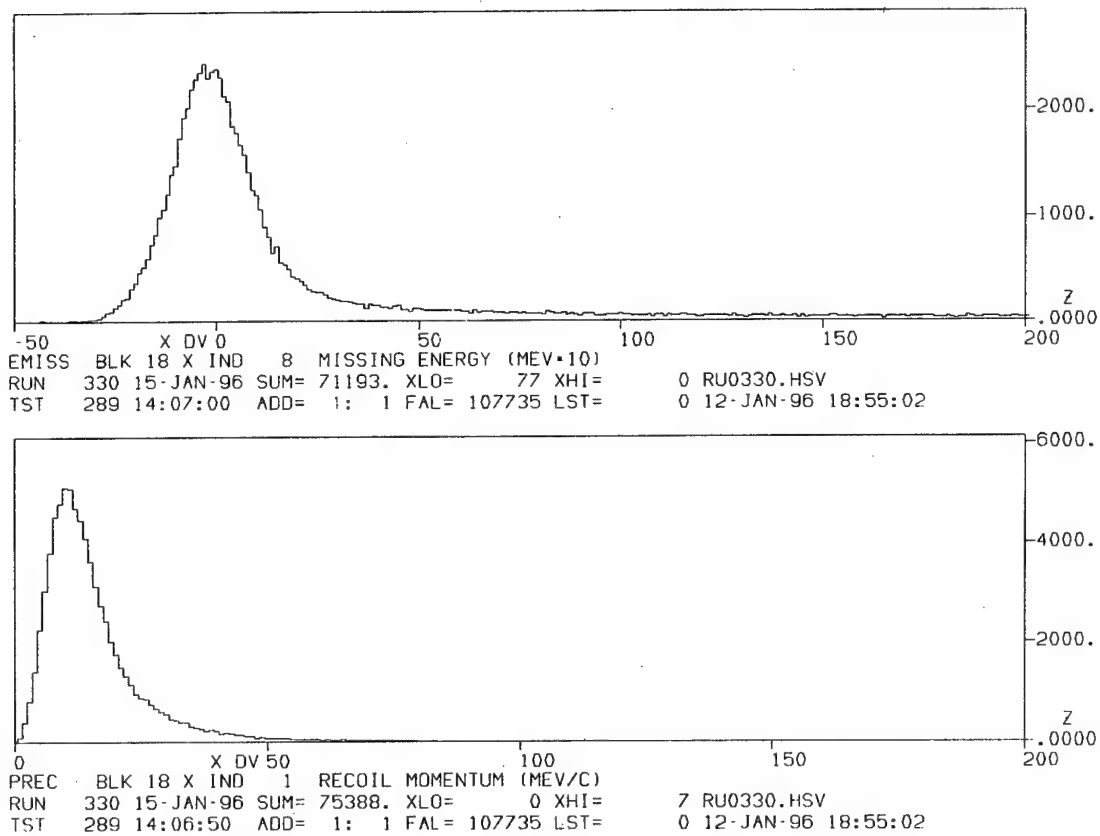


Figure 4.7 Missing energy (top) and momentum (bottom) spectra.

With the energy losses calculated, the true momenta seen by the spectrometers were known. Using the measured relative momentum δ , the actual central momentum of the spectrometers could then be determined using equation 4.9. Figure 4.7 shows a typical missing energy (top) and missing momentum (bottom) from our experiment. The missing energy is accounted for to within 1 MeV and the missing momenta peaks near zero, as expected. (The reason it does not peak at zero is that its yield integral, in addition to containing a peak at zero widened due to resolution, multiple scattering, etc.; contains a phase space term $p^2 dp$ that goes to zero as p goes to zero.) The tails in both spectra are due to radiative losses by the electron, both before and after the scattering.

4.5 FPP MWPC Analysis

Our largest analysis effort was devoted to polarization determination. The information from each of the four MWPCs had to be combined to determine the particle tracks before and after the carbon and then the scattering angles in the carbon. Whereas our MEPS and OHIPS analysis codes were based on the works of previous experimenters, our FPP analysis code was entirely our own creation. Its description makes up this section.

4.5.1 Determination of Carbon Scattering Angles

The first step in the analysis is to convert the raw PCOS data into wire numbers. The wire numbers were converted into wire positions with the origin defined as the middle of the chamber. Hit wires in the same plane that were adjacent were clusterized into a "single" hit. Unlike drift chambers, position resolution in MWPCs cannot be better than a wire spacing. The chambers were aligned, both internally and with respect to the VDCX, using software offsets. The determination and consequences of these offsets are described in appendix C.

In order for track reconstruction to be possible, there had to be one and only one hit in each plane. If one of the planes had two nonconsecutive hits and the other seven had single hits, analysis was performed using both cases, in the hope that cuts performed after the trajectories had been determined would eliminate one of them.

Figure 4.8 illustrates the track-reconstruction problem. From the observed chamber event positions (represented by \vec{A}_c , where c is the chamber number 1 through 4) and the known distances between the chambers one must determine the initial and final trajectories (\vec{S}_i and \vec{S}_f), and then the scattering angles

from those. The polarimeter's coordinate system is defined like OHIPS's to be right-handed with \hat{z} along the central ray normal to the chambers and \hat{x} in the direction of the increasing momentum dispersion. The direction $\vec{i}(\vec{f})$ of the proton's initial(final) trajectory is determined entirely from the positional information from the front(rear) chambers:

$$\begin{aligned}\vec{i} &\propto (\Delta x_{21}, \Delta y_{21}, \Delta z_{21}) \\ &= (\Delta x_{21}/\Delta z_{21}, \Delta y_{21}/\Delta z_{21}, 1) \\ &= (\tan \theta_i, \tan \phi_i, 1)\end{aligned}\tag{4.28}$$

and

$$\begin{aligned}\vec{f} &\propto (\Delta x_{43}, \Delta y_{43}, \Delta z_{43}) \\ &= (\tan \theta_f, \tan \phi_f, 1)\end{aligned}\tag{4.29}$$

The trajectories \vec{S}_i and \vec{S}_f are simply straight lines of slope \vec{i} and \vec{f} :

$$\begin{aligned}\vec{S}_i &= \vec{A}_1 + \vec{i}t_i \\ \vec{S}_f &= \vec{A}'_1 + \vec{f}t_f\end{aligned}\tag{4.30}$$

where \vec{A}_1 is \vec{S}_i 's intercept in plane 1 and \vec{A}'_1 is \vec{S}_f 's projected intercept in plane 1. To solve for \vec{A}'_1 note that

$$\begin{aligned}\vec{S}_f(z_4) \cdot \hat{z} &= \vec{A}'_1 \cdot \hat{z} + \vec{f} \cdot \hat{z}t_f(z_4) \\ \vec{S}_f(z_4) \cdot \hat{z} &= \vec{f} \cdot \hat{z}t_f(z_4) \\ z_4 &= t_f(z_4)\end{aligned}\tag{4.31}$$

so that

$$\begin{aligned}\vec{A}'_1 &= \vec{S}_f(z_4) - \vec{f}z_4 \\ &= \vec{A}_4 - \vec{f}z_4\end{aligned}\tag{4.32}$$

Once the basic trajectory vectors are set up the scattering angles can be determined. The polar scattering angle is simply the angle between the two

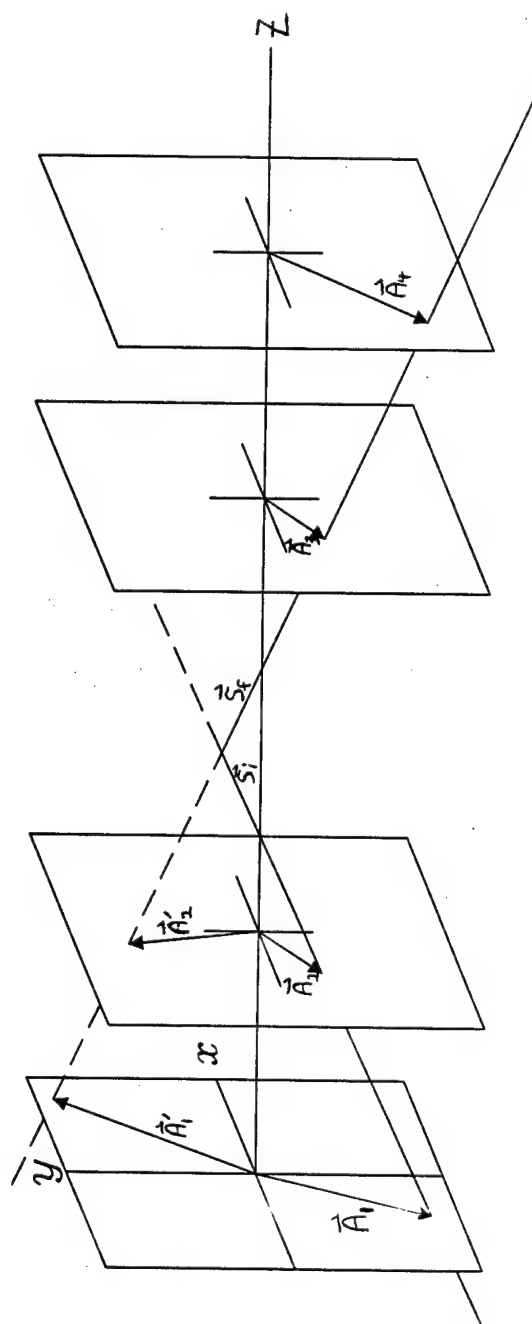


Figure 4.8 FPP MWPC trajectories. See text for description.

proton trajectories:

$$\theta = \cos^{-1} \left[\frac{\vec{i} \cdot \vec{f}}{|\vec{i}| |\vec{f}|} \right] \quad (4.33)$$

Determination of the azimuthal scattering angle ϕ is more complicated. First, let's define an event coordinate system in which \hat{z}' lies along the proton's momentum \vec{i} . Each event's \hat{z}' will be different, though the variation will be small since the vertical angle θ_{foc} is small ($\leq \sim 11^\circ$). These primed coordinates must transform to the spectrometer's when the vertical angle goes to zero (i.e., the proton goes straight up). By definition, ϕ equals 0 along the \hat{x}' axis. Expressing eq. 4.28 as $\vec{i} = (i_x, i_y, 1)$, the event unit vectors are:

$$\begin{aligned} \hat{z}' &= \vec{i}/|\vec{i}| = \frac{1}{\sqrt{\alpha}}(i_x, i_y, 1) \\ \hat{x}' &= \hat{y} \times \hat{z}' / |\hat{y} \times \hat{z}'| = \frac{1}{\sqrt{1 + i_x^2}}(1, 0, -i_x) \\ \hat{y}' &= \hat{z}' \times \hat{x}' \\ &= \frac{1}{\sqrt{\alpha(1 + i_x^2)}}(-i_x i_y, 1 + i_x^2, -i_y) \quad , \end{aligned} \quad (4.34)$$

where $\alpha = \vec{i} \cdot \vec{i}$. In these coordinates, the relationships

$$\begin{aligned} \vec{f} \cdot \hat{x}' &= |\vec{f}| \sin \theta \cos \phi \\ \vec{f} \cdot \hat{y}' &= |\vec{f}| \sin \theta \sin \phi \quad , \end{aligned} \quad (4.35)$$

lead to the azimuthal scattering angle

$$\begin{aligned} \tan \phi &= \frac{\vec{f} \cdot \hat{y}'}{\vec{f} \cdot \hat{x}'} \\ &= \frac{-f_x i_x i_y + f_y (1 + i_x^2) - i_y}{\sqrt{\alpha}(f_x - i_x)} \quad . \end{aligned} \quad (4.36)$$

(At this point some computational advice is in order. Remember that the arctan function will only return values between $-\frac{\pi}{2}$ and $\frac{\pi}{2}$ [quadrants I and IV]. The two other quadrants [II and III], however, have negative $\cos \phi$ [the previous equation's denominator] values instead of positive ones. Of these two quadrants, quadrant II has a positive $\sin \phi$ [the previous equation's numerator]

value and quadrant III has a negative one. Thus a correct four-quadrant ϕ value can be determined.)

In addition to the scattering angles we also used the before-and-after trajectories to determine the distance of closest approach of the two tracks. We define the vector $\vec{\Delta}$ as the difference between the two trajectories:

$$\vec{\Delta} = \vec{S}_i - \vec{S}_f = \Delta\vec{A} + \vec{i}t_i - \vec{f}t_f, \quad (4.37)$$

where $\Delta\vec{A} = \vec{A}_1 - \vec{A}'_1$. To get the vector coordinates at the intersection point (more correctly, the point of closest approach of the two trajectory vectors), $\vec{\Delta}$ needs to be minimized with respect to t_i and t_f . It is actually easier to minimize $\vec{\Delta}^2$:

$$\vec{\Delta}^2 = (\Delta\vec{A})^2 + \alpha t_i^2 + \beta t_f^2 - 2\gamma t_i t_f - 2\delta t_f + 2\epsilon t_i, \quad (4.38)$$

where

$$\begin{aligned} \alpha &= \vec{i} \cdot \vec{i} \\ \beta &= \vec{f} \cdot \vec{f} \\ \gamma &= \vec{i} \cdot \vec{f} \\ \delta &= -\vec{f} \cdot \Delta\vec{A} \\ \epsilon &= -\vec{i} \cdot \Delta\vec{A} \end{aligned} \quad (4.39)$$

Performing the minimization gives:

$$\begin{aligned} \frac{\delta}{\delta t_i} \Delta^2 &= 2\alpha t_i - 2\gamma t_f - 2\epsilon = 0 \\ \frac{\delta}{\delta t_f} \Delta^2 &= 2\beta t_f - 2\gamma t_i - 2\delta = 0 \end{aligned} \quad (4.40)$$

Solving these two equations simultaneously gives t_i and t_f at the moment of closest approach:

$$\begin{aligned} t_i^c &= \frac{\gamma\delta - \beta\epsilon}{\gamma^2 - \alpha\beta} \\ t_f^c &= \frac{\alpha\delta - \gamma\epsilon}{\gamma^2 - \alpha\beta} \end{aligned} \quad (4.41)$$

Using eq. 4.37 the distance of closest approach d_c between the two reconstructed trajectories can be determined:

$$\begin{aligned} dx &= \Delta A_x + i_x t_i^c - f_x t_f^c \\ dy &= \Delta A_y + i_y t_i^c - f_y t_f^c \\ dz &= t_i^c - t_f^c \\ d_c &= \sqrt{dx^2 + dy^2 + dz^2} \end{aligned} \quad (4.42)$$

Given the wire spacings (which define the chamber resolutions for MWPCs) and plane distances in table 3.5, the maximum error in the determined location of either the front or back track in the center of the carbon block is about 3 mm. Not taking dz into account, this implies that the distance of closest approach should generally be less than 6 mm. The top histogram in figure 4.9 shows our d_c spectra, which indeed falls in line with this estimate of the resolution.

It's also useful to check that the trajectory intersection occurred in the carbon slab. The coordinates of the closest approach point can be determined by averaging the two trajectory vectors at the point of closest approach:

$$\begin{aligned} \vec{c} &= \vec{\Sigma}/2 = (\vec{S}_i(t_i^c) - \vec{S}_f(t_f^c))/2 \\ &= (\vec{A}_1 + \vec{A}_1')/2 + (\vec{i}t_i^c + \vec{f}t_f^c)/2 \\ &= (\vec{A}_1 + \vec{A}_4 - \vec{f}z_4)/2 + (\vec{i}t_i^c + \vec{f}t_f^c)/2 \end{aligned} \quad (4.43)$$

Using this and the two trajectories, the pathlength the proton travels in the carbon before scattering can also be determined. The bottom histogram in figure 4.8 exhibits our pathlength spectra, which is basically the width of the carbon block (7 cm in this case).

Once the track (or possibly two tracks) had been reconstructed, it was tested to see if it had acceptable values for the x and y coordinates of the closest approach (\vec{c}), the initial trajectory angles (θ_i and ϕ_i), and the polar scattering angle (θ). These values were determined by studying events that only had one hit (or cluster) per plane. Hopefully, a two-track event had one track eliminated

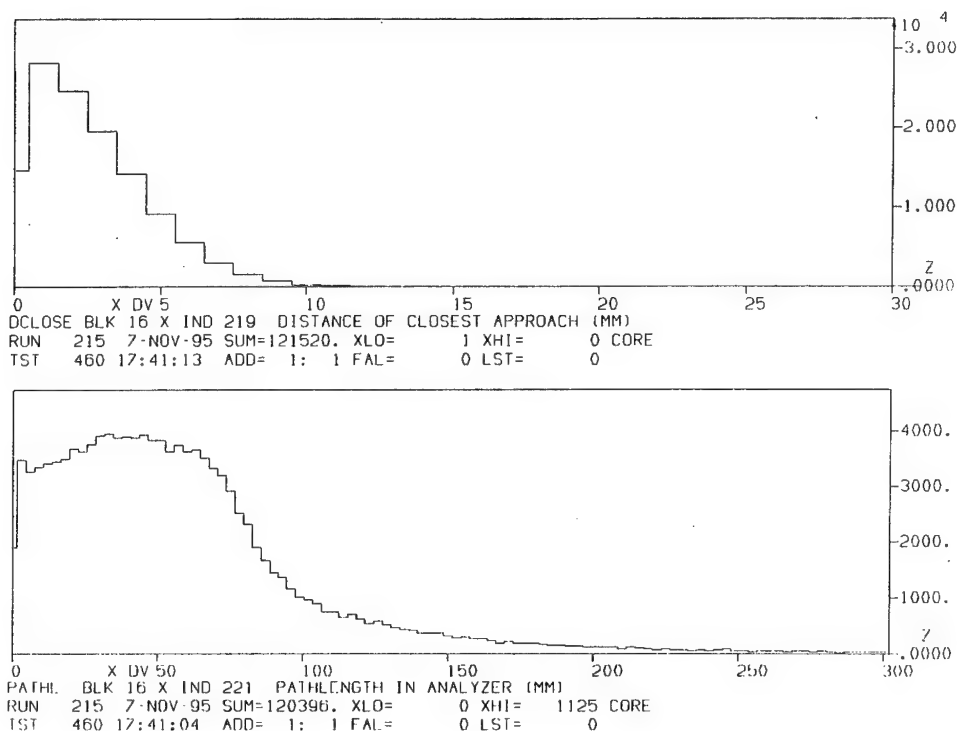


Figure 4.9 Spectra showing the FPP MWPC's ability to determine the scattering point from the measured trajectories. The top figure shows the closest distance between the two trajectories and the bottom figure shows the calculated distance of the scattering vertex from the front of the carbon block.

by these cuts so that it could be used. At this stage the remaining events were considered to be correctly reconstructed and analyzable. Using this method, we were able to analyze approximately 55% of the FPP events instead of the 45% that were single-cluster in each plane.

Since there is little information to be gleaned from small angle events and the analyzing powers ($A_c(\theta)$) above 20 degrees are not well known, we next limited our "good" events to those with scattering angles between 7 and 20

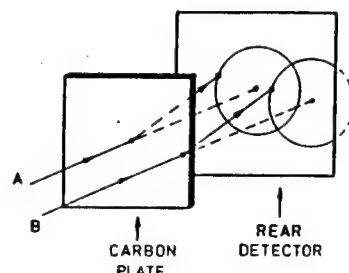


Figure 4.10 *Diagram of a cone-test.*

degrees. (See appendix C for a discussion of the lower value.) Furthermore, we also required events to pass a cone-test, shown in figure 4.10. ^[50] The difference between the location of an actual event in the rear detector (plane 4) and where it would have been had the proton not scattered serves as a radius of a cone's base for all possible ϕ scatterings from a given point with a given initial trajectory. If part of this cone lies off plane 4, such as for track B in the figure, this event must be thrown out to avoid making a biased sample of the scattering data. In our case, due to the size of our detectors, such events occurred rarely. An event passing this final test was considered to be a good event useful for extracting physics measurements.

4.5.2 Determination of Spin Precession Angle

Once it was decided that an event was good it was also necessary to determine its spin precession angle χ in the spectrometer. The proton's initial directional

^[50] J.A. Edgington, Nuc. Inst. Meth. **164**, 175 (1979).

vector at the entrance to the spectrometer is given by

$$\vec{P}_i = \frac{1}{\sqrt{1 + \tan^2 \theta_{tgt} + \tan^2 \phi_{tgt}}} (\tan \theta_{tgt}, \tan \phi_{tgt}, 1) \quad (4.44)$$

while its final directional vector at the focal plane is

$$\vec{P}_{fp} = \frac{1}{\sqrt{1 + \tan^2 \theta_{fp} + \tan^2 \phi_{fp}}} (\tan \theta_{fp}, \tan \phi_{fp}, 1) \quad (4.45)$$

We wish to know the final vector as expressed in the initial target coordinate system. This is simply a coordinate transformation:

$$\begin{pmatrix} P_f^x \\ P_f^y \\ P_f^z \end{pmatrix} = \begin{pmatrix} 0 & 0 & -1 \\ 0 & 1 & 0 \\ 1 & 0 & 0 \end{pmatrix} \begin{pmatrix} P_{fp}^x \\ P_{fp}^y \\ P_{fp}^z \end{pmatrix} \quad (4.46)$$

Since the bend is only in the xz plane the bend angle is given by:

$$\theta_{bend} = \cos^{-1}(\vec{P}_i \cdot \vec{P}_f) \quad (4.47)$$

From eqn. 3.5, then, the spin precession angle is:

$$\chi = \theta_{bend} \gamma \left(\frac{g}{2} - 1 \right) \quad (4.48)$$

where $\gamma = \sqrt{\left(\frac{P}{M_p}\right)^2 + 1}$.

4.6 Extraction of Polarizations

The last section described the event selection and trajectory determination procedures. The interesting “physics”, however, is not in the individual events but in the overall collection of events. Recall from chapter 2 that our purpose for using the FPP was to measure the outgoing proton polarization in an $(\vec{e}, e' \vec{p})$ reaction. This involves measuring the $\vec{p}^{-12}\text{C}$ angular distribution (eq. 2.4) from the scattering that occurs in the FPP’s carbon:

$$I(\theta, \phi) = I_0(\theta) [1 - p_x^{fp} A_c(\theta) \sin \phi + p_y^{fp} A_c(\theta) \cos \phi] \quad (4.49)$$

or, in terms of the measured asymmetries $\epsilon_x(\theta)$ and $\epsilon_y(\theta)$:

$$I(\theta, \phi) = I_0(\theta) [1 + \epsilon_y \cos \phi + \epsilon_x \sin \phi] \quad . \quad (4.50)$$

The polarizations are just

$$p_{x(y)}^{fp} = \frac{\epsilon_{x(y)}(\theta)}{A_c(\theta)} \quad (4.51)$$

(with the proper sign, of course). Recall also from chapter 2 that the focal plane polarizations are related to the initial target polarizations by the spectrometer's spin precession angle χ .

Equation 4.50 includes physical asymmetries but not intrinsic systematic ones. Their effects on the polarimeter's azimuthal response can be represented by a Fourier series: ^[51]

$$\xi(\theta, \phi) = 1 + \sum_{m=1}^{\infty} e_m(\theta) \cos(m\phi) + \sum_{m=1}^{\infty} \bar{e}_m(\theta) \sin(m\phi) \quad , \quad (4.52)$$

where $\xi(\theta, \phi)$ is normalized to one in the absence of any systematic azimuthal asymmetry. Thus the actual measured distribution $N(\theta, \phi)$ is the physical distribution modified by the systematic effects:

$$\begin{aligned} N(\theta, \phi) &= I(\theta, \phi) \xi(\theta, \phi) \\ &= I_0(\theta) R(\theta, \phi) \quad , \end{aligned} \quad (4.53)$$

where

$$\begin{aligned} R(\theta, \phi) &= [1 + (\epsilon_y \cos \phi + \epsilon_x \sin \phi)] \\ &\times [1 + \sum_{m=1}^{\infty} e_m(\theta) \cos(m\phi) + \sum_{m=1}^{\infty} \bar{e}_m(\theta) \sin(m\phi)] \quad . \end{aligned} \quad (4.54)$$

[51] D.H. Barkhuff, private communication.

Using simple trigonometry addition formulas, this is:

$$\begin{aligned}
 R(\theta, \phi) = 1 + \sum e_m(\theta) \cos(m\phi) + \sum \bar{e}_m(\theta) \sin(m\phi) \\
 + \epsilon_y \left\{ \cos \phi + \frac{1}{2} \sum e_m(\theta) [+ \cos(m-1)\phi + \cos(m+1)\phi] \right. \\
 \left. + \frac{1}{2} \sum \bar{e}_m(\theta) [+ \sin(m-1)\phi + \sin(m+1)\phi] \right\} \\
 + \epsilon_x \left\{ \sin \phi + \frac{1}{2} \sum e_m(\theta) [- \sin(m-1)\phi + \sin(m+1)\phi] \right. \\
 \left. + \frac{1}{2} \sum \bar{e}_m(\theta) [+ \cos(m-1)\phi - \cos(m+1)\phi] \right\} .
 \end{aligned} \tag{4.55}$$

Many different sums involving good events were created so that overall averages could be determined. For example, sums of the spin precession in the spectrometer χ : $\sum_{ev} \chi$, $\sum_{ev} \cos \chi$, and $\sum_{ev} \sin \chi$ were needed. Various kinematic factor sums were needed for the determination of G_E/G_M and the beam helicity. Most importantly, the good events were summed five different ways by (helicity state) $\times(\phi$ -bin). These five different sums were: $\sum_{ev} 1$, $\sum_{ev} \cos \phi$, $\sum_{ev} \cos 2\phi$, $\sum_{ev} \sin \phi$, and $\sum_{ev} \sin 2\phi$. These were used to determine the focal plane asymmetries (real and systematic), using the Fourier analysis method developed by fellow graduate student David Barkhuff and described in the following paragraphs.

The asymmetries $\epsilon_{x(y)}$ of eq. 4.50, assuming full azimuthal acceptance, are determined by integrals of the distribution weighted by $\cos \phi$, $\sin \phi$, and 1: ^[52]

$$\begin{aligned}
 \epsilon_y \int_0^{2\pi} d\phi I(\theta, \phi) &= 2 \int_0^{2\pi} d\phi I(\theta, \phi) \cos \phi \\
 \epsilon_x \int_0^{2\pi} d\phi I(\theta, \phi) &= 2 \int_0^{2\pi} d\phi I(\theta, \phi) \sin \phi .
 \end{aligned} \tag{4.56}$$

For the situation where intrinsic systematic asymmetries are present the

[52] D. Besset *et al.*, Nuc. Inst. Meth. **166**, 515 (1979).

weighted integrals $u_j(\theta)$ and $v_j(\theta)$ are defined as:

$$\begin{aligned} u_j \int_0^{2\pi} d\phi N(\theta, \phi) &= \int_0^{2\pi} d\phi N(\theta, \phi) \cos(j\phi) \\ v_j \int_0^{2\pi} d\phi N(\theta, \phi) &= \int_0^{2\pi} d\phi N(\theta, \phi) \sin(j\phi) \end{aligned} \quad (4.57)$$

These integrals are estimated by sums over the observed events so that

$$\begin{aligned} u_j &\approx 1/N \sum_{ev} \cos(j\phi) \equiv \overline{\cos(j\phi)} \\ v_j &\approx 1/N \sum_{ev} \sin(j\phi) \equiv \overline{\sin(j\phi)} , \end{aligned} \quad (4.58)$$

where $N = \sum_{ev} 1$.

It should be pointed out that, although we initially binned our sums by θ in addition to helicity and ϕ , we ultimately determined that it did not affect the final result. Thus the measured asymmetries ϵ_x and ϵ_y and the weighted integrals u_j and v_j were integrated over θ . Also, the analyzing power used in equation 4.49 was an average analyzing power $\overline{A_c}$ rather than a θ -dependent one. The average came from a sum of analyzing powers calculated for each good event using that event's θ and kinetic energy. The analyzing power used was an average of four different models. The four models were of two slightly different model forms (the SIN^[30] and LAMPF^[31] forms), fit both with and without our IUCF 200 MeV data. All four fits used the data from SIN and LAMPF. The standard deviation around the mean of the models was a third of one percent; better than the overall 2% uncertainty of the models.

If there are no systematic asymmetries, evaluation of the eq. 4.57 integrals shows the only nonvanishing averages to be u_1 and v_1 , which equal $\epsilon_y/2$ and $\epsilon_x/2$, respectively. In this case u_1 and v_1 are directly proportional to the physical asymmetries. Conversely, if there are no physical asymmetries, u_j and v_j equal $e_j/2$ and $\bar{e}_j/2$, making them directly proportional to the systematic

asymmetries. More generally, however, when there are both physical and systematic asymmetries, one gets:

$$\begin{aligned} u_1 &= \frac{\epsilon_y (2 + e_2) + \epsilon_x \bar{e}_2 + 2e_1}{4 + 2\epsilon_y e_1 + 2\epsilon_x \bar{e}_1} \\ v_1 &= \frac{\epsilon_x (2 - e_2) + \epsilon_y \bar{e}_2 + 2\bar{e}_1}{4 + 2\epsilon_y e_1 + 2\epsilon_x \bar{e}_1} \end{aligned} \quad (4.59)$$

This becomes a pair of inhomogeneous linear equations:

$$\begin{aligned} \alpha_y \epsilon_y + \beta_y \epsilon_x - \delta_y &= 0 \\ \alpha_x \epsilon_y + \beta_x \epsilon_x - \delta_x &= 0 \end{aligned} \quad (4.60)$$

where the coefficients are given by

$$\begin{aligned} \alpha_y &= 1 + \frac{1}{2}e_2 - u_1 e_1 & \alpha_x &= \frac{1}{2}\bar{e}_2 - v_1 e_1 \\ \beta_y &= \frac{1}{2}\bar{e}_2 - u_1 \bar{e}_1 & \beta_x &= 1 - \frac{1}{2}e_2 - v_1 \bar{e}_1 \\ \delta_y &= 2u_1 - e_1 & \delta_x &= 2v_1 - \bar{e}_1 \end{aligned} \quad (4.61)$$

Thus the observed sums, the physical asymmetries, and the systematic asymmetries are related by the matrix equation:

$$\mathbf{W}^{-1} \boldsymbol{\epsilon} = \boldsymbol{\delta} \quad (4.62)$$

where

$$\mathbf{W}^{-1} = \begin{pmatrix} \alpha_y & \beta_y \\ \alpha_x & \beta_x \end{pmatrix} \quad \boldsymbol{\epsilon} = \begin{pmatrix} \epsilon_y \\ \epsilon_x \end{pmatrix} \quad \boldsymbol{\delta} = \begin{pmatrix} \delta_y \\ \delta_x \end{pmatrix} \quad (4.63)$$

From this equation it is clear that the physical and systematic asymmetries cannot be simultaneously determined. However, when unpolarized electrons scatter on protons there are no physical asymmetries so the systematic asymmetries e_j and \bar{e}_j can be determined as described earlier. These can then be used to extract the physical asymmetries from the data.

Equation 4.62 can be rewritten as

$$\begin{pmatrix} \epsilon_y \\ \epsilon_x \end{pmatrix} = |\mathbf{W}| \begin{pmatrix} 1 - \frac{1}{2}e_2 - v_1 \bar{e}_1 & u_1 \bar{e}_1 - \frac{1}{2}\bar{e}_2 \\ v_1 e_1 - \frac{1}{2}\bar{e}_2 & 1 + \frac{1}{2}e_2 - u_1 e_1 \end{pmatrix} \begin{pmatrix} 2u_1 - e_1 \\ 2v_1 - \bar{e}_1 \end{pmatrix} \quad (4.64)$$

where the determinant is given by:

$$|W|^{-1} = 1 - v_1 \bar{e}_1 - u_1 e_1 + \frac{v_1}{2}(e_1 \bar{e}_2 - \bar{e}_1 e_2) + \frac{u_1}{2}(e_1 e_2 + \bar{e}_1 \bar{e}_2) - \frac{1}{4}(e_2^2 + \bar{e}_2^2). \quad (4.65)$$

If the systematic asymmetries are small, a good estimate of the statistical uncertainty in the physical asymmetries can be obtained by keeping only the first order terms in e_j and \bar{e}_j . Then the determinant is approximated by:

$$|W| \approx 1 + v_1 \bar{e}_1 + u_1 e_1, \quad (4.66)$$

so that

$$\begin{aligned} \begin{pmatrix} \epsilon_y \\ \epsilon_x \end{pmatrix} &\approx \begin{pmatrix} 1 - \frac{1}{2}e_2 + u_1 e_1 & u_1 \bar{e}_1 - \frac{1}{2}\bar{e}_2 \\ v_1 e_1 - \frac{1}{2}\bar{e}_2 & 1 + \frac{1}{2}e_2 + v_1 \bar{e}_1 \end{pmatrix} \begin{pmatrix} 2u_1 - e_1 \\ 2v_1 - \bar{e}_1 \end{pmatrix} \\ &\approx \begin{pmatrix} 2u_1(1 + u_1 e_1 + v_1 \bar{e}_1) - e_1 - u_1 e_2 - v_1 \bar{e}_2 \\ 2v_1(1 + u_1 e_1 + v_1 \bar{e}_1) - \bar{e}_1 - u_1 \bar{e}_2 - v_1 e_2 \end{pmatrix} \end{aligned} \quad (4.67)$$

(to first order). Provided they are small compared to those in u_1 and v_1 , one can ignore the statistical uncertainties in e_j and \bar{e}_j . By rewriting the event sums of eq. 4.58 as sums of different ϕ bins:

$$\sum_{ev} \cos(j\phi) = \sum_i^N n_i \cos(j\phi_i), \quad (4.68)$$

where n_i is the number of events in the i th of N phi bins so that $N = \sum_i n_i$, the statistical uncertainties are given by:

$$\begin{pmatrix} \sigma_y^2 \\ \sigma_x^2 \end{pmatrix} = \begin{pmatrix} (\partial \epsilon_y / \partial u_1)^2 & (\partial \epsilon_y / \partial v_1)^2 \\ (\partial \epsilon_x / \partial u_1)^2 & (\partial \epsilon_x / \partial v_1)^2 \end{pmatrix} \begin{pmatrix} \sum_i (\partial u_1 / \partial n_i)^2 \sigma_{n_i}^2 \\ \sum_i (\partial v_1 / \partial n_i)^2 \sigma_{n_i}^2 \end{pmatrix}.$$

Note that $\sigma_{n_i}^2 = n_i$. Performing the differentiations and using eq. 4.58, the statistical uncertainties are:

$$\begin{aligned} \begin{pmatrix} \sigma_y^2 \\ \sigma_x^2 \end{pmatrix} &= \begin{pmatrix} (1 + 2u_1 e_1 + v_1 \bar{e}_1 - \frac{1}{2}e_2)^2 & (u_1 \bar{e}_1 - \frac{1}{2}\bar{e}_2)^2 \\ (v_1 e_1 - \frac{1}{2}\bar{e}_2)^2 & (1 + u_1 e_1 + 2v_1 \bar{e}_1 - \frac{1}{2}e_2)^2 \end{pmatrix} \\ &\times \frac{2}{N} \begin{pmatrix} 1 + u_2 - 2u_1^2 \\ 1 - u_2 - 2u_1^2 \end{pmatrix}. \end{aligned} \quad (4.69)$$

Using these results the average focal plane polarizations for each helicity state can be determined (remember the minus sign for p_x^{fp}):

$$\bar{p}_i^{fp} = \frac{\epsilon_i}{A_c} \quad (4.70)$$

and

$$\sigma(\bar{p}_i^{fp}) = \frac{\sigma(\epsilon_i)}{A_c} \quad (4.71)$$

4.7 Quadrupole Depolarization Effects

The method of determining the target polarizations and G_E/G_M using the helicity states and the spin precession in OHIPS's dipole was described in section 2.2. Precession also occurs in the magnetic fields of the quadrupoles, however, and failure to account for this results in the determined target polarizations being lower than they should, or "depolarized". The polarizations are lowered because the polarization is in actuality an average over many different spin rotation directions and failure to account for any effect that randomizes the spin rotation directions will lower this average. Quantifying this effect is more difficult for quadrupoles because, unlike dipoles, their magnetic fields are inhomogeneous. Our solution to this problem is based on the work of Nurushhev. [53]

The Thomas equation (3.1) reduces to

$$\begin{aligned} \frac{d\vec{p}}{dt} &= \frac{ev}{pc} \vec{p} \times \left[\frac{g}{2} \vec{B}_L + \left(1 + \frac{g-2}{2} \gamma \right) \vec{B}_T \right] \\ &= \frac{ev}{pc} \vec{p} \times \vec{A} \end{aligned} \quad (4.72)$$

in the absence of an electric field. B_L and B_T are the magnetic field components parallel and perpendicular to the particle's velocity, respectively. If the particle

[53] S. Nurushhev, Nuc. Inst. Meth. 141, 417 (1977).

(in this case a proton) moves in the z -direction with a constant velocity the polarization components are:

$$\frac{dp_k}{dz} = \frac{e}{pc} \epsilon_{ijk} p_i A_j \quad . \quad (4.73)$$

Integrating this gives:

$$p_k(z) = p_k(0) + \frac{e}{pc} \epsilon_{ijk} \int_0^z p_i(\zeta) a_j(\zeta) d\zeta \quad . \quad (4.74)$$

Assuming the fields in a quadrupole can be modeled as $\vec{B}_L = 0$ and $\vec{B}_T = G(y\hat{x} + x\hat{y})$, the equations of motion for a particle in a quadrupole are:

$$\begin{aligned} x'' \pm K^2 x &= 0 \\ y'' \mp K^2 y &= 0 \quad , \end{aligned} \quad (4.75)$$

where $K^2 = \frac{eG}{pc}$ and the upper(lower) signs refer to vertical and horizontal focusing quadrupoles, respectively. (Recall the TRANSPORT coordinates of figure 4.4.) This results in eq. 4.74 becoming:

$$\begin{aligned} p_t(z) &= p_t(0) - \lambda \int_0^z p_l(\zeta) y(\zeta) d\zeta \\ p_n(z) &= p_n(0) + \lambda \int_0^z p_l(\zeta) x(\zeta) d\zeta \\ p_l(z) &= p_l(0) + \lambda \int_0^z [p_t(\zeta) y(\zeta) - p_n(\zeta) x(\zeta)] d\zeta \quad , \end{aligned} \quad (4.76)$$

where $\lambda = (1 + \frac{q-2}{2}\gamma)K^2$. Solving these equations, taking the above equations of motion into account, quadrupole matrix elements (as given in ref. [53]) can be determined for relating $p_i(z)$ at the focal plane to $p_k(0)$ at the target. This was done with a Monte Carlo calculation where a realistic population of the aperture was used so that average matrix elements could be obtained. For hydrogen, the kinematic correlation between momentum and scattering angle was enforced in the calculation.

Kinematics	$\Delta p_t/p_t$	$\Delta p_n/p_n$	$\Delta p_l/p_l$
Q2	0.065	2.26	0.123
Q3	0.075	2.61	0.096

Table 4.3. Change in target polarizations after taking quadrupole effects into account.

For our spectrometer setup of two quadrupoles and a dipole we have:

$$\mathbf{p}_{fp} = \mathbf{M}_D \mathbf{M}_{Q2} \mathbf{M}_{Q1} \mathbf{p}_{tgt} \quad . \quad (4.77)$$

We measured four things at the focal plane: p_x and p_y for both helicities. Writing these in terms of sums and differences (divided by 2), the measured quantities are related to the target polarization vector via:

$$\begin{pmatrix} \Sigma y \\ \Delta y \\ \Sigma x \\ \Delta x \end{pmatrix} = \begin{pmatrix} 0 & \langle Q_{12} \rangle & 0 \\ \langle Q_{11} \rangle & 0 & \langle Q_{13} \rangle \\ 0 & \langle -Q_{22} \cos \chi \rangle & 0 \\ & \langle -Q_{33} \sin \chi \rangle & \\ \langle -Q_{21} \cos \chi \rangle & 0 & \langle -Q_{23} \cos \chi \rangle \\ \langle -Q_{31} \sin \chi \rangle & & \langle -Q_{33} \sin \chi \rangle \end{pmatrix} \begin{pmatrix} p_t^{tgt} \\ p_n^{tgt} \\ p_l^{tgt} \end{pmatrix} , \quad (4.78)$$

where the quadrupole matrix elements Q_{ij} represent the combined effects of both quadrupoles. Using the pseudo-inverse $\mathbf{M}_{total}^+ = (\mathbf{M}_{total}^T \mathbf{M}_{total})^{-1} \mathbf{M}_{total}^T$, the least squares estimates of the target polarization are obtained as

$$\begin{pmatrix} p_t^{tgt} \\ p_n^{tgt} \\ p_l^{tgt} \end{pmatrix} = \mathbf{M}_{total}^+ \begin{pmatrix} \Sigma y \\ \Delta y \\ \Sigma x \\ \Delta x \end{pmatrix} . \quad (4.79)$$

Table 4.3 lists the increases in our target polarization values once we took the quadrupole effects into account.

Chapter 5

Results

Table 5.1 lists the experimental kinematics. Measurements were taken at two different Q^2 values (0.38 and 0.50 GeV^2). The initial beam energy was approximately 580 MeV; or 579.05 MeV at the hydrogen target center. The momenta in the table include the effects of target losses.

5.1 Systematic Errors

There are three contributors to the systematic errors of our experiment: the beam helicity uncertainty, the analyzing power uncertainty, and the uncertainty in the depolarization effects of the spectrometer magnets. (The last one includes kinematic uncertainties.) The helicity uncertainty was 4% and contributed to the error of p_l and p_t . Table 5.2 ^[54] gives the individual contributions to this systematic error. $A_y(\theta)$'s absolute error of ± 0.02 gives a relative error of about 0.04 that affects all of the polarizations. Tables 5.3 and 5.4 detail the systematic error from the uncertainty in the magnetic depolarization effects for $Q^2 = 0.38 \text{ GeV}^2$ and $Q^2 = 0.50 \text{ GeV}^2$, respectively. For p_l the uncertainty in beam's vertical position at the target dominated the error while p_t 's error was dominated by the uncertainties in ϕ_{tgt} and the beam's horizontal position at the target. The systematic uncertainties for p_n were minimal. Note that the magnet depolarization effect systematic errors associated with p_t and p_l are not correlated. This means that both must be included in the systematic error of

^[54] K. Joo, private communication.

$Q^2(\text{GeV}^2)$	0.38	0.50
θ_e (deg)	82.72	113.87
E' (MeV)	376.3	310.2
p_{MEPS} (MeV/c)	375.3	309.2
θ_p (deg)	35.22	22.03
ω (MeV)	202.8	268.9
p_{OHIPS} (MeV/c)	645.9	756.9
Carbon thick. (cm)	7	9.5
p_{carbon}^{center} (MeV/c)	174.0	237.0
Total charge (C)	1.6	1.0
Avg. hel. (%)	30.9	28.2
Total good counts	1935342	754067
$\bar{\chi}$	195.87	207.47

Table 5.1 Experiment Kinematics

G_E/G_M . Tables 5.5 and 5.6 summarize the systematic errors for the two Q^2 measurements.

The helicity uncertainty is common to both Q^2 measurements and is therefore an overall systematic error. Likewise, the analyzing power uncertainties are common to both p_t and p_l , though they are different for the separate Q^2 measurements, as those were done with different proton kinetic

Description	Error (%)
Beam position fluctuation	2.5
Signal to background ratio uncertainty	1.5
Target polarization uncertainty	1.3
Target angle uncertainty	1.5
Systematic diff. between 2 detectors	1.8
Helicity correlated uncertainty	0.2
Intra-atomic motion of bound electrons	0.3
Total Systematic Error	4.0

Table 5.2 *Møller Systematic Errors*

energies (T_p) and different carbon analyzer thicknesses. The uncertainties in the magnet depolarization effects are unique to each measured polarization for both Q^2 measurements.

5.2 Results

Figure 5.1 displays our experiment's measured polarizations versus their theoretical values from the plane wave impulse approximation (PWIA) using a dipole fit. Since p_t and p_l scale with helicity the polarization transfer coefficients $D_{lj}(= p_j/h)$ are given instead to provide a basis of comparison with other experiments. The inner error bars are statistical while the outer are statistical with the systematic magnet depolarization effects added in

Description	$\Delta p_t/p_t$	$\Delta p_l/p_l$
beam energy: ± 1 MeV	0	0.0049
beam horiz. tgt. pos.: ± 1 mm	0.0070	0.0025
beam vert. tgt. pos.: ± 1 mm	0	0.0250
$\phi_{tgt} : \pm 0.9$ mrad	0.0066	0.0043
quad. 1 to quad. 2 vert. align.: ± 0.35 mm	0	0.0012
quad. 1 to quad. 2 horiz. align.: ± 0.61 mm	0.0021	0.0015
quad. to dipole vert. align.: ± 0.32 mm	0	0.0010
Total Systematic Error	0.010	0.026

Table 5.3 Magnet Depolarization Systematic Errors for $Q^2 = 0.38 \text{ GeV}^2$

quadrature. In addition, there are systematic uncertainties from the beam helicity and analyzing power which, as they are common overall uncertainties, are not included in the displayed error bars. The size of the overall systematic error for each polarization is noted at the bottom of figure. All of the measured polarizations are near their theoretical value, though D_{lt} for $Q^2 = 0.38 \text{ GeV}^2$ is a little low. Tables 5.7 and 5.8 list the measured results for $Q^2 = 0.38 \text{ GeV}^2$ and $Q^2 = 0.50 \text{ GeV}^2$, respectively.

Also included in the figure are preliminary polarizations measured from deuterium during runs interspersed with the hydrogen ones during this

Description	$\Delta p_t/p_t$	$\Delta p_l/p_l$
beam energy: ± 1 MeV	0	0.0020
beam horiz. tgt. pos.: ± 1 mm	0.0124	0.0030
beam vert. tgt. pos.: ± 1 mm	0	0.0143
$\phi_{tgt} : \pm 0.9$ mrad	0.0127	0.0030
quad. 2 to quad. 1 vert. align.: ± 0.35 mm	0	0.0006
quad. 2 to quad. 1 horiz. align.: ± 0.61 mm	0.0035	0.0010
quad. to dipole vert. align.: ± 0.32 mm	0	0.0006
Total Systematic Error	0.038	0.022

Table 5.4 Magnet Depolarization Systematic Errors for $Q^2 = 0.50$ GeV²

	$\Delta p_l/p_l$	$\Delta p_t/p_t$	$\Delta p_n/p_n$	$\Delta G_{rat}/G_{rat}$
$\Delta h/h$	0.04	0.04	—	—
$\Delta A_y/A_y$	0.04	0.04	0.04	—
Magnet depol. effects	0.038	0.024	0.0022	0.044

Table 5.5 $Q^2 = 0.38$ GeV² Systematic Errors

	$\Delta p_l/p_l$	$\Delta p_t/p_t$	$\Delta p_n/p_n$	$\Delta G_{rat}/G_{rat}$
$\Delta h/h$	0.04	0.04	—	—
$\Delta A_y/A_y$	0.04	0.04	0.04	—
Magnet depol. effects	0.022	0.038	0.0033	0.044

Table 5.6 $Q^2 = 0.50 \text{ GeV}^2$ Systematic Errors

$Q^2(\text{GeV}^2)$	0.38
p_n^{tgt}	$-0.0034 \pm .0020 \pm .00001 \pm .0001$
D_{lt}^{tgt}	$-0.468 \pm .006 \pm .005 \pm .027$
D_{ll}^{tgt}	$0.609 \pm .023 \pm .016 \pm .035$
$\mu G_E/G_M$	$0.941 \pm .038 \pm .027$

Table 5.7. Experiment Results for $Q^2 = 0.38 \text{ GeV}^2$. The first errors are statistical. The second errors are systematic uncertainties due to magnet depolarization effects and the third are correlated overall uncertainties from the beam helicity and A_y .

experiment. [55] Their consistency with the hydrogen results shows that polarization transfer coefficients on the deuteron are not greatly affected by nuclear binding and interaction effects. This implies that polarization transfer

[55] J. McIntyre, private communication.

$Q^2(\text{GeV}^2)$	0.50
p_n^{tgt}	$0.0003 \pm .0034 \pm .000001 \pm .00001$
D_{lt}^{tgt}	$-0.434 \pm .011 \pm .008 \pm .026$
D_{ll}^{tgt}	$0.882 \pm .023 \pm .013 \pm .050$
$\mu G_E / G_M$	$0.996 \pm .036 \pm .023$

Table 5.8. Experiment Results for $Q^2 = 0.50 \text{ GeV}^2$. The first errors are statistical. The second errors are systematic uncertainties due to magnet depolarization effects and the third are correlated overall uncertainties from the beam helicity and A_y .

measurements hold great promise for determining G_E^n .

Finally, Figure 5.2 displays the $\mu_p G_E^p / G_M^p$ ratios that we obtained (dark diamonds), along with previous data from Rosenbluth separation experiments. Again, the inner error bars are statistical while the outer ones are statistical and systematic added in quadrature. Unlike the polarizations, the ratios are independent of uncertainties in the beam helicity and A_y . The fits are described in section 1.5. The previous data are from: Bartel *et al.* ^[18] (open squares), Janssens *et al.* ^[21] (Xs), and Höhler *et al.* ^[9] (open circles). The dark circles are our preliminary data from the deuteron (offset for clarity).

5.3 Conclusion and Recommendations

This experiment has successfully measured polarization transfers in the $^1\text{H}(\vec{e}, e' \vec{p})$ reaction. While the transverse polarization transfer has previously

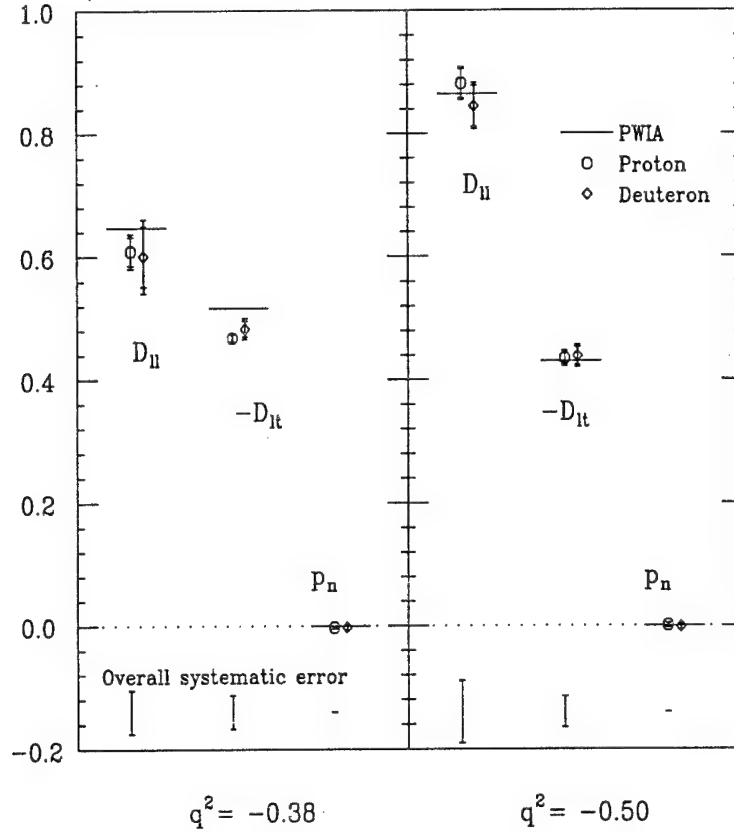


Figure 5.1 Measured polarizations. The inner error bars are statistical while the outer error bars are statistical errors added in quadrature with the uncertainties due to magnet depolarization effects. The overall uncertainties from the beam helicity and analyzing power are not shown.

been measured in this manner at Mainz, ^[3] this is the first experiment to measure all three polarization components and determine the ratio G_E^p/G_M^p . The ratio measured is consistent with the dipole model and has error bars comparable to previous measurements using Rosenbluth separation. Thus the

^[3] D. Eyl *et al.*, Z. Phys. A352, 211 (1995).

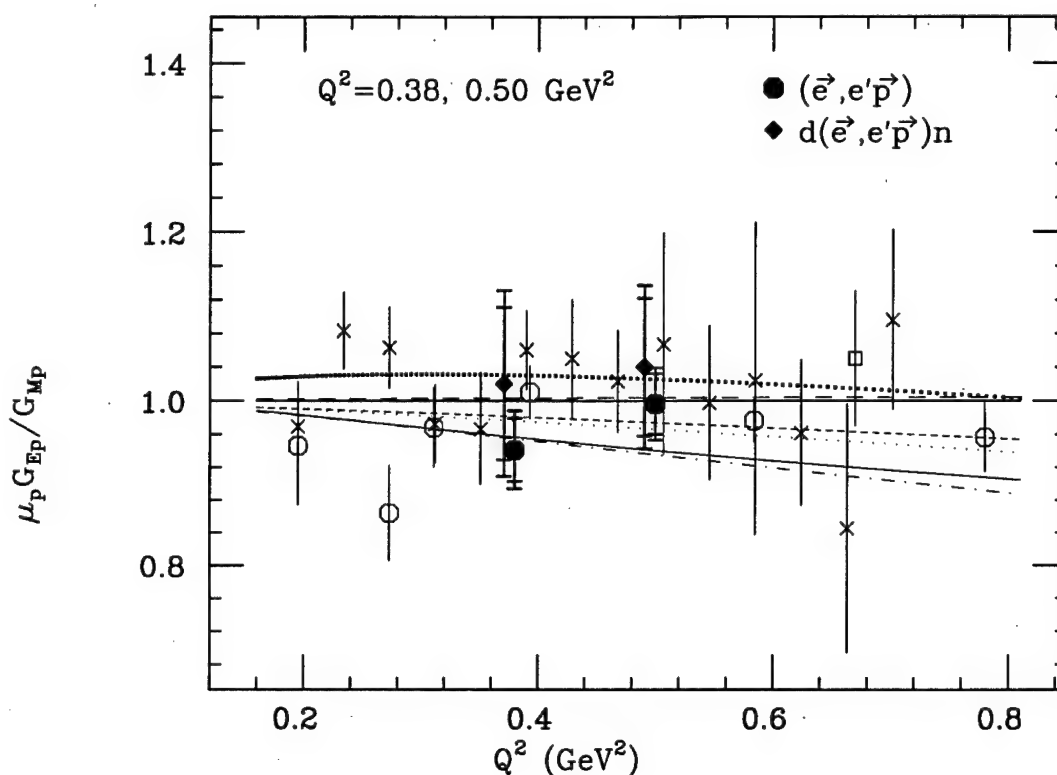


Figure 5.2 $\mu_p G_E^p / G_M^p$ vs. Q^2 . The symbols and fits are listed in the text.

groundwork has been laid for an alternative method of determining form factors, particularly at higher Q^2 -values^[29] where G_E can be difficult to extract using Rosenbluth separation.

As a proof-of-principle experiment, this experiment, though successful, has revealed unexpected problems that hopefully can be avoided in future similar experiments. For example, I believe there is room for a significant improvement in the data rate since nearly half of our acquired data had to be discarded due to irreducible multi-hits. Given the large number of wire chambers needed for this experiment, shielding is probably more important than in the typical $(e, e'p)$ experiment. The use of redundant chambers (i.e., more than two) on both sides of the analyzer would also help, though it might necessitate a more

creative small-angle rejection system.

I would also recommend that future polarimeters be built to make alignment easier than ours and that experimenters treat its determination with a higher priority than we did. If we had had to replace a wire chamber later in our experiment, we could have been in trouble concerning our alignment offsets, as we did not do a "straight-through" run until well after the experiment was over. Such a run should be the first thing done. Then, with the chambers and supports designed to allow known adjustments to be made easily, one could ensure that the small angle rejection system did not bias the data nearly as much as ours, thus raising the useful percentage of data acquired.

Finally, this experiment shows that spin transfer physics requires well understood magnetic fields and magnet alignments. This experiment was done on a spectrometer with unmapped fields. Knowledge of the actual fields as a function of position would have allowed us to better determine the spin transport effects in the magnets, as well as the focal plane to target coordinate transformations. Better knowledge of the relative alignments of the spectrometer magnets themselves and, more importantly, better stability and knowledge of the beam position at the target would have also reduced systematic errors.

Appendix A

Derivation of Cross Section Relationships

This appendix provides detailed derivations of differential cross section and polarization equations used in this dissertation for scattering electrons off protons. The first section details the necessary formalism to start from transition currents and the Dirac equation and arrive at a differential cross section in terms of an invariant scattering amplitude. The next section introduces a reference frame - the Breit frame - which will be used in evaluating the scattering amplitude. The third section describes the proton transition current in this frame, while in the last two sections the cross section relations for both unpolarized electrons, giving the Rosenbluth equation, and for polarized electrons, are derived.

A.1 Cross Section Formalism

In this section the formalism leading up to the electron-nucleon scattering cross section is developed as in Halzen and Martin ^[57] and Chinitz. ^[58] The basic ingredient is the current-current interaction as depicted in figure A.1 in which the electron's transition current j_{fi}^μ interacts with the proton's transition current J_μ^{fi} . The first step in calculating the cross section is to determine just what these currents are.

[57] F. Halzen and A.D. Martin, *Quarks and Leptons*, John Wiley & Sons, (1984).

[58] L.M. Chinitz, Ph.D. dissertation, U.Va. (1990), unpublished.

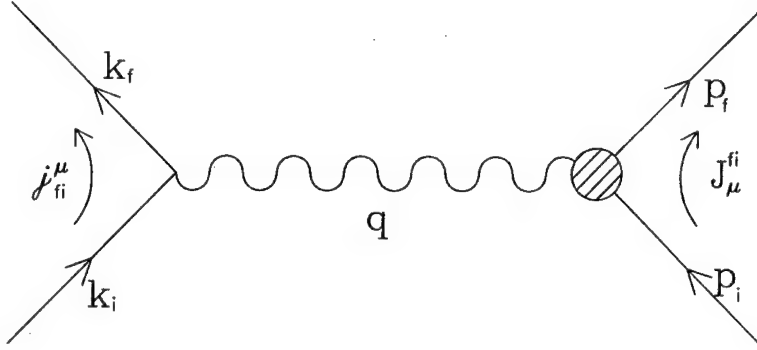


Figure A.1 Transitions currents in electron-nucleon scattering.

The relativistic Dirac equation for spin- $\frac{1}{2}$ particles is

$$H\psi = (\boldsymbol{\alpha} \cdot \mathbf{P} + \beta m)\psi \quad , \quad (\text{A.1})$$

which can be written covariantly as

$$(\gamma^\mu p_\mu - m)\psi = 0 \quad . \quad (\text{A.2})$$

For free electrons, the wave function

$$\psi = u(\mathbf{p})e^{-ip \cdot x} \quad , \quad (\text{A.3})$$

where $u(\mathbf{p})$ is a four-component spinor, satisfies this equation. Using (A.2) and the continuity equation, $\partial_\mu j^\mu = 0$, gives the electron's transition current between its initial and final states as:

$$\begin{aligned} j_{fi}^\mu &= -e \bar{\psi}_f \gamma^\mu \psi_i \\ &= -e \bar{u}_f \gamma^\mu u_i e^{i(p_f - p_i) \cdot x} \quad . \end{aligned} \quad (\text{A.4})$$

Since the nucleon is not a point-particle, J_μ cannot be written in the same way as j^μ . The vertex factor γ_μ must be replaced by a term $\Gamma_\mu(p_f, p_i)$ that contains the nucleon's structure information. This makes the nucleon's

transition current:

$$J_\mu = e \bar{u}_f \Gamma_\mu(p_f, p_i) u_i e^{i(p_f - p_i) \cdot x} \quad (A.5)$$

If one were at the quark level, however, a point-particle vertex could still be used. Then you would have

$$J_\mu^{fi} = \sum_j e_j \bar{q}_j^f \gamma_\mu q_j^i, \quad (A.6)$$

where e_j represents the fractional charge for each quark and q_j represents the quark wave functions. Instead, however, $\Gamma_\mu(p_f, p_i)$ must assume the most general four-vector form that can be constructed with p_f , p_i , $q (= p_f - p_i)$, and the γ matrices without violating parity conservation. This is:

$$\Gamma_\mu(p_f, p_i) = \gamma_\mu K_1 + i\sigma_{\mu\nu} q^\nu K_2 + i\sigma_{\mu\nu} (p_f + p_i)^\nu K_3 + q_\mu K_4 + (p_f + p_i)_\mu K_5 \quad (A.7)$$

The Gordon decomposition,

$$\bar{u}_f \gamma_\mu u_i = \frac{1}{2m} \bar{u}_f ((p_f + p_i)_\mu + i\sigma_{\mu\nu} q^\nu) u_i, \quad (A.8)$$

shows that the $(p_f + p_i)_\mu$ terms are really just linear combinations of the γ_μ and $\sigma_{\mu\nu} q^\nu$ terms, so that

$$\Gamma_\mu(p_f, p_i) = \gamma_\mu F_1 + \frac{i\kappa}{2M} \sigma_{\mu\nu} q^\nu F_2 + q_\mu F_3, \quad (A.9)$$

where M is the nucleon mass. Current conservation at the vertex gives that

$$q^\mu J_\mu = e \bar{u}_f (q^\mu \gamma_\mu F_1 + \frac{i\kappa}{2M} q^\mu \sigma_{\mu\nu} q^\nu F_2 + q^2 F_3) u_i = 0 \quad (A.10)$$

The first term in this equation is zero by the Dirac equation. The second is zero since it is a contraction of symmetric and antisymmetric tensors. This means that F_3 must be zero as well. Thus one is left with

$$\Gamma_\mu(p_f, p_i) = F_1(Q^2) \gamma_\mu + \frac{i\kappa}{2M} F_2(Q^2) \sigma_{\mu\nu} q^\nu \quad (A.11)$$

This equation is valid for both protons and neutrons, though the form factors for each are different. F_1 is called the Dirac form factor and F_2 is called the Pauli

form factor. κ is the anomalous magnetic moment. It is related to the magnetic moment μ by $\mu_N = F_1^N(0) + \kappa_N F_2^N(0)$. For protons $F_1^p(0) = F_2^p(0) = 1$ and $\mu_p = 2.79$, whereas for neutrons $F_1^n(0) = 0, F_2^n(0) = 1$ and $\mu_n = -1.91$. Hence in the real photon limit ($q^2 \rightarrow 0$), one basically probes a particle of magnetic moment $(1 + \kappa)\frac{e}{2M}$ and charge e (for the proton, 0 for the neutron).

The electron scattering off a nucleon in figure A.1 is not a free electron but rather is traveling in an electromagnetic field A_μ caused by J_μ . In classical electrodynamics the motion of an electron through an electromagnetic potential brings about the substitution

$$p_\mu \rightarrow p_\mu + eA_\mu \quad . \quad (A.12)$$

(As it turns out, requiring local gauge invariance on the electron Lagrangian mandates this substitution.) This changes the Dirac equation (A.2) to

$$(\gamma^\mu p_\mu - m)\psi = -e\gamma^\mu A_\mu \quad . \quad (A.13)$$

The field's potential is defined as

$$\gamma^0 V = -e\gamma^\mu A_\mu \quad . \quad (A.14)$$

By first order perturbation theory, the transition amplitude of a particle from an initial state to a final state in a potential is

$$T_{fi} = -i \int \psi_f^\dagger(x) V(x) \psi_i(x) d^4x \quad . \quad (A.15)$$

Using j_{fi}^μ (A.4), where $\bar{\psi} = \psi^\dagger \gamma^0$, and (A.14) transforms this to

$$T_{fi} = -i \int j_{fi}^\mu A_\mu d^4x \quad . \quad (A.16)$$

The relationship between A_μ and J_μ is given by Maxwell's equations, which are written covariantly in position-space as

$$\square^2 A_\mu(x) = J_\mu(x) \quad . \quad (A.17)$$

Fourier transforming this leads to the result that:

$$A_\mu(q) = -\frac{1}{q^2} J_\mu(q) \quad . \quad (A.18)$$

This makes the transition amplitude

$$T_{fi} = i \int j^\mu \frac{1}{q^2} J_\mu d^4x \quad . \quad (A.19)$$

Upon integration, T_{fi} can be written as

$$T_{fi} = \frac{-i(2\pi)^4}{V^2} \delta^4(k' + p' - k - p) \mathcal{M} \quad (A.20)$$

where V is the normalization volume and \mathcal{M} is the invariant scattering amplitude and equals

$$\mathcal{M} = -e^2 \bar{u}(k_f) \gamma^\mu u(k_i) \frac{1}{q^2} \bar{u}(p_f) \Gamma_\mu u(p_i) \quad . \quad (A.21)$$

For the scattering process $k + p \rightarrow k' + p'$, the transition rate per unit volume is defined as

$$W_{fi} = \frac{|T_{fi}|^2}{TV} \quad (A.22)$$

where T is the interaction's time interval. This is related to the cross section by

$$\sigma = \frac{W_{fi}}{(\text{initial flux})} (\text{number of final states}) \quad . \quad (A.23)$$

From phase space,

$$\text{number of final states} = \frac{V d^3 k'}{(2\pi)^3 2E'} \frac{V d^3 p'}{(2\pi)^3 2E'_p} \quad . \quad (A.24)$$

The initial flux in the lab frame is expressed as

$$\text{initial flux} = |\mathbf{v}_e| \frac{2E}{V} \frac{2E_p}{V} \quad . \quad (A.25)$$

For $m \ll E$, $\mathbf{v}_e = \frac{\mathbf{p}_e}{E}$ is ≈ 1 . Thus the lab frame cross section is

$$d\sigma = \frac{(2\pi)^4 |\mathcal{M}|^2}{4EM} \delta^4(k - k' + p - p') \frac{d^3 k'}{(2\pi)^3 2E'} \frac{d^3 p'}{(2\pi)^3 2E'_p} \quad . \quad (A.26)$$

Note that $\overline{|\mathcal{M}|^2}$ has been used rather than $|\mathcal{M}|^2$ since an unpolarized cross section needs to be averaged over the initial states and summed over the final states. The energy equation $E'^2 = k'^2 + m^2$ gives the relationship $E' dE' = k' dk'$ making

$$d^3 k' = k'^2 dk' d\Omega = E'^2 dE' d\Omega \quad . \quad (A.27)$$

For the lab frame one can also write

$$\begin{aligned} \int \frac{d^3 p'}{2E'_p} \delta(p + q - p') &= \frac{1}{2M} \delta(\omega + \frac{q^2}{2M}) \\ &\approx \frac{1}{2MA} \delta(E' - E/A) \end{aligned} \quad (A.28)$$

where

$$A = \frac{E}{E'} = 1 + \frac{2E}{M} \sin^2\left(\frac{\theta}{2}\right) \quad (A.29)$$

and the relationships

$$\omega = E - E' = \frac{Q^2}{2M} \quad (A.30)$$

and

$$Q^2 \approx 2k \cdot k' = 4EE' \sin^2\left(\frac{\theta}{2}\right) \quad (A.31)$$

have been used. Putting in these values makes the laboratory frame cross section equation

$$\frac{d\sigma}{d\Omega} = \frac{\overline{|\mathcal{M}|^2}}{64\pi^2 M^2} \left(\frac{E'}{E}\right)^2 \quad . \quad (A.32)$$

It is useful to write $\overline{|\mathcal{M}|^2}$ in terms of two tensors representing the two interacting particles:

$$L^{\mu\nu} = \frac{1}{2} \sum_{spins} [\bar{u}(k') \gamma^\mu u(k)] [\bar{u}(k') \gamma^\nu u(k)]^* \quad (A.33)$$

and

$$W_{\mu\nu} = \frac{1}{2} \sum_{spins} [\bar{u}(p') \Gamma_\mu u(p)] [\bar{u}(p') \Gamma_\nu u(p)]^* \quad (A.34)$$

for the electron and proton, respectively. This makes

$$|\overline{\mathcal{M}}|^2 = \frac{e^4}{q^4} L^{\mu\nu} W_{\mu\nu} \quad . \quad (A.35)$$

To evaluate these tensors note that the terms in brackets are 1×1 matrix elements. The consequence of this is that the terms's complex and hermitian conjugates are the same. Using $\gamma^\nu \dagger \gamma^0 = \gamma^0 \gamma^\nu$ gives

$$[\bar{u}(k') \gamma^\nu u(k)]^* = [\bar{u}(k) \gamma^\nu u(k')] \quad .$$

By writing out $L^{\mu\nu}$ now in terms of explicit matrix elements ^[59] and using the completeness relation

$$\sum_{s=1,2} u^{(s)}(p) \bar{u}^{(s)}(p) = \not{p} + m \quad (A.36)$$

(where $\not{p} = \gamma^\mu p_\mu$), the electron tensor becomes:

$$L^{\mu\nu} = \frac{1}{2} \text{Tr}((\not{k}' + m) \gamma^\mu (\not{k} + m) \gamma^\nu) \quad . \quad (A.37)$$

Using trace theorems and neglecting the mass-squared term gives

$$\begin{aligned} L^{\mu\nu} &= 2(k'^\mu k^\nu + k'^\nu k^\mu - (k \cdot k') g^{\mu\nu}) \\ &= 2(k'^\mu k^\nu + k'^\nu k^\mu) + q^2 g^{\mu\nu} \quad , \end{aligned} \quad (A.38)$$

where (A.31) was used. To evaluate the proton tensor, let's define a slightly different version of the nucleon transition current (A.5) without the electron charge and the exponent

$$\mathcal{J}_\mu = \bar{u}_f \Gamma_\mu(p_f, p_i) u_i \quad . \quad (A.39)$$

This allows the proton tensor to be written as

$$W_{\mu\nu} = \frac{1}{2} \text{Tr}(\mathcal{J}_\mu \mathcal{J}_\nu^\dagger) \quad . \quad (A.40)$$

All that is left is to further evaluate the transition currents and put in the appropriate momentum four-vector values. Since $|\overline{\mathcal{M}}|^2$ is an invariant this can

[59] J.D. Bjorken and S.D. Drell, *Relativistic Quantum Mechanics*, McGraw-Hill, (1964).

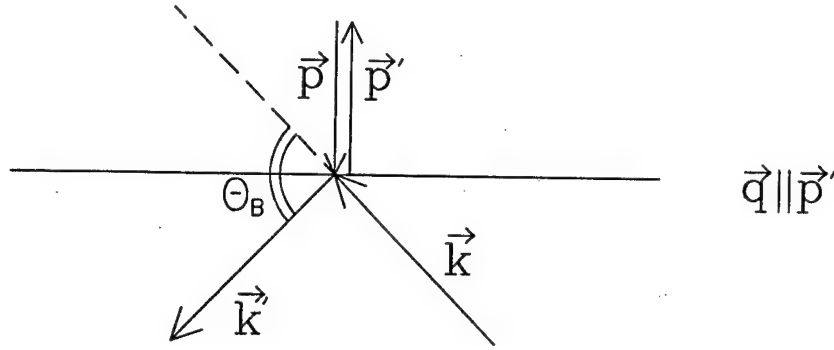


Figure A.2 Breit reference frame.

be done in whatever frame one chooses. The reference frame that we will use is the Breit frame, which is described in the next section.

A.2 The Breit Reference Frame

A useful reference frame for the evaluation of transition currents is the Breit frame. This is also called the brick wall frame since in this frame the proton and electron are essentially “bouncing” off a wall, as can be seen in figure A.2. In this frame $\vec{p} = -\vec{p}'$ and $\vec{q}_B \parallel \vec{p}'$.^[60] There is no energy transfer ($\omega = 0$) so

$$Q^2 = |\vec{q}_B|^2 \quad . \quad (A.41)$$

Since $\vec{q}_B = 2\vec{p}$ this means that

$$q_B^2 = -4|\vec{p}|^2 \quad . \quad (A.42)$$

If the z-axis is chosen along \vec{q}_B with scattering in the x-z plane the electron

^[60] R. Hagedorn, *Relativistic Kinematics*, W.A. Benjamin, (1973).

four momenta are: [61] [62]

$$\begin{aligned} k &= \frac{|\vec{q}_B|}{2} \left(\csc \frac{\theta_B}{2}, \cot \frac{\theta_B}{2}, 0, 1 \right) \\ k' &= \frac{|\vec{q}_B|}{2} \left(\csc \frac{\theta_B}{2}, \cot \frac{\theta_B}{2}, 0, -1 \right) . \end{aligned} \quad (A.43)$$

Since the Lorentz transformation from the laboratory frame to the Breit frame is entirely along the z -axis, the fact that x is the same in both frames can be used to get the relationship:

$$x = z \cot\left(\frac{\theta}{2}\right) = z_B \cot\left(\frac{\theta_B}{2}\right) \quad (A.44)$$

or

$$\cot^2\left(\frac{\theta}{2}\right) = \frac{z^2}{z_B^2} \cot^2\left(\frac{\theta_B}{2}\right) . \quad (A.45)$$

z and z_B are related by the Lorentz transformation as:

$$z^2 = (1 - \beta^2) z_B^2 , \quad (A.46)$$

where $\beta = v/c$.

All that is left is to establish a relationship between θ and θ_B is to determine the value of β . This can be done by looking at the Lorentz transformation from the lab to the Breit frame and using the fact that in the Breit frame $\vec{p} = -\vec{p}'$. The four momenta in the lab frame are $p_i = (M, 0)$ and $p_f = (M + \omega, \vec{q}_L)$, whereas in the Breit frame they are $p_{iB} = (E_B, \vec{p}_{iB})$ and $p_{fB} = (E_B, \vec{p}_{fB})$. Using the Lorentz transformations gives

$$\begin{pmatrix} E_B \\ \vec{p}_{iB} \end{pmatrix} = \begin{pmatrix} \gamma & -\beta\gamma \\ -\beta\gamma & \gamma \end{pmatrix} \begin{pmatrix} M \\ 0 \end{pmatrix} , \quad (A.47)$$

which leads to

$$p_{iBz} = -\beta\gamma M ; \quad (A.48)$$

[61] N. Dombey, Rev. Mod. Phys. 41, 236 (1969).

[62] A.I. Akhiezer and M.P. Rekalo, Fiz. Elem. Chast. Atom. Yad. 4, 662 (1973)[Sov. J. Part. Nucl. 4, 277 (1974)].

and

$$\begin{pmatrix} E_B \\ \vec{p}_{fB} \end{pmatrix} = \begin{pmatrix} \gamma & -\beta\gamma \\ -\beta\gamma & \gamma \end{pmatrix} \begin{pmatrix} M + \omega \\ \vec{q}_L \end{pmatrix}, \quad (\text{A.49})$$

which gives

$$p_{fB_z} = -\beta\gamma(M + \omega) + \gamma q_{L_z}. \quad (\text{A.50})$$

Equating p_{iB_z} and $-p_{fB_z}$ gives

$$\beta(2M + \omega) = q_{L_z} \quad (\text{A.51})$$

or

$$\beta^2 = \frac{q_{L_z}^2}{(2M + \omega)^2}. \quad (\text{A.52})$$

Since $q_L^2 = \omega^2 + Q^2$ this is:

$$\begin{aligned} \beta^2 &= \frac{\omega^2 + Q^2}{4M^2 + 4M\omega + \omega^2} \\ &= \frac{\frac{Q^4}{4M^2} + Q^2}{4M^2 + 2Q^2 + \frac{Q^4}{4M^2}} \\ &= \frac{\frac{Q^4}{16M^4} + \frac{Q^2}{4M^2}}{1 + \frac{2Q^2}{4M^2} + \frac{Q^4}{16M^4}} \\ &= \frac{\tau(1 + \tau)}{(1 + \tau)^2} \\ &= \frac{\tau}{1 + \tau} \end{aligned} \quad (\text{A.53})$$

where $\tau = \frac{Q^2}{4M^2}$. This gives

$$1 - \beta^2 = 1 - \frac{\tau}{1 + \tau} = \frac{1}{1 + \tau} \quad (\text{A.54})$$

so that

$$\cot^2 \frac{\theta_B}{2} = \frac{\cot^2 \frac{\theta}{2}}{1 + \tau}. \quad (\text{A.55})$$

A.3 Proton Transition Current in the Breit Frame

Putting Γ_μ (A.11) into the modified proton transition current (A.39) gives

$$\mathcal{J}_\mu = \bar{u}_f(F_1\gamma_\mu + \frac{i\kappa}{2M}F_2\sigma_{\mu\nu}q^\nu)u_i \quad . \quad (A.56)$$

Using Gordon decomposition (A.8) this can be written as ^[57]

$$\mathcal{J}_\mu = \bar{u}_f[\gamma_\mu(F_1 + \kappa F_2) - \frac{(p_\mu + p'_\mu)}{2M}\kappa F_2]u_i \quad . \quad (A.57)$$

To determine the different \mathcal{J}_μ there are three quantities that need to be evaluated: $\bar{u}_f u_i$; $\bar{u}_f \gamma_0 u_i$; and $\bar{u}_f \gamma_k u_i$, where $k = 1, 2, 3$. Note that in the Breit frame, where $\vec{p} = -\vec{p}'$, the second term in (A.57) is zero for \mathcal{J}_k .

For positive energy, the four-component spinor $u(\mathbf{p})$ is:

$$u^{(s)} = \sqrt{E+m} \begin{pmatrix} \chi^{(s)} \\ \frac{\vec{\sigma} \cdot \vec{p}}{E+m} \chi^{(s)} \end{pmatrix} \quad (A.58)$$

while the corresponding $\bar{u}(\mathbf{p}')$ is:

$$\bar{u}^{(s')} = \sqrt{E+m} \left(\chi^{(s')\dagger} - \frac{\vec{\sigma} \cdot \vec{p}'}{E+m} \chi^{(s')\dagger} \right) \quad . \quad (A.59)$$

$s = 1, 2$ and χ is a two-component spinor with

$$\chi_i^\dagger \chi_j = \delta_{ij} \quad . \quad (A.60)$$

Using these values in the Breit frame gives: ^[57]

$$\begin{aligned} \bar{u}_f u_i &= (E+M) \left(1 + \frac{(\vec{\sigma} \cdot \vec{p})^2}{(E+M)^2} \right) \\ &= \frac{E^2 + M^2 + 2EM + |\vec{p}|^2}{E+M} \\ &= 2E \end{aligned} \quad (A.61)$$

where the relationship $(\vec{\sigma} \cdot \vec{p})^2 = |\vec{p}|^2$ has been used. Similarly, $\bar{u}_f \gamma_0 u_i = 2M$.

Using these results makes the modified charge density:

$$\begin{aligned}
 \mathcal{J}_0 &= 2M[F_1 + (1 - \frac{E^2}{M^2})\kappa F_2] \\
 &= 2M[F_1 - \frac{|\vec{p}|^2}{M^2}\kappa F_2] \\
 &= 2M[F_1 + \frac{q^2}{4M^2}\kappa F_2]
 \end{aligned} \tag{A.62}$$

where (A.42) has been used in the last step. By defining

$$G_E = F_1 + \frac{\kappa q^2}{4M^2}F_2 \tag{A.63}$$

one gets

$$\mathcal{J}_0 = 2MG_E \quad . \tag{A.64}$$

The remaining term to evaluate is $\bar{u}_f \gamma_\mu u_i$. Using the four-component spinors (A.58 and A.59) here one gets ^[63] ^[64]

$$\bar{u}_f \gamma_k u_i = \chi^{(s')\dagger} [\vec{\sigma}_k (\vec{\sigma} \cdot \vec{p}) + (\vec{\sigma} \cdot \vec{p}') \vec{\sigma}_k] \chi^{(s)} \quad . \tag{A.65}$$

Using the relationship

$$(\vec{\sigma} \cdot \vec{a})(\vec{\sigma} \cdot \vec{b}) = \vec{a} \cdot \vec{b} + i\vec{\sigma} \cdot (\vec{a} \times \vec{b}) \tag{A.66}$$

gives

$$\begin{aligned}
 \bar{u}_f \gamma_k u_i &= \chi^{(s')\dagger} [p_k - i\vec{\sigma} \cdot (\vec{p} \times \hat{n}_k) + p'_k + i\vec{\sigma} \cdot (\vec{p}' \times \hat{n}_k)] \chi^{(s)} \\
 &= \chi^{(s')\dagger} i\vec{\sigma} [(\vec{p}' - \vec{p}) \times \hat{n}_k] \chi^{(s)} \\
 &= \chi^{(s')\dagger} i(\vec{\sigma} \times \vec{q})_k \chi^{(s)} \quad .
 \end{aligned} \tag{A.67}$$

This makes the modified proton transition current

$$\mathcal{J}_k = \chi^{(s')\dagger} i(\vec{\sigma} \times \vec{q})_k (F_1 + \kappa F_2) \chi^{(s)} \quad . \tag{A.68}$$

[63] J.J. Sakurai, *Advanced Quantum Mechanics*, Addison-Wesley, (1967).

[64] V.B. Berestetskii, E.M. Lifshitz, and L.P. Pitaevskii, *Relativistic Quantum Theory*, Addison-Wesley, (1971).

As in the case of \mathcal{J}_0 , it is convenient to use a linear combination of F_1 and F_2 ; in this case,

$$G_M = F_1 + \kappa F_2 \quad . \quad (A.69)$$

This gives

$$\mathcal{J}_k = \chi^{(s')\dagger} i(\vec{\sigma} \times \vec{q})_k G_M \chi^{(s)} \quad . \quad (A.70)$$

From this current and (A.64) it can be shown that in the Breit frame G_E and G_M (often called the “Sachs form factors”) are the Fourier transforms of the charge and magnetic moment distributions of the proton. ^[24]

By defining the modified proton transition current as ^{[61] [62]}

$$\mathcal{J}_\mu = \chi^{(s')\dagger} \mathcal{F}_\mu \chi^{(s)} \quad , \quad (A.71)$$

one can clearly write the proton tensor (A.40) as

$$W_{\mu\nu} = \frac{1}{2} \text{Tr}(\mathcal{F}_\mu \mathcal{F}_\nu^\dagger) \quad (A.72)$$

using (A.60). The \mathcal{F} s are then simply:

$$\mathcal{F}_0 = 2MG_E \quad (A.73)$$

and

$$\mathcal{F}_k = i(\vec{\sigma} \times \vec{q})_k G_M \quad . \quad (A.74)$$

More specifically, since \vec{q}_B lies entirely along the z-axis in this frame, the components of \mathcal{F}_k are:

$$\begin{aligned} \mathcal{F}_1 &= i|\vec{q}_B| G_M \sigma_2 \\ \mathcal{F}_2 &= -i|\vec{q}_B| G_M \sigma_1 \\ \mathcal{F}_3 &= 0 \quad . \end{aligned} \quad (A.75)$$

The formalism necessary to evaluate the cross sections is now in place.

A.4 Rosenbluth Formula

Putting the above \mathcal{F} s into the proton tensor (A.72), the proton tensor components are: ^[61]

$$\begin{aligned} W_{00} &= 4M^2 G_E^2 \\ W_{11} &= W_{22} = Q^2 G_M^2 \quad , \end{aligned} \quad (\text{A.76})$$

with all of the others equal to zero. Likewise, using the Breit frame four momenta (A.43) in the electron tensor (A.38), gives the nonzero electron tensor components: ^[62]

$$\begin{aligned} L^{00} &= Q^2 \left(\csc^2 \frac{\theta_B}{2} - 1 \right) = Q^2 \cot^2 \frac{\theta_B}{2} \\ L^{01} &= L^{10} = Q^2 \cot \frac{\theta_B}{2} \csc \frac{\theta_B}{2} \\ L^{11} &= Q^2 \left(\cot^2 \frac{\theta_B}{2} + 1 \right) = Q^2 \csc^2 \frac{\theta_B}{2} \\ L^{22} &= Q^2 \quad . \end{aligned} \quad (\text{A.77})$$

(Please note that the electron tensor is symmetric in this case.) Therefore the electron-proton tensor product is

$$L^{\mu\nu} W_{\mu\nu} = 4M^2 G_E^2 Q^2 \frac{\cot^2 \frac{\theta}{2}}{1 + \tau} + Q^4 G_M^2 \left(2 + \frac{\cot^2 \frac{\theta}{2}}{1 + \tau} \right) \quad , \quad (\text{A.78})$$

where (A.55) has been used to convert from the Breit frame to the lab frame. Putting this into the cross section equation (A.32 and A.35) gives the Rosenbluth cross section

$$\frac{d\sigma}{d\Omega} = \frac{e^4}{64\pi^2 M^2 Q^4} \left(\frac{E'}{E} \right)^2 \left(4M^2 G_E^2 Q^2 \frac{\cot^2 \frac{\theta}{2}}{1 + \tau} + Q^4 G_M^2 \left(2 + \frac{\cot^2 \frac{\theta}{2}}{1 + \tau} \right) \right) \quad . \quad (\text{A.79})$$

It can be insightful to write this equation with the nonstructure cross section,

$$\left[\frac{d\sigma}{d\Omega_e} \right]_{ns} = \frac{\alpha^2 \cos^2(\theta_e/2)}{4E^2 \sin^4(\theta_e/2)} \left(\frac{E'}{E} \right) \quad , \quad (\text{A.80})$$

separated out. Using (A.29-31), it is straightforward to do this and get

$$\left[\frac{d\sigma}{d\Omega_e} \right]_{\text{Rosenbluth}} = \frac{\alpha^2 \cos^2(\theta_e/2)}{4E^2 \sin^4(\theta_e/2)} \left(\frac{E'}{E} \right) \times \left[\frac{G_E^2}{1+\tau} + \tau G_M^2 \left(\frac{1}{1+\tau} + 2 \tan^2 \frac{\theta_e}{2} \right) \right] . \quad (\text{A.81})$$

A.5 Polarizations

In this section polarizations induced in protons scattered by polarized electrons will be derived, as is discussed in Akhiezer and Rekalov. ^[62] These polarizations are in terms of the Sachs form factors and allow for the ratio of G_E to G_M to be determined. For derivation of polarizations using a response function formalism please see Donnelly and Raskin. ^[65]

For a polarized electron in the extreme relativistic limit, the term $\frac{1}{2}(1+h\gamma^5)$ must be introduced ^[59] into the electron tensor (A.37) to project the different electron spin states. h represents the electron beam's helicity, which is ± 1 for a purely polarized beam and $|h| < 1$ for a partially polarized beam, as in this experiment. This adds an antisymmetric part to the previously discussed symmetric part of the electron tensor

$$L^{\mu\nu} = L_S^{\mu\nu} + hL_A^{\mu\nu} . \quad (\text{A.82})$$

This antisymmetric part is (ignoring the mass terms): ^[66]

$$\begin{aligned} L_A^{\mu\nu} &= +\frac{1}{2} \text{Tr}(\not{k}' \gamma^\mu \gamma^5 \not{k} \gamma^\nu) \\ &= +2i\epsilon^{\rho\mu\sigma\nu} k'_\rho k_\sigma . \end{aligned} \quad (\text{A.83})$$

^[65] T.W. Donnelly and A.S. Raskin, Ann. Phys. **169**, 247 (1986).

^[66] R.G. Arnold, C.E. Carlson, and F. Gross, Phys. Rev. C **23**, 363 (1981).

As was done with the symmetric part, the Breit frame four-momenta (A.43) are used to evaluate this tensor's components, the results being:

$$\begin{aligned} L_A^{02} &= -L_A^{20} = -iQ^2 \cot \frac{\theta_B}{2} \\ L_A^{12} &= -L_A^{21} = -iQ^2 \csc \frac{\theta_B}{2} , \end{aligned} \quad (\text{A.84})$$

with the other components being zero.

Of course polarization also affects the proton's tensor (A.72). Specifically, the proton tensor denoting the final polarization in the direction \mathbf{n} of a proton which was initially unpolarized is written as:

$$\mathcal{P}_{\mu\nu}^{(n)} = \frac{1}{2} \text{Tr}[\mathcal{F}_\mu \mathcal{F}_\nu^\dagger (\vec{\sigma} \cdot \hat{n})] . \quad (\text{A.85})$$

Evaluating the tensor components is simply a matter of putting in the \mathcal{F} values (A.73 and A.75). For example,

$$\begin{aligned} \mathcal{P}_{21}^{(n)} &= -Q^2 G_M^2 \frac{1}{2} \text{Tr}[\sigma_1 \sigma_2 (\vec{\sigma} \cdot \hat{n})] \\ &= -Q^2 G_M^2 \frac{1}{2} \text{Tr} \left[\begin{pmatrix} 0 & 1 \\ 1 & 0 \end{pmatrix} \begin{pmatrix} 0 & -i \\ i & 0 \end{pmatrix} \begin{pmatrix} n_z & n_x - in_y \\ n_x + in_y & -n_z \end{pmatrix} \right] \\ &= -Q^2 G_M^2 \frac{1}{2} \text{Tr} \begin{pmatrix} in_z & in_x + in_y \\ -in_x + n_y & in_z \end{pmatrix} . \end{aligned}$$

This gives $\mathcal{P}_{21}^{(z)} = -iQ^2 G_M^2$, while $\mathcal{P}_{21}^{(x),(y)} = 0$ since their traces are zero. A complete listing of the nonzero proton tensor components is:

$$\begin{aligned} \mathcal{P}_{02}^{(x)} &= -\mathcal{P}_{20}^{(x)} = -\mathcal{P}_{01}^{(y)} = \mathcal{P}_{10}^{(y)} = 2iM|\vec{q}_B|G_E G_M \\ \mathcal{P}_{12}^{(z)} &= -\mathcal{P}_{21}^{(z)} = iQ^2 G_M^2 . \end{aligned} \quad (\text{A.86})$$

Note that if one were interested in an experiment using a polarized target instead of measuring the final polarization of the protons, the $(\vec{\sigma} \cdot \hat{n})$ term in (A.85) would have been sandwiched between the \mathcal{F} 's rather than at the end. The tensor components in this case would have been identical except for a sign difference in the z-direction. Hence both options give the same information.

Since the $\mathcal{P}_{\mu\nu}^{(n)}$ s are antisymmetric, and the contraction of symmetric and antisymmetric tensors is zero, only the antisymmetric part of the electron tensor is important for determining the polarized cross section $\frac{d\sigma^{(n)}}{d\Omega_e}$. Again using (A.32 and A.35) one gets:

$$\begin{aligned}\frac{d\sigma^{(x)}}{d\Omega_e} &= -\frac{h|\vec{q}_B|\alpha^2}{MQ^2}\left(\frac{E'}{E}\right)^2 G_E G_M \cot \frac{\theta_B}{2} \\ \frac{d\sigma^{(y)}}{d\Omega_e} &= 0 \\ \frac{d\sigma^{(z)}}{d\Omega_e} &= \frac{h\alpha^2}{2M^2}\left(\frac{E'}{E}\right)^2 G_M^2 \csc \frac{\theta_B}{2} .\end{aligned}\tag{A.87}$$

The polarized cross section divided by the unpolarized cross section gives the polarization:

$$p_n = \frac{\frac{d\sigma^{(n)}}{d\Omega_e}}{\frac{d\sigma}{d\Omega_e}} .\tag{A.88}$$

I will give the values of the polarizations, as stated by Arnold *et al.* ^[66], after going through some of the algebra.

The unpolarized cross section can be written as:

$$\frac{d\sigma}{d\Omega_e} = \left[\frac{d\sigma}{d\Omega} \right]_{ns} \frac{I_0}{1 + \tau}\tag{A.89}$$

where

$$I_0 = G_E^2 + \tau G_M^2 + 2\tau(1 + \tau)G_M^2 \tan^2 \frac{\theta}{2}\tag{A.90}$$

and $\tau = \frac{Q^2}{4M^2}$. By rewriting the nonstructure cross section (A.80) as

$$\left[\frac{d\sigma}{d\Omega_e} \right]_{ns} = \frac{\alpha^2}{Q^2} \left(\frac{E'}{E} \right)^2 \cot^2 \frac{\theta_e}{2}\tag{A.91}$$

and using (A.55), the Breit-lab relationship, it is simple to get the relationship:

$$p_z I_0 = -2hG_E G_M \sqrt{\tau(1 + \tau)} \tan \frac{\theta}{2} .\tag{A.92}$$

Somewhat more algebra is needed to get Arnold *et al.*'s other polarization equation:

$$\begin{aligned} p_z I_0 &= 2h\tau G_M^2 \sec \frac{\theta}{2} \tan \frac{\theta}{2} [(1 + \tau)(1 + \tau \sin^2 \frac{\theta}{2})]^{\frac{1}{2}} \\ &= h \frac{E + E'}{M} \sqrt{\tau(1 + \tau)} G_M^2 \tan^2 \frac{\theta}{2} \end{aligned} \quad (A.93)$$

By taking the ratio of these two measured quantities, one obtains the ratio of G_E/G_M independent of the beam's helicity:

$$\frac{p_x}{p_z} = -\frac{2M}{(E + E') \tan \frac{\theta}{2}} \frac{G_E}{G_M}.$$

Note that the coordinate frame in which this was evaluated has \hat{z} along \vec{q} and \hat{x} transverse to it in the scattering plane (as opposed to our spectrometer's coordinate frame, depicted in figure 4.4, in which \hat{x} is normal to the scattering plane). Thus to avoid any misunderstandings, I rewrite the previous equation as:

$$\frac{p_t}{p_l} = -\frac{2M}{(E + E') \tan \frac{\theta}{2}} \frac{G_E}{G_M}. \quad (A.94)$$

Appendix B

FPP Calibration at IUCF

The FPP was calibrated at IUCF during February 1993. This appendix gives a brief description of the calibration run and results, based on the more detailed description by our group in Lourie *et al.* ^[41]

At IUCF the FPP was directly exposed to a low-intensity ($\approx 10^5/s$) proton beam in the QQSP area. This low-intensity was achieved using many slits, collimators, and a lead degrader. The FPP was mounted on its side so that its bottom chamber faced the beam-pipe. The table on which the FPP was mounted was wheeled and had a hydraulic lift so that the FPP could be moved in all three dimensions with respect to the beam-pipe. This allowed us to illuminate many different regions of the FPP and at different angles. The FPP-table assembly had to be craned into the QQSP area through its removable roof.

Beam energies of 120, 150, 180, and 200 MeV were used and the beam polarization measured by the FPP was compared to the IUCF beamline polarimeters. By reversing the polarization, instrumental asymmetries were canceled out. The ratio of the FPP's measured polarization magnitude at 200 MeV to IUCF's was: 0.976 ± 0.006 . More important than the magnitude measurement is the ratio of spin-up to spin-down polarizations, where asymmetries are not canceled. This ratio was also measured by an IUCF low-energy polarimeter using (p,α) scattering. The FPP ratio to IUCF's was: 1.018 ± 0.011 . Figure B.1 shows our measured asymmetry compared to previous

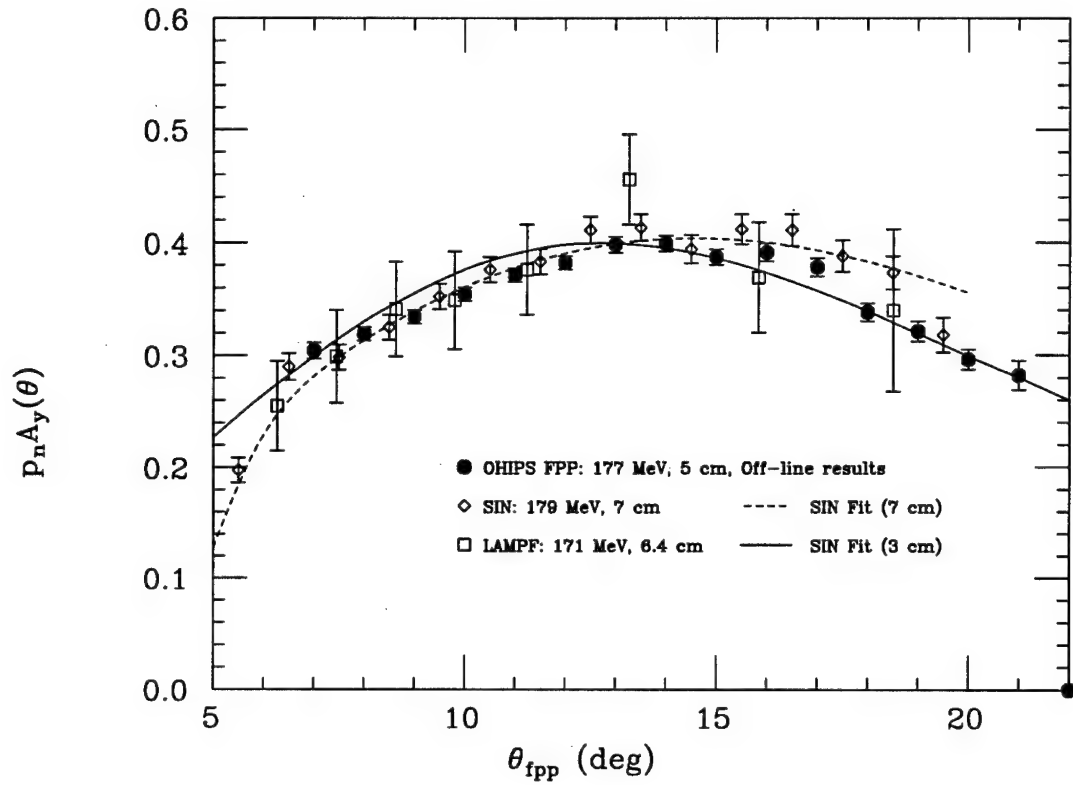


Figure B.1 FPP asymmetry vs. scattering angle at IUCF (solid circles). Other data are from SIN (open diamonds) and LAMPF (open squares). The two fits are from the SIN data set.

data from SIN ^[30] and LAMPF. ^[31]

Appendix C

FPP Alignment

The track reconstruction and carbon scattering angles determination described in section 4.5.1 require that the four FPP wire chambers be aligned well, both with respect to each other and to the VDCX. When the chambers were made, marks were placed on the outside that corresponded to particular wires on the inside. Before beginning our experiment, much time was spent surveying the FPP/VDCX setup. This was all for naught, however, as various problems caused the different chambers and the FPP itself to be taken out of OHIPS prior to the production data acquisition. Also, about a tenth of the way into this experiment a wire broke in chamber 3, requiring the complete removal of the FPP and the quick replacement of a chamber. (Good thing we built spares!) Hence, we only had a crude understanding of the alignment during the experiment. It was not until our experimental program ended months after this experiment (see Epilogue) that the FPP (still in the same configuration since the chamber-3 replacement) was surveyed. The walls of the OHIPS hut were removed and concrete blocks were stacked so that a theodolite could survey the FPP while it was still on OHIPS.

The survey was concerned primarily with the two large back chambers, so that the absolute angular alignment of the FPP could be established. The two chambers were found to be well-aligned except for a -1.1 mm offset needed in chamber 3's y-axis. The survey's uncertainty was dominated by the uncertainty in the fiducial mark location (0.1 mm). This leads to a systematic uncertainty of 0.3 mrad in the FPP's ability to measure an absolute angle.

Chamber	internal offset (cm)	external offset (cm)
X1	0.151	-0.009
X2	0.103	-0.057
X3	0	-0.160
X4	0	-0.160
Y1	-0.573	-0.419
Y2	-0.356	-0.202
Y3	-0.111	0.043
Y4	0	0.154

Table C.1. *FPP Chamber Offsets. The internal offsets refer to the amount the individual chamber axes had to be shifted relative to chamber 4. The external offsets refer to the amount the individual chamber axes had to be shifted relative to the VDCX.*

Next it was necessary to align the front two chambers relative to the back ones. During sieve-slit runs a month after the completion of our experiment, the carbon was taken out of the FPP so that "straight-through" tracks could be recorded. Using these data, we compared actual positions in the front two chambers to those predicted using the back two chambers. The differences between them were called $X1(2)DIF$ and $Y1(2)DIF$ and were correlated with θ_{fp} and ϕ_{fp} , respectively. (The focal plane angles were determined by the VDCX in this case.) These correlations were exploited to determine the offsets

Y IND 246 NO TITLE IN FILE
YLO= 2183 YHI= 2199

TH= 45 PHI= 30

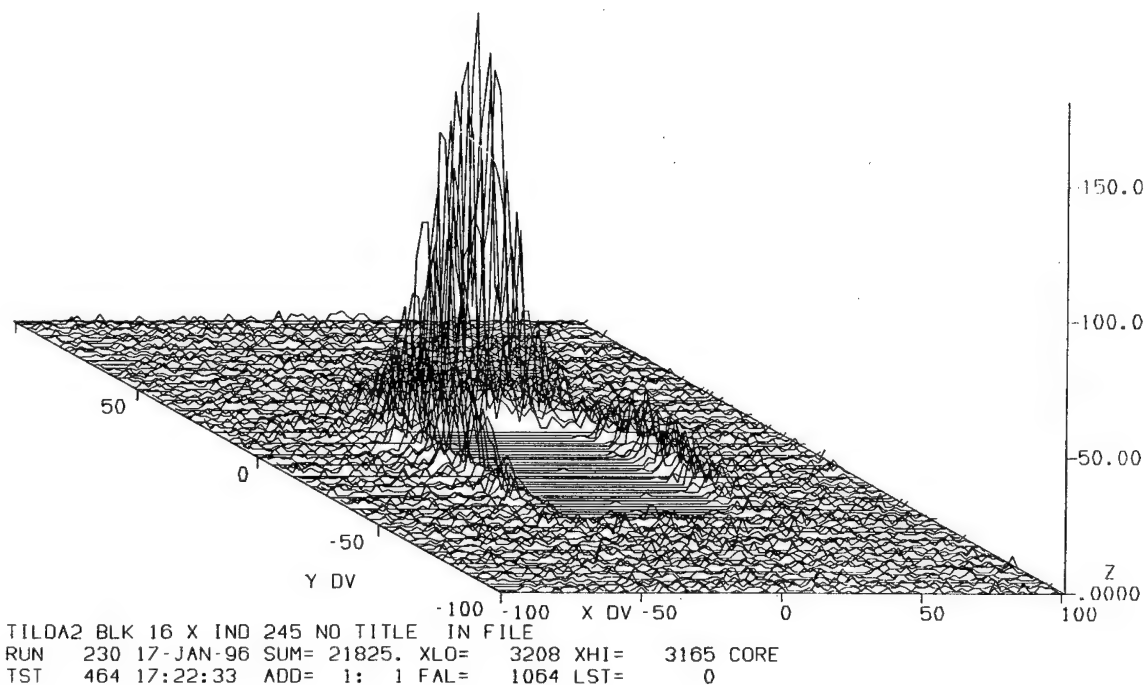


Figure C.1 $z = \theta \cos(\phi)$ versus $y = \theta \sin(\phi)$ showing how the FPP's misalignment effects the small-angle rejection system.

necessary for the DIF spectra to center at zero. ^[67] This task was not as easy as one would think due to the fact that the DIF spectra were not broad peaks, but composed of several discrete peaks due to the “integerization” of the wire chamber positions by the wires themselves. Table C.1 lists these “internal” offsets. Rotation angles in the x-y plane (yaw) were also determined but did not have much effect and were ignored. Pitch and roll are second order effects and were ignored.

[67] G. Warren, Bates Technical Note #96-01.

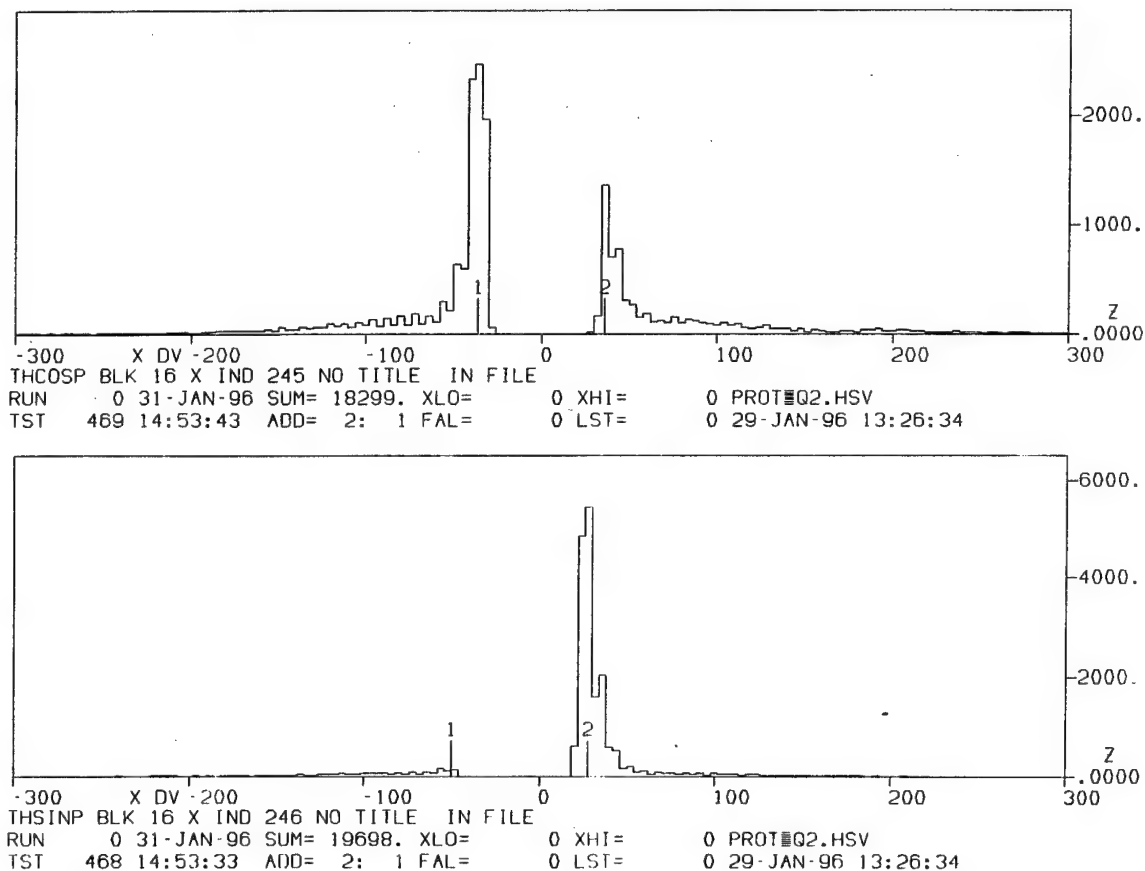


Figure C.2 $x = \theta \cos(\phi)$ cut on $-2 < y = \theta \sin(\phi) < 2$ and vice versa. The area where the distributions decrease toward 0 are regions where the data is biased.

All that was left was to align the FPP relative to the focal plane of the VDCX. Again, this was done by taking DIF spectra between FPP positions projected to the focal plane and what the VDCX, which is accurate in position to 0.1 mm, measured. In this case, “integerization” is not a problem since a drift-chamber is involved. We determined that the FPP’s x-axis had to be shifted by -0.160 cm and the y-axis by 0.154 cm. These offsets are reflected in the “external” offsets of table C.1.

The most problematic aspect of misaligned chambers is not the subsequent

Y IND 246 NO TITLE IN FILE
 YLO= 0 YHI= 0

TH= 45 PHI= 30

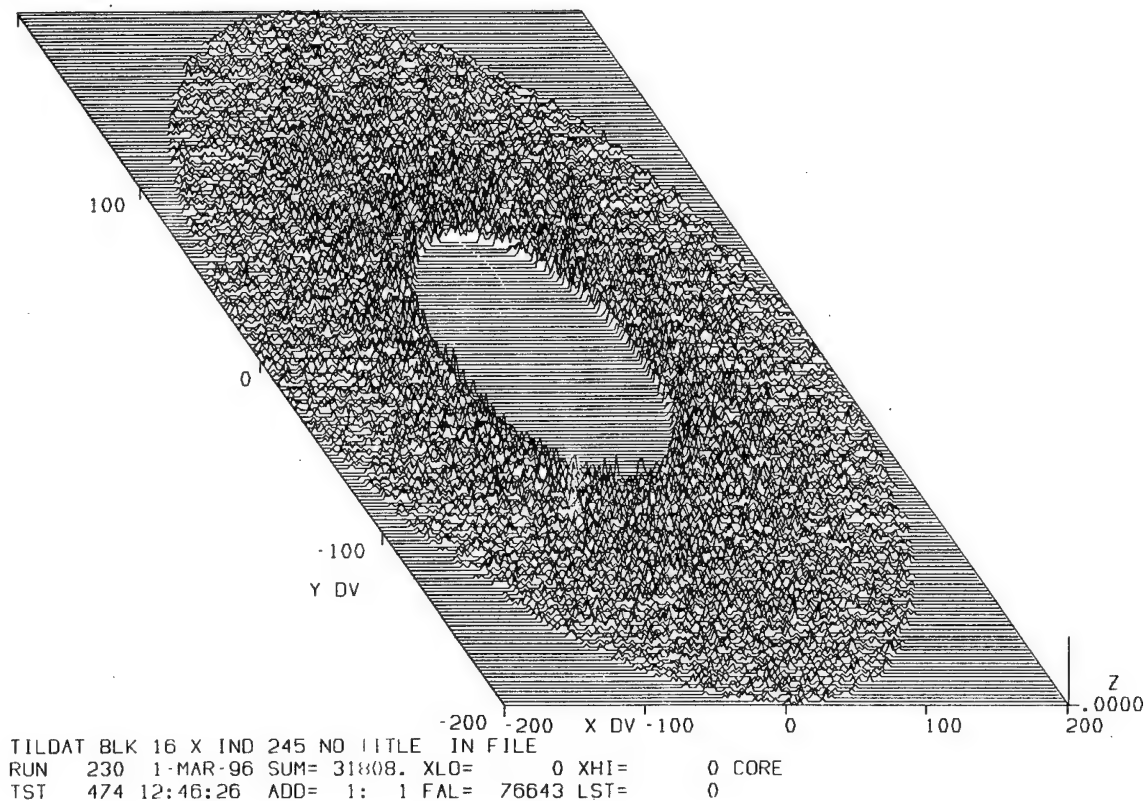


Figure C.3 Event distribution after software θ -cut for the same data as fig. C.1 (but at a different scale). Events whose polar scattering was less than 7° have been excluded, as have those above 20° , where the analyzing power is not well known.

need to determine software offsets. Rather, it is its effects on the FPP's small-angle rejection system (described in section 3.6.2.2). Some events that should have been rejected are accepted and others that should have been accepted are not. The result of this is shown in figure C.1, where $x = \theta \cos(\phi)$ is plotted versus $y = \theta \sin(\phi)$ (these are second scattering angles). This effectively shows the events that passed the MLU. The "dead" region in the center corresponds to rejected events. Instead of being centered on the small- θ peak, it is obviously off to one side.

The above observation necessitated finding the smallest value of θ that produced an unbiased sample. Notice that even if the FPP had been perfectly aligned, we still would have had to reject events that fell within a circle whose radius was the distance from the center of fig. C.1's dead square to its corners. This is because the hardware electronics implemented a box cut whereas we require a circular one to avoid azimuthal biasing. For the early part of our data taking, the MLU was set to reject events with θ below 5° . Part way through the experiment (and prior to the figure shown), it was decided that 3.5° was a more optimal setting. These values correspond to radii of rejection of 7.1° and 5° , respectively. To determine what we actually needed to reject, we plotted $x(=\theta \cos(\phi))$ cut on $-2 < y(=\theta \sin(\phi)) < 2$ and vice versa. These are shown in figure C.2. Those areas where the distributions of events are decreasing toward zero are where bias exists in the data due to both the chamber misalignment and the MLU's square "angular" rejection. This figure is from runs where the MLU was set at 3.5° . It implies that data below $\sqrt{5^{\circ 2} + 4^{\circ 2}} = 6.4^\circ$ is biased. We only analyzed data above 7° (9° for the early data). Recall from fig. 2.3 that this is still not in the region where A_c peaks. Figure C.3 shows the data of fig. C.1 with this software θ -cut.

References

- [1] T. de Forest Jr. and J.D. Walecka, *Adv. Phys.* **15**, 1 (1966).
- [2] M. Gourdin, *Nuovo Cim.* **21**, 1094 (1961).
- [3] M.N. Rosenbluth, *Phys. Rev.* **79**, 615 (1950).
- [4] L.N. Hand, D.G. Miller, and R. Wilson, *Rev. Mod. Phys.* **35**, 335 (1963).
- [5] B. Frois and S. Platchkov, *Modern Topics in Electron Scattering*, eds. B. Frois and I. Sick, World Scientific, (1991).
- [6] L. Andivahis *et al.*, *Phys. Rev. D* **50**, 5491 (1994).
- [7] T.A. Griffy and L.I. Schiff, *High Energy Physics*, Vol. 1, ed. E.H. Burhop, Academic Press, (1967).
- [8] G.G. Simon *et al.*, *Nucl. Phys.* **A333**, 381 (1980).
- [9] G. Höhler *et al.*, *Nucl. Phys.* **B114**, 505 (1976).
- [10] P. Mergell *et al.*, hep-ph/9506375 preprint (20 Jun 95).
- [11] M. Gari and W. Krümpelmann, *Z. Phys.* **A322**, 689 (1985).
- [12] S.J. Brodsky and G.R. Farrar, *Phys. Rev. D* **11**, 1309 (1975); S.J. Brodsky and B.T. Chertok, *Phys. Rev. D* **14**, 3003 (1976).
- [13] G.P. Lepage and S.J. Brodsky, *Phys. Rev. Lett.* **43**, 545, 1625(E) (1979); G.P. Lepage and S.J. Brodsky, *Phys. Rev. D* **22**, 2157 (1980).

-
- [14] M. Aguilar-Benitez *et al.*, Phys. Rev D **50**, 1173 (1994).
- [15] V.L. Chernyak and A.R. Zhitnitsky, Phys. Rep. **112**, 173 (1984).
- [16] X. Song and J.S. McCarthy, Phys. Rev. C **46**, 1077 (1992).
- [17] R.C. Walker *et al.*, Phys. Rev. D **49**, 5671 (1994).
- [18] W. Bartel *et al.*, Nucl. Phys. **B58**, 429 (1973).
- [19] P.E. Bosted *et al.*, Phys. Rev. C **42**, 38 (1990).
- [20] P.E. Bosted *et al.*, Phys. Rev. Lett. **68**, 3841 (1992).
- [21] T. Janssens *et al.*, Phys. Rev. **142**, 922 (1966).
- [22] S. Blatnik and N. Zovko, Acta Phys. Austr. **39**, 1 (1974).
- [23] P. Markowitz, Ph.D. dissertation, William & Mary (1992), unpublished.
- [24] R.G. Sachs, Phys. Rev. **126**, 2256 (1962).
- [25] F. Borkowski *et al.*, Z. Phys. **A275**, 29 (1975).
- [26] M. McCord *et al.*, Nucl. Inst. Meth. **B56**, 496 (1991).
- [27] D.J. Berkeland *et al.*, Phys. Rev. Lett. **75**, 2470 (1995).
- [28] R.G. Arnold *et al.*, Phys. Rev. Lett. **57**, 174 (1986); A.F. Sill *et al.*, Phys. Rev. D **48**, 29 (1993).
- [29] CEBAF PR 93-027, "Electric Form Factor of the Proton by Recoil Polarization", C.F. Perdrisat and V. Punjabi, co-spokespersons.
- [30] E. Aprile-Giboni *et al.*, Nucl. Inst. Meth. **215**, 147 (1983).

- [31] M.W. McNaughton *et al.*, Nucl. Inst. Meth, **A241**, 435 (1985).
- [32] M. Farkhondeh, private explanatory tour of source.
- [33] E. Hecht, *Optics*, Addison-Wesley, (1987).
- [34] D.T. Pierce *et al.*, Rev. Sci. Inst. **51**, 478 (1980).
- [35] J.D. Jackson, *Classical Electrodynamics*, John Wiley & Sons, (1975).
- [36] J. Arrington *et al.*, Nuc. Inst. Meth. **A311**, 39 (1992).
- [37] B. Wagner *et al.*, Nuc. Inst. Meth. **A294**, 541 (1990).
- [38] D. Caditz, B.S. Thesis, M.I.T. (1983), unpublished (Bates Internal Report #85-04).
- [39] W.R. Leo, *Techniques for Nuclear and Particle Physics Experiments*, Springer-Verlag, (1987).
- [40] J. McIntyre and G. Warren, Bates Technical Note #94-01.
- [41] R.W. Lourie *et al.*, IUCF Scientific and Technical Report, 135 (May 1992 - April 1993).
- [42] R.W. Lourie *et al.*, Nuc. Inst. Meth. **A306**, 83 (1991).
- [43] W. Bertozzi *et al.*, Nuc. Inst. Meth. **141**, 457 (1977).
- [44] D. Jordan *et al.*, Bates Internal Report #92-03.
- [45] S.D. Penn, Ph.D. dissertation, MIT(1993), unpublished.
- [46] H. Überall, *Electron Scattering from Complex Nuclei*, Vol. B, Academic Press (1971).

-
- [47] C.S. Whisnant, private communication.
- [48] W. Barkas and M. Berger, *Tables of Energy Losses and Ranges of Heavy Charged Particles*, NASA-SP-3013 (1964).
- [49] J. Janni, *At. Data and Nucl. Data Tables* **27**, nos. 4-5 (1982).
- [50] J.A. Edgington, *Nuc. Inst. Meth.* **164**, 175 (1979).
- [51] D.H. Barkhuff, private communication.
- [52] D. Besset *et al.*, *Nuc. Inst. Meth.* **166**, 515 (1979).
- [53] S. Nurushev, *Nuc. Inst. Meth.* **141**, 417 (1977).
- [54] K. Joo, private communication.
- [55] J. McIntyre, private communication.
- [56] D. Eyl *et al.*, *Z. Phys.* **A352**, 211 (1995).
- [57] F. Halzen and A.D. Martin, *Quarks and Leptons*, John Wiley & Sons, (1984).
- [58] L.M. Chinitz, Ph.D. dissertation, U.Va. (1990), unpublished.
- [59] J.D. Bjorken and S.D. Drell, *Relativistic Quantum Mechanics*, McGraw-Hill, (1964).
- [60] R. Hagedorn, *Relativistic Kinematics*, W.A. Benjamin, (1973).
- [61] N. Dombey, *Rev. Mod. Phys.* **41**, 236 (1969).
- [62] A.I. Akhiezer and M.P. Rekalo, *Fiz. Elem. Chast. Atom. Yad.* **4**, 662 (1973)[*Sov. J. Part. Nucl.* **4**, 277 (1974)].

- [63] J.J. Sakurai, *Advanced Quantum Mechanics*, Addison-Wesley, (1967).
- [64] V.B. Berestetskii, E.M. Lifshitz, and L.P. Pitaevskii, *Relativistic Quantum Theory*, Addison-Wesley, (1971).
- [65] T.W. Donnelly and A.S. Raskin, *Ann. Phys.* **169**, 247 (1986).
- [66] R.G. Arnold, C.E. Carlson, and F. Gross, *Phys. Rev. C* **23**, 363 (1981).
- [67] G. Warren, Bates Technical Note #96-01.

Epilogue and Acknowledgements

As alluded to in the first paragraph of chapter one, the measurement described in this dissertation was done in conjunction with several others, all using the FPP. The FPP was moved to Bates in the spring of 1993 following its calibration run at IUCF and installed in the South Hall that fall. After this, one bad thing after another happened: months had to be spent resurveying and relearning the recirculator tune, the polarized source befell one disaster after another, the target ruptured, etc. (A favorite quote of the graduate students was "One woe be passed. Lo, here cometh two more."). As the need to produce results and theses became more and more desperate, the experiment grew to include measurements that would have otherwise been done as part of separate experiments, adding students and collaborators as it grew. That which had been a big experiment already became a humongous experiment which started in January of 1995 and did not end until early July of that year. The many measurements resulted in eight Ph.D. dissertation topics, including mine.

Taken concurrently with my hydrogen data in January and February of 1995 was quasielastic deuterium data at the same two Q^2 values. This was the dissertation data for Justin I. McIntyre of William & Mary. In April we again took quasielastic $Q^2 = 0.38 \text{ GeV}^2$ deuterium data, but this time in nonparallel kinematics ($\theta_{pq}^{cm} = 19^\circ$ and $p_{recoil} = 100 \text{ Mev/c}$). This dissertation data was for fellow University of Virginia graduate student David H. Barkhuff. A May deuterium measurement (also at $p_{recoil} = 100 \text{ Mev/c}$) in the "dip" region beyond the quasielastic peak provided data for Kyungseon Joo of Massachusetts Institute of Technology. In February and March, while the polarized source was down, $^{12}\text{C}(e, e'\bar{p})$ data was taken for Rhett J. Woo of W&M to study the induced normal polarization as a function of recoil momentum in order to test for non-PWIA nucleon-nucleus dynamics. Induced normal polarizations were

also looked for in the June $^1\text{H}(e,e'\vec{p})\pi^0$ experiment, whose data comprises the dissertation of M.I.T.'s Glen A. Warren. This measurement at $\omega = 1232$ MeV was designed to help constrain background models in the $N \rightarrow \Delta$ transition. $^1\text{H}(e,e'p)\pi^0$ measurements from May to early July of the response functions R_T and R_{LT} over a range of invariant masses were taken to study the C2/M1 ratio in the $N \rightarrow \Delta$ transition. Christophe Mertz of Arizona State University and Costas Vellidis of the University of Athens analyzed this data.

It should be pointed out that many of these other measurements used the hydrogen results. Since there are no final state interactions for an outgoing proton in hydrogen, p_n is very nearly equal to 0, and there are no physical asymmetries in the unpolarized proton data. This allowed the FPP's systematic asymmetries to be determined (as described in section 4.6) and used in the hydrogen and non-hydrogen data alike. Since the PWIA can be considered valid for hydrogen, the measured polarizations of the other experiments could be normalized with respect to hydrogen's.

Given the size of this project, there are a lot of people who deserve my thanks and acknowledgement. Foremost among them would be our group leader and my advisor, Robert Lourie. He's a brilliant physicist and it has been a pleasure to learn under him. He took a very active role in the early planning and development of the experiment's code and electronics and was more involved in the day-to-day management of keeping the experiment running successfully than I've ever seen from a professor. He was also far-and-above the best classroom teacher I had at UVa.

The other spokesmen for my experiment were Mike Finn and Charles Perdrisat of William & Mary and Paul Ulmer, formerly at CEBAF and now at Old Dominion University. One couldn't ask for a nicer group of experiment leaders. Dr. Finn was quite involved with the experimental trigger electronics

and served as a good counter-balance to Robert. Dr. Perdrisat provided the FPP's scintillators and Dr. Ulmer was quite involved with determining the kinematics, beam times, etc., needed for making our experiment a success.

Scott Van Verst, now at the Washington Dept. of Health's Division of Radiation Protection, was our group's UVa postdoc for most of my time with the group, though he became an M.I.T. research scientist right before the data started coming in. He oversaw the building of the FPP and was chiefly responsible for the experiment's complicated electronics. Scott was very good at explaining things in simple terms and I enjoyed our many lunches together at the Pav.

David Barkhuff was my friend and classmate even before I joined this experimental group in the spring of 1991 and it's too bad that we were not able to work together more, since he was at Bates and I was primarily in Charlottesville. David built our wire-chambers pretty much all by himself, was responsible for our experimental control electronics, and developed many of the key parts of our analyzer code, such as the FPP and polarization-determination codes – much more than any one student should have to do to get a Ph.D.

Justin McIntyre grew from a fresh, rash-decision-making new student to a dependable, take-charge compatriot and also my best friend in the experiment. I enjoyed our many shifts together and our many outings together, especially those many walks at Crane's Beach and conversations in the Danvers YMCA sauna. I think those more than anything got us through those agonizing setbacks of 1994. Justin was deeply involved in the experiment's electronics, particularly the extensive trigger electronics.

M.I.T. was well represented by Glen Warren, Kyungseon Joo, and Dan Dale - a postdoc who later became a professor at the University of Kentucky. Glen was our man in charge of the target and also developed many valuable

tools for some of the not-so-fun parts of our analysis, such as chamber alignment and vdcx drift-time to drift-distance conversion. Kyungseon analyzed all of the Møller data for us. Dan Dale worked extensively on getting the wire chambers to work and getting our IUCF calibration run to be successful.

Though our run at Bates was not a smooth one, it was certainly no fault of the people there, who are top-notch and deserve thanks for trying so hard to make our experiment a success. I especially enjoyed working with Karen Dow on data acquisition matters. Manousch Farakhondeh and George Dodson worked very hard to get us polarized beam, as did the accelerator guys in general, particularly Steve Bradley, the tune-master. Dan Tieger was the spectrometer-dude. The target group and crane-operators (especially Stevie) worked very hard for us, as did everyone in general. I appreciate all the watching-out for us students that Anne, Sheila, Ginny, and Audrey provided.

Thanks also to the IUCF staff that made our calibration run there so successful: Chuck Foster, Ed Stephenson, chamber-specialist Keith Solberg, computer expert N. Yoder, Jim Crail and his terrific crew, and Theresa May.

Thanks to Christophe and Rhett for their extensive data-taking shift work. Thanks also to former UVa postdoc Joe Mitchell (now at CEBAF) for his work in the early stages and to Shalev Gilad, Bill Bertozzi, and George Sechen of M.I.T. for their work in getting our wire chambers built.

Thanks to the Cal State-L.A. group: Marty Epstein, S. Mukhopadhyay, and D. Liu for their help in data taking, particularly at IUCF. Old Dominion Univ.'s Larry Weinstein also took a lot of shifts, particularly during some key check-out runs. Thanks to W&M postdocs R. Pourang for his scintillator work and Mark Jones for his data-taking work. W&M's Chris Armstrong also helped, as did Pete Markowitz of the University of Maryland (now at Florida International), Vina Punjabi of Norfolk State, Hossain Baghaei of UVa; and

Jen-Ping Chen (now at CEBAF), Adam Sarty (now at Florida State Univ.), and Wolfgang Korsch (now at Cal Tech), all from M.I.T.

I'd also like to thank the UVa group I worked with prior to joining Robert's group for the valuable things I learned from them (not to mention the summer in Los Alamos): Steve Thornton, Richard Sealock, Sam Hoblitt, Cole Smith (who taught me 'Q'), and Ralph Minehart.

Thanks also to the wonderful staff at the UVa physics department. Jody Leake and Pam Joseph made sure I got paid. Suzie Garrett and Sybil Hale watched out for me in general, while Nancy Honeywell had to process my many travel reimbursements. George Plum and his machine-shop crew were great to work with, as was Bobby Floyd in the stockroom. I enjoyed Pat Walsh's services as the VAX-cluster master and probably used computer-guru Bryan Wright more than anyone else in the department during this last year. Jim Shea helped me quite a bit in the library and was a fun guy to chat with in general.

I'd like to thank officemates Tom Gresko and Peter Karen for taking care of things for me while I was away. Thanks to Robert Lourie for his \TeX thesis macros and to Justin, Glen, Rhett, and Arizona State's Steve Dolfini for the many figures that they provided for this dissertation. I appreciate the help of officemate Kevin Cromer and the Instructional Resource Center's Y. Stephanie Milbrath (nee Lin) concerning incorporating figures into \TeX . Thanks to my committee members: Robert Lourie, Ralph Minehart, Robert Mulder, and Blaine Norum for their service.

Thanks to Stephanie and my parents for their support and encouragement during graduate school. Finally, I appreciate the financial support I received during graduate school from the Air Force Office of Sponsored Research, the Dept. of Energy, and the UVa Physics Dept.

To everyone out there who has just read these acknowledgements without bothering to read all or part of the dissertation itself, I say this: Have you thought about getting a life? This is not the most important part of the dissertation, just THE END.